



NTNU – Trondheim
Norwegian University of
Science and Technology

Characterization of Non-Metallic Inclusions in Ferritic Weld Metals for Arctic Applications

Isabella Juul Hjeltereie

Materials Technology

Submission date: June 2015

Supervisor: Odd Magne Akselsen, IPM

Co-supervisor: John Walmsley, SINTEF

Norwegian University of Science and Technology
Department of Engineering Design and Materials

Preface

This master's thesis is submitted as a part of a master program in Material Science and Engineering at The Norwegian University of Science and Technology, (NTNU). It was carried out at the Department of Materials Science and Technology and is written in collaboration with SINTEF Materials and Chemistry. The project description for this report is attached in Appendix A and the risk assessment of the experimental work is attached in Appendix B.

This thesis is part of the SINTEF-project "Arctic Materials", in which they collaborate with NTNU. The main goal of the project is to establish criteria and solutions for safe and cost-effective application of materials for hydrocarbon exploration and production in arctic regions.

Declaration

I herby declare that this work has been carried out independently and according to the examination regulations of The Norwegian University of Science and Technology (NTNU).

Trondheim, June 10th, 2015



Isabella Juul Hjeltterei

Abstract

In Arctic applications, structural steel weldments will be subjected to low temperatures, in the worst cases approaching -60 °C. This may be a major challenge, due to the ductile to brittle transition taking place at certain temperature below 0 °C. Thus, the fracture toughness and the use of commercial wires will be of major concern. One factor influencing the weld metal toughness is the microstructure, which again may be dependent on the non-metallic inclusions entrapped in the weld metal.

The main objective in the present work is to characterize the weld metal microstructure and determine the characteristics of the non-metallic inclusions. Three welds were investigated using optical microscopy, scanning electron microscopy and transmission electron microscope to decide the type, chemical composition and size distribution of the inclusions and eventual orientation relationships with the surrounding matrix.

Results from investigating the specimens in optical microscope revealed that specimen 2.1 has the highest fraction of acicular ferrite, while specimen 3.1 consists mainly of bainite and specimen 5.2.1 is a mixture of several microstructures. Examination in the micro probe showed that the non-metallic inclusions had either high titanium or aluminum content, and it seems to have an effect on the amount of acicular ferrite in the weld metal. In addition the inclusions contained oxygen, nitrogen and manganese, which seem to have had a positive effect on the microstructure, since increased content of these elements showed larger amounts of acicular ferrite. Specimen 2.1 and 5.2.1 had both larger and more inclusions than specimen 3.1 when the size distribution of the inclusions was measured.

In the fracture surface appearance of specimen 2.1 and 5.2.1 had both a large ductile crack growth before the brittle fracture occurred. Specimen 3.1 showed nearly no plastic deformation before fracture, indicating a brittle microstructure.

Results from the chemical analysis in the TEM show that the inclusions in specimen 2.1 consist of a titanium oxide core and the surrounding edge composed of manganese sulphide and a complex oxide. Specimen 3.1 has a high aluminum content consisting together with oxygen or nitrogen. Specimen 5.2.1 consisted of complex inclusions with aluminum, manganese, silicon and oxygen. One inclusion in specimen 2.1 was indexed and it indicated an orientation relationship to the surrounding matrix. The exact chemical composition of the same inclusion was also confirmed.

Sammendrag

I arktiske anvendelser vil sveiste strukturer bli utsatt for lave temperaturer, i de verste tilfeller helt ned til $-60\text{ }^{\circ}\text{C}$. Dette kan by på en stor utfordring på konstruksjonsstålet pga. duktil til sprø overgang som skjer ved en viss temperatur under $0\text{ }^{\circ}\text{C}$. Derfor vil bruddseigheten og bruken av kommersielle sveisetråder være en stor bekymring. Seigheten på sveisemetallet vil bli påvirket av flere faktorer. En faktor som påvirker seigheten i sveisemetallet er mikrostrukturen, som igjen er avhengig av de ikke-metalliske inneslutningene oppfanget i sveisemetallet.

Hovedmålet i dette arbeidet er å karakterisere mikrostrukturen i sveisemetallet og bestemme karakteristikken av de ikke-metalliske inneslutningene. Tre sveiser er blitt undersøkt ved å bruke lysmikroskop, skanning elektronmikroskop og transmisjons elektronmikroskop for bestemme type, kjemisk sammensetning og størrelsesfordeling av inneslutningene, og eventuelt orienteringsforhold til omkringliggende matriks.

Resultatene fra undersøkelse av prøvene i lysmikroskopet viste at prøve 2.1 har den høyeste andelen med aciculær ferritt, mens prøve 3.1 hovedsakelig besto av bainitt og prøve 5.2.1 en blanding av flere mikrostrukturer. Undersøkelse i mikrosonde viste av de ikke-metalliske inneslutningene enten hadde et høyt titan- eller aluminiums innhold, og det ser ut som det har hatt en effekt på mengden aciculær ferritt sveisemetallet. I tillegg inneholdt inneslutningene oksygen, nitrogen og mangan, som så ut til å ha en positiv effekt på mikrostrukturen, siden økt innhold av disse elementene viste større mengde aciculær ferritt. Prøve 2.1 og 5.2.1 hadde begge større og flere inneslutninger enn prøve 3.1 når størrelsesfordelingen av inneslutningene ble målt.

Bruddoverflaten på prøve 2.1 og 5.2.1 hadde begge et stort duktilt bruddområde før sprøbruddet oppsto. Prøve 3.1 viste nesten ingen plastisk deformasjon før bruddet, noe som indikerer en sprø mikrostruktur.

Resultatene fra den kjemiske analysen i TEM viser at inneslutningene i prøve 2.1 består av titanoksid i kjernen og mangansulfid, samt et komplekst oksid i kanten rundt. Prøve 3.1 hadde et høyt aluminiums innhold bestående med oksygen eller nitrogen. Prøve 5.2.1 besto av komplekse inneslutninger med aluminium, mangan, silisium og oksygen. En inneslutning i prøve 2.1 ble indeksert og det antydning til et orienteringsforhold med omkringliggende matriks. Den eksakte kjemiske sammensetningen av denne inneslutningen ble også bekreftet.

Acknowledgment

First of all I wish to thank my supervisor Professor Odd Magne Akselsen at SINTEF for doing his utmost to help me with the various challenges encountered during this thesis. He has been committed and has shared his knowledge to provide the necessary quality to this study.

I am particularly grateful for the support I received from my co-supervisor John Walmsley (SINTEF) in the art of operating a TEM.

I wish to thank Elin Pettersen (SINTEF) and Trygve Lindahl Schanche (NTNU), for their assistance at the Metallurgical Laboratory, and Brigitte Karlsen (SINTEF) for her help in preparing specimens for use in the TEM.

I thank senior engineers Yingda Yu Morten and Peder Raanes at the Electron Microscopy Laboratories, NTNU, for assistance with EBSD and chemical analysis by micro probe. I also wish to thank Ida Westermann and Jarle Hjelen for useful input throughout the process.

Table of Contents

Preface	I
Abstract	III
Sammendrag	V
Acknowledgment	VII
List of abbreviations	XI
Chapter 1 Introduction	1
Chapter 2 Theoretical background	3
2.1 Welding	3
2.2 Non-metallic inclusions	3
2.3 Phase transformation during welding	3
2.4 Formation of acicular ferrite	4
2.5 Nucleation of acicular ferrite	5
2.6 Growth of acicular ferrite	8
2.7 Bainite	9
2.8 Optical microscopy	10
2.9 Fracture	10
2.9.1 Brittle fracture	10
2.9.2 Ductile fracture	11
2.9.3 Charpy V-notch test	12
2.10 Scanning Electron Microscope	13
2.11 Electron Microprobe	14
2.12 Transmission electron microscope (TEM)	14
2.12.1 Diffraction patterns	16
2.12.2 Particles in TEM	18
Chapter 3 Experimental work	19
3.1 Materials	19
3.2 Sample preparation	21
3.3 Optical Microscope and SEM	23
3.4 Electron Microprobe	24
3.5 Size distribution	24
3.6 Transmission electron microscopy	25
3.7 Indexing of the diffraction patterns	25
Chapter 4 Results	29
4.1 Microstructural characterization and quantification	29
4.2 Microprobe analyses	33
4.3 Size distribution of non-metallic inclusions	36
4.4 Fracture surface appearance	38
4.5 TEM	43
4.5.1 Type and composition	43
4.5.2 Indexing of the inclusions	50
4.5.3 Orientation relationship	52

Chapter 5 Discussion	55
5.1 Microstructure	55
5.2 Micro probe and size distribution	56
5.3 Fracture surface	57
5.4 TEM	58
5.4.1 Chemical analysis	58
5.4.2 Indexed diffraction patterns	59
5.4.3 Orientation relationship	59
Chapter 6 Conclusion	61
Suggestions to further work.....	63
References.....	65
Appendix.....	i
A – Project description	i
B – Risk assessment	iii
C – MacTempasX input data	vi
Ti ₃ O ₅	vi
MnS	vii

List of abbreviations

HSLA:	High strength low alloy
γ :	Austenite
α :	Ferrite
AF:	Acicular ferrite
PF:	Polygonal ferrite
GBF:	Grain boundary ferrite
WF:	Widmanstätten ferrite
UB:	Upper bainite
LB:	Lower bainite
WM:	Weld metal
CGWM:	Coarse-grained weld metal
FGWM:	Fine-grained weld metal
SS FCAW:	Self-shielded flux-cored arc welding
GS FCAW:	Gas-shielded flux-cored arc welding
PF:	Flat horizontal position
PC:	Transverse position
SEM:	Secondary electron microscope
TEM:	Transmission electron microscope
STEM:	Scanning transmission electron microscope
ADF:	Annular dark field
MDZ:	Manganese-depleted zone
FCC:	Face centered cubic
BCC:	Body centered cubic

Chapter 1 Introduction

It is believed that around 25 % of the worlds undiscovered oil and gas is located in the Northern Sea. When these areas are to be explored it will require better materials due to the harsh climate conditions.

When structural steels are used in Arctic environments they will be exposed to low temperatures, approaching down to -60 °C. Also the harsh weather conditions and the poor light conditions influence how maintenance, installation and transportation is done. It is therefore important to develop robust applications that are easy to maintain and deploy. One of the largest concerns will be the fracture toughness of the steel. Investigation show that the properties of weldments of available structural steels are insufficient or on the borderline for arctic applications down to -60 °C. Structures are welded together and during welding the microstructure in the steel will change and the new microstructure that forms will be one of the factors controlling the toughness. The microstructure formed during welding is dependent on the type of non-metallic inclusions and their size distribution and chemical composition.

Acicular ferrite microstructure in steel weld metal gives an optimal combination of high strength and high toughness, which make this microstructure very desirable. The good mechanical properties that acicular ferrite have is because of the plates that nucleate intragranularly on non-metallic inclusions inside large austenite grains and grow in many different directions giving it a non-ordered structure [1]. Test results from several analysis show that the fracture-appearance transition-temperature decreases and the yield strength increases with increased proportion of acicular ferrite. This is illustrated in Figure 1 [2].

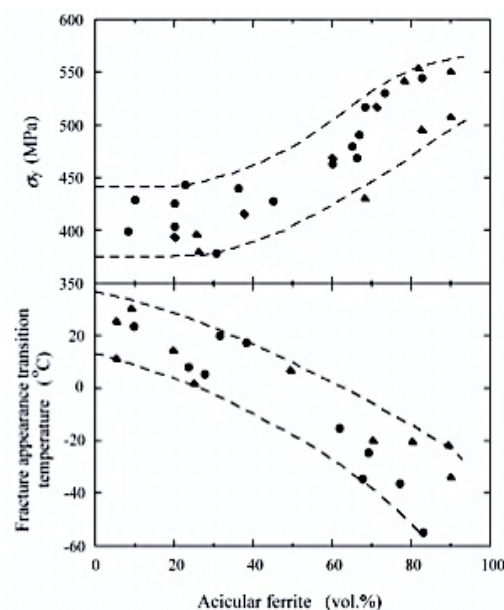


Figure 1. Illustration of the variation in yield strength and fracture appearance transition temperature with the volume fraction of acicular ferrite [2].

The main objective for this project is to characterize the microstructure of the weld metal and determine the characteristics of the non-metallic inclusions in the weld metal in respect of chemical composition, type and size. Also, it is desirable to establish information on the orientation relationship with the microstructure. This is in order to obtain a greater understanding of the development of transformation textures in low alloy steel metals [3]. To do this a transmission electron microscope (TEM) is a suitable technique to index the diffraction pattern extracted from the microscopic investigation.

Chapter 2 Theoretical background

2.1 Welding

An arc-welded joint consists of two major regions, the fusion zone and the heat-affected zone (HAZ). This project focuses on the fusion zone where the deposit metal and steel is melted during the welding process. Grains in the fusion zone grow along the direction of the heat flow, and are therefore anisotropic. During the solidification of the fusion zone oxide, silicate and sulphide particles are entrapped and are referred to as non-metallic inclusions. These inclusions are heterogeneous nucleation sites and are important in the formation of the microstructure. The chemical composition of the weld metal is dependent on the base material, wire and flux compositions. Several types of microstructures may form during cooling, including allotriomorphic, Widmanstätten and acicular ferrite, as well as bainite, in addition to micro phases. In cases where there are multiple layers, some regions of original primary weld metal microstructure are reheated. This region can be divided into coarse-grained, fine-grained and partially reheated weld metal.

2.2 Non-metallic inclusions

Since the solubility of oxygen in steel is negligible ($< 1\text{ ppm}$), the present oxygen is therefor available as non-metallic inclusions. The volume fraction (V_V) of endogenous inclusions (oxides, sulphide, nitrides and carbides) is directly related to the oxygen (O) and sulfide (S) content in the weld. For Al-Ti-Si-Mn deoxidized weld metals the following correlation can be made [4]:

$$V_V = 10^{-2}[5.0 (\text{wt\% O}) + 5.4 (\text{wt\% S} - 0.003)] \quad (1)$$

2.3 Phase transformation during welding

During welding of steel different types of microstructures may form, both in the weld metal and in the heat affected zone (HAZ) during the austenite (γ) to ferrite (α) transformation. This depends on the chosen combination of base material, welding wire and the welding parameters. The microstructure is classified into five structure components [4]:

M: Martensite and lower bainite.

SP: Side-plate ferrite. This also includes Widmanstätten ferrite and upper bainite, and consists of two or more parallel plates that nucleate on grain boundaries or in the matrix. The plates are separated by a micro-phase (perlite, cementite, martensite, austenite).

- AF: Acicular ferrite. This designation covers separate ferrite-needles with relative high length-to-width relationship that nucleate heterogeneous in the matrix.
- F: Ferrite. Includes both allotriomorphic and idiomorphic structure in terms of grain boundary ferrite and equiaxed ferrite.
- P: Pearlite. Have a structure of separate colonies that occur preferably in the base material or in the fine-grained HAZ at relatively slow cooling.

2.4 Formation of acicular ferrite

The expression acicular means shaped and pointed like needles and the acicular ferrite microstructure is often described as chaotic. Figure 2 shows a SEM image of a weld microstructure containing acicular ferrite that has nucleated from a non-metallic inclusion and an illustration of the chaotic microstructure. The microstructure has a three dimensional morphology of thin, lenticular plates. Experiments show that the length, width and thickness are less than 36.0, 6.0 and 3.0 μm , respectively [5].

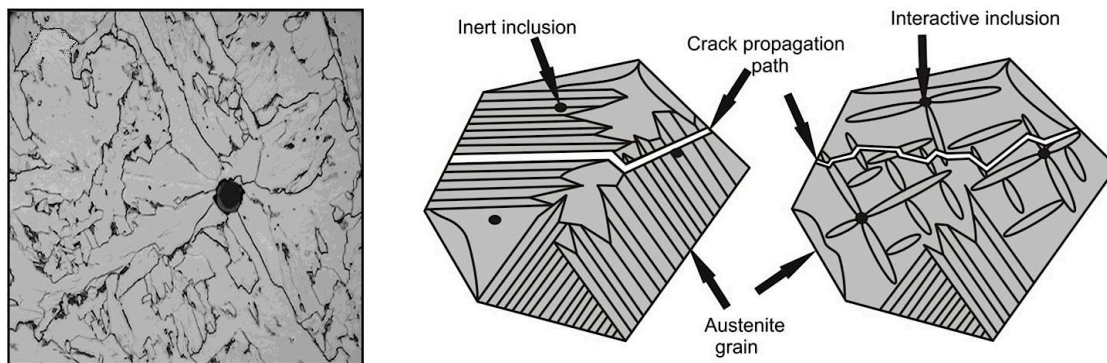


Figure 2. On the left is an SEM-image of acicular ferrite nucleating from on a non-metallic inclusion. On the right is an illustration on how acicular ferrite hinders crack propagation because of the chaotic microstructure [2].

The transformation mechanism of acicular ferrite and bainite is quite similar, even though their microstructure is different. While bainite sheaves grow as groups of parallel plates from the austenite grain surfaces, acicular ferrite plates will nucleate intra-granularly at point sites, making parallel formations impossible. In both cases of growth there will be an invariant-plane strain shape deformation with a large shear component. The lattice of the acicular ferrite is generated by deformation of austenite, and makes it unable for iron and substitutional solutes to diffuse during the transformation from austenite to acicular ferrite. The concentration of the substitutional alloying elements is therefore unchanged within the growth of acicular ferrite. This is called displacive transformation. On the other hand is reconstructive transformation, or diffusion transformation, and involves breaking and reforming of bonds. This may result in a completely new atomic arrangement [5].

The new structure that forms are intimately related to that of the austenite, this is due to the fact that deformation of austenite, which changes to acicular ferrite, occurs on

particular planes and directions. Acicular, Widmanstätten and bainitic ferrite holds the Kurdjumov-Sachs (K-S) orientation relationship with the parent austenite grain in low carbon steels [6]. When the carbon concentration of the remaining austenite reaches a certain level, which makes it impossible to decompose any more without diffusion, the acicular ferrite reaction will stop. Acicular ferrite will therefore grow supersaturated on carbon, but will shortly afterwards reject the excess carbon into the austenite.

The density of the inclusions are lower than the austenite grain boundaries and the available surface area for nucleation at the austenite grain boundaries is greater than that of the intragranular inclusions. This makes the austenite grain boundaries the favorable site for nucleation [7]. It is possible to have a steel containing inclusions to transform from bainite into acicular ferrite, by making the austenite grain surface to an ineffective nucleation site. This is possible by covering the boundaries with inert allotriomorphic ferrite, or by adding small amounts of boron. The boron will make the boundaries a less favorable site for nucleation to start. All methods that will increase intragranular nucleation sites will help the formation of acicular ferrite [5].

This also includes the cooling time, often given as $\Delta t_{8/5}$. This factor is of highly importance during the austenite to ferrite transformation since the formed microstructure depends of it. The chemical composition of the steel decides the optimal cooling rate to obtain acicular ferrite [2]. Earlier research found that by increasing the heat input the peak frequency of inclusion size distribution shifts towards larger inclusion diameter [8]. Growth of inclusions in the weld pool occurs as a result of coarsening of particles (Oswald ripening). Research has shown that the mean particle diameter (d_v) is proportional to the net heat input during welding:

$$d_v(\mu m) = 0.35 \cdot (\eta E)^{\frac{1}{3}} \quad (1)$$

where η is the arc efficiency and E (kJ/mm) is the gross heat input [4].

2.5 Nucleation of acicular ferrite

Earlier experiments show that titanium-rich inclusions are very effective in the acicular ferrite production. Research show that by adding 0.005 wt% of Ti it increases the content of acicular ferrite significantly. Plate steels containing inclusions with titanium and oxygen have proven to be very effective. Ti_2O_3 particles were found active in Mn-bearing steels, but were inert in Mn-free steels [2]. Recent research on similar weld metals also shows that the inclusion size decreases and the inclusion density increases with increased amount of Ti. It also showed that maximum acicular ferrite content and the lowest ductile-to-brittle transition temperature was obtained with 0.07 wt% Ti. This resulted in inclusions predominantly of Ti_2O_3 surrounded by Mn-depleted zone (MDZ) [9].

Also, with small amount of aluminum, the oxygen is available to form titanium oxides. When the $[Al][O]$ ratio allows the coexistence of galaxite and titanium oxides, the optimal acicular ferrite is obtained [7]. Earlier research shows that the oxygen content should be adjusted, since both too high and too low reduces the amount of acicular ferrite. Results show that a content of 300 ppm oxygen produced more acicular ferrite than both 60 ppm and 654 ppm. [10] Research has found that a Mo content of about 1.5 wt% and approximately 3 wt% Ni is considered optimal to decrease the transformation-temperature, resulting in high volume fraction of fine acicular ferrite and good toughness [2]. To produce a fine acicular ferrite microstructure with high strength and good toughness, increased alloying of Mn, Mo and Ni have shown a positive effect.

Since non-metallic inclusions often consist of several crystalline and amorphous phases it is difficult to decide which component is responsible for the nucleation and which effect, positive or negative, the elements possess. The microstructure of the inclusions will therefore be of special interest to obtain an understanding of their role in the nucleation. It is necessary to understand why acicular ferrite nucleate on inclusions and there are four major mechanisms to explain this. The four mechanisms are illustrated in Figure 3 [11].

1. The inclusions are inert surfaces, which lead to a reduction of activation energy, and ferrite nucleation is promoted. See Figure 3(a) [11]. Since the free energy of heterogeneous nucleation is higher at inclusions than at grain boundaries, naturally, the energy for homogeneous is much lower. The size and number of inclusions as a center for heterogeneous nucleation of acicular ferrite is therefore important to improve the metal microstructure [2].
2. A reduction in the activation energy for nucleation may also occur having good lattice matching between inclusions and ferrite. This is illustrated in Figure 3(b) [11]. A low mismatch strain between the ferrite/austenite and inclusion is suggested to be the best solution for nucleation to occur. This means, that the crystallographic planes for ferrite/austenite and inclusions should be parallel and their phases should have a simple crystallographic orientation relationship [2]. During earlier research the misfit between the ferrite matrix and the surface of the inclusions found in weld metals was calculated. TiO , TiN and the spinel $MnO \cdot Al_2O_3$ exhibited low misfit orientation relationship, while the α -MnS phase had a relatively high crystallographic misfit [7].
3. Figure 3(c) illustrates how inclusions may cause depletion of the different elements, such as manganese, from the austenite. If the concentration of manganese is decreased near the precipitated manganese-sulphide inclusions, the austenite zone is reduced and ferrite nucleation in a manganese-depleted zone (MDZ) is promoted. According to this, manganese-sulphide inclusions are regarded as active inclusions for nucleation of acicular ferrite. An illustration of acicular ferrite nucleated from an inclusion surface in a MDZ is showed in Figure 4 [2].

4. Austenite and inclusions have different thermal expansion coefficients ($\Delta\epsilon$), this may develop thermal strains near the inclusion-austenite interface [11]. These stresses cause strains in the steel matrix and it is expected that higher stress cause higher strains and easier nucleation of acicular ferrite. Some compounds have a larger difference in thermal expansion coefficients and are in this point of view more effective nucleants for acicular ferrite formation. See Figure 3(d) [2].

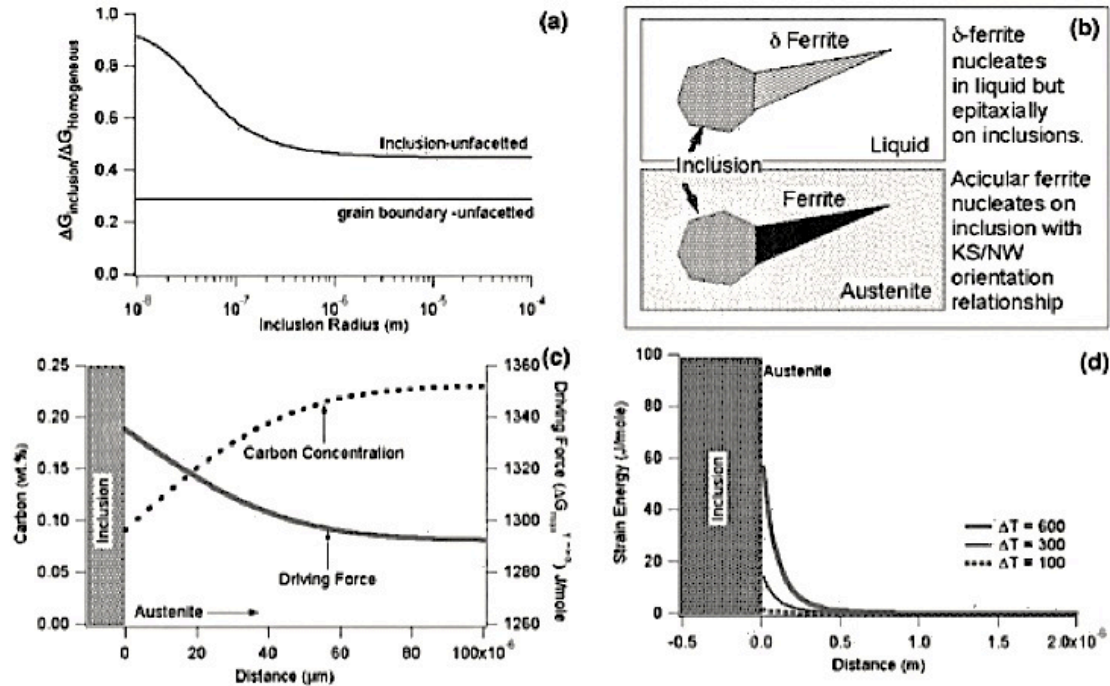


Figure 3. Illustrations of four mechanisms for nucleation of acicular ferrite [11].

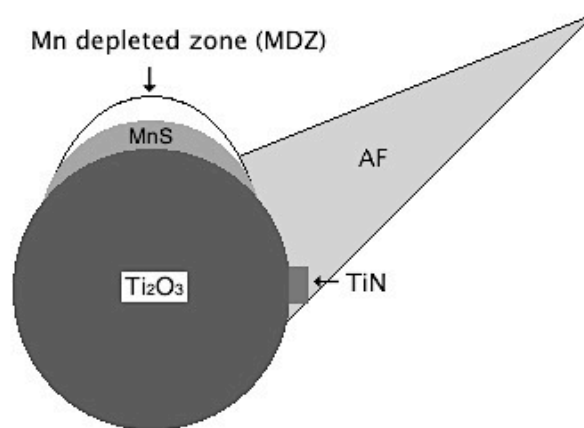


Figure 4. Illustration of nucleation of acicular ferrite.

From earlier research it have been recognised that factors controlling the acicular ferrite formation is austenite grain size, inclusion characteristic and alloying content [7]. Large austenite grain size is favourable in nucleating high fraction of acicular ferrite. By increasing the ratio between the surface areas of inclusions and grain boundaries, the

volume fraction of acicular ferrite increases. By increasing the grain size it limits the grain boundary area available for grain boundary ferrite and ferrite side plates [2].

The chemical composition of the inclusions influence the formation of acicular ferrite and is in most cases determined by the factors described in the previous section and Figure 3 (a-d). There are many types of inclusions based on their chemistry. Inclusions can be classified as active or inert depending on their capability to nucleate acicular ferrite. This is summarized in Table 1. Most of the acicular ferrite nucleants in steel have diameters in the range of 0.5-0.8 μm , even though larger inclusions ($>1.0 \mu\text{m}$) have larger probability for ferrite nucleation [2].

Another important factor to obtain a fine microstructure with high volume fraction of acicular ferrite is the number of active inclusions in the steel. Since research show that larger number of acicular ferrite nucleants is between 0.5-0.8 μm , it is desired to have most of the inclusions in this size range [2].

Table 1. Active and inert inclusions in steel based on their chemical composition [2].

Compound	Active inclusions	Inert inclusions
Simple oxides	Ti-oxides (Ti_2O_3 , TiO , TiO_2)	Al_2O_3 , SiO_2 , Ti_2O_3 (in Mn- free steel)
Complex oxides	$(\text{Ti}, \text{Mn})_2\text{O}_3$ TiO_2 -(MnO - Al_2O_3) Galaxite spinel MnO - Al_2O_3	MnO - Si_2 , MnO - FeO_x - SiO_2 MgO - Al_2O_3 MnO - Al_2O_3
Simple nitrides	TiN VN	TiN
Simple sulphides		MnS CuS
Complex oxy-sulphides and multi-phase inclusions	Al_2O_3 - MnS , Ti_2O_3 - Al_2O_3 - MnS Ti- and Ti-Ca-oxy-sulphides Ti_2O_3 - TiN - MnS , TiO_x - TiN - MnS FeS -(Mn , Cu) S MnS - VC , MnS - $\text{V}(\text{C}, \text{N})$	

2.6 Growth of acicular ferrite

When the primary microstructure is formed it mainly consists of allotriomorphic, Widmanstätten, idiomorphic and acicular ferrite. The allotriomorphic is the first phase to form and nucleates at columnar austenite grain boundaries. When the temperature decreases the diffusional growth of ferrite slows down. The remaining austenite transforms into Widmanstätten and acicular ferrite [12]. Plates of acicular ferrite will grow from repeated nucleation of ferrite subunits by displacive transformation. During this formation the carbon will escape to the austenite. The austenite will be enriched during the growth of acicular ferrite until the carbon content reaches a limit beyond

which it is impossible to have displacive formation. This occurs when the free energy of the austenite is equal to the stored energy in ferrite (400 J/mol) [11].

2.7 Bainite

Decomposition of austenite at temperatures above M_s (temperature where the martensite nucleation starts) results in formation of bainite. Acicular ferrite and bainite has some similarities, as described in previous chapter 2.4. The main difference is that bainite nucleate from grain boundaries and are non-lamellar aggregates with plate-shaped ferrite. These ferrite plates are about 10 μm long and 0,2 μm thick. Bainite can be divided into two types, upper bainite (UB) and lower bainite (LB). Upper bainite consists of cluster of platelets of ferrite with almost identical crystallographic orientation, resulting in low-angle boundaries. The cementite will only precipitate between the ferrite plates, while the ferrite itself is carbide free. The cementite will form a continuous layer between the ferrite and the amount will depend on the carbon concentration in the alloy. This cementite is coarse and nucleate cleavage cracks and voids [5].

The thin plates of ferrite help to minimize the strain energy in the material. By adding sufficient quantities of silicon or aluminum the formation of cementite will retard and the formation of cementite may be suppressed. This result in a structure called lower bainite, with good toughness because the brittle cementite is absent. Figure 5 gives a schematic illustration of upper and lower bainite.

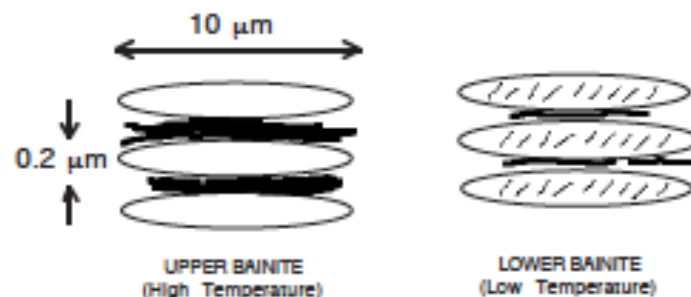


Figure 5. Illustration of upper and lower bainite.

Both the microstructure and the crystallographic features are very similar for upper and lower bainite. The main difference between them is that cementite also precipitates inside the ferrite plates in the lower bainite. The carbides found in lower bainite are extremely fine and since they precipitate inside the ferrite a smaller amount of carbon is partitioned into the austenite. The result is finer and fewer cementite particles between the ferrite plates. This is why lower bainite have better strength and toughness than upper bainite [5].

2.8 Optical microscopy

An optical microscope consists of a collection of lenses to dissolve details in an object and transfer this as a magnified image to the eye making it possible to distinguish the details. In addition of using the optical microscope to determine the type of microstructures present, it is possible to quantify the microstructure. By inserting a grid consisting of 100 junctions it is possible to count which microstructure is located underneath each of these junctions, and from this quantify the microstructure. This is illustrated in Figure 6.

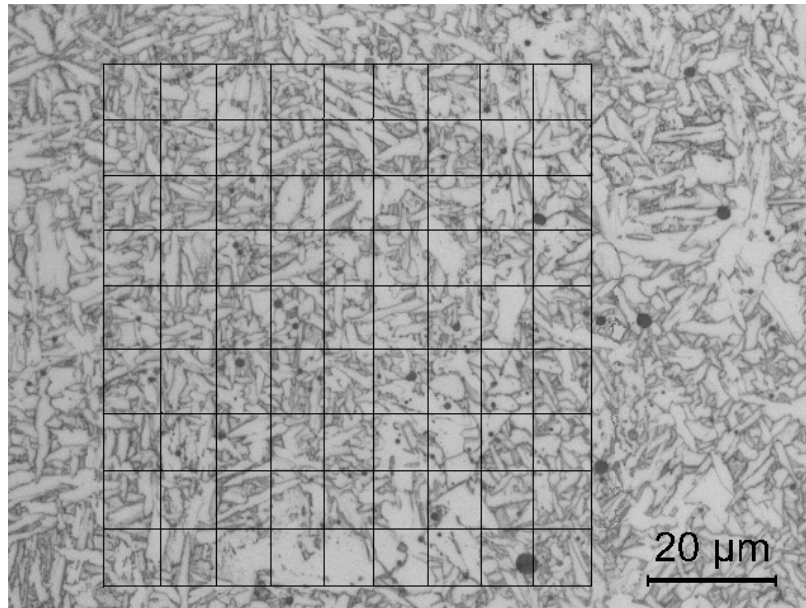


Figure 6. Illustration on how the quantification of the microstructure is done.

2.9 Fracture

A fracture occurs when an object is divided into two or more while exposed to stress. This process may be divided into two components; the crack initiation and the crack formation. A fracture can either ductile or brittle. The tendency to brittle fractures increase with decreasing temperature, increased strain rate and the triaxial stress state [13]. Such brittle fractures often occur rapidly without notice and may be catastrophic [14].

2.9.1 Brittle fracture

Brittle fractures occur in metals or alloys with high strength, or poor toughness and ductility. Metals considered as ductile may suffer a brittle fracture at low temperatures. Little or no plastic deformation is required and the fracture may move very rapidly, causing a sudden fracture [15]. These fractures have a surface texture with presence of facets resulting from grain boundary fracture or cleavage. Materials and their crystal structure will have certain crystallographic planes where the slip occurs, resulting in cleavage [16]. Chevron pattern, also called “river” pattern, is a common feature and cracks propagate from the origin [15]. This is illustrated in Figure 7.

Fractures may also be defined from the relationship between the grain structure and the path of the fracture. Fractures grown across of grains is called trans-granular fractures, but if the fracture has grown between the grains it is called intra-granular fracture. Depending on the amount of plastic deformation, trans-granular fractures may either be ductile or brittle. Intra-granular fractures are always brittle. If the grain boundaries are brittle, they may be susceptible to fracture [14].

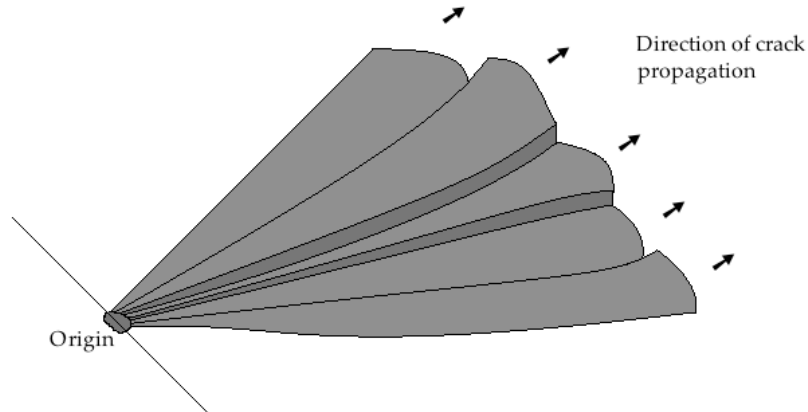


Figure 7. A common feature in brittle fractures is the Chevron pattern.

2.9.2 Ductile fracture

The ductility of a material is defined as the extent of deformation prior to fracture. The different factors influencing the plastic flow will affect the ductility of the material, such as temperature, grain size, strain rate, inclusions etc. [16]. A ductile fracture is often trans-granular in materials (metal) with good toughness and ductility. Prior to the fracture the material will be subjected to large amounts of deformation, including necking. By examining the fracture surface using a secondary electron microscope (SEM) a dimpled surface will be revealed. These dimples show the traces of the microvoids that were produced during the fracture [15]. This is illustrated in Figure 8.

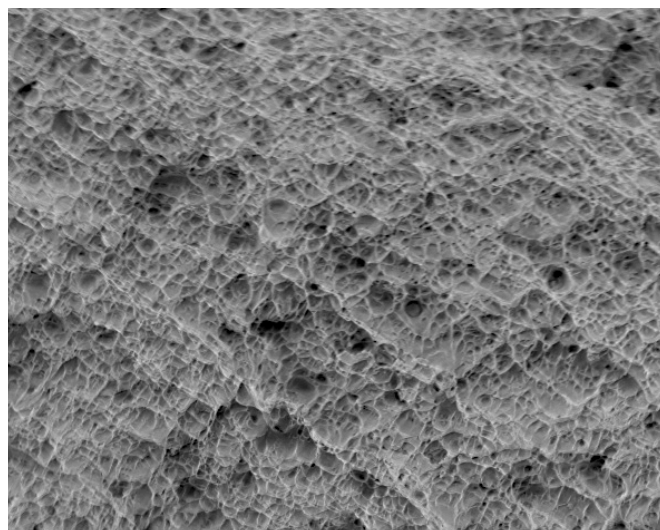


Figure 8. Macrograph from specimen 2.1 showing a ductile fracture after a Charpy V test.

2.9.3 Charpy V-notch test

When a specimen is subjected to an impact test it is often used to determine the brittleness of a material under certain conditions. One such test procedure is called Charpy test, where the specimen either is notched or un-notched. Figure 9 illustrates the dimensions of a notched specimen and how the test is performed. The test is performed by using a heavy pendulum, which starts at an elevation h_0 , swings through its arc, strikes and breaks the specimen, and then reaches a lower final elevation h_f . By knowing the initial and final elevations of the pendulum, it is possible to calculate the difference in potential energy. The difference is the impact energy absorbed by the specimen during its failure. This energy is usually expressed in joules (J) [17].

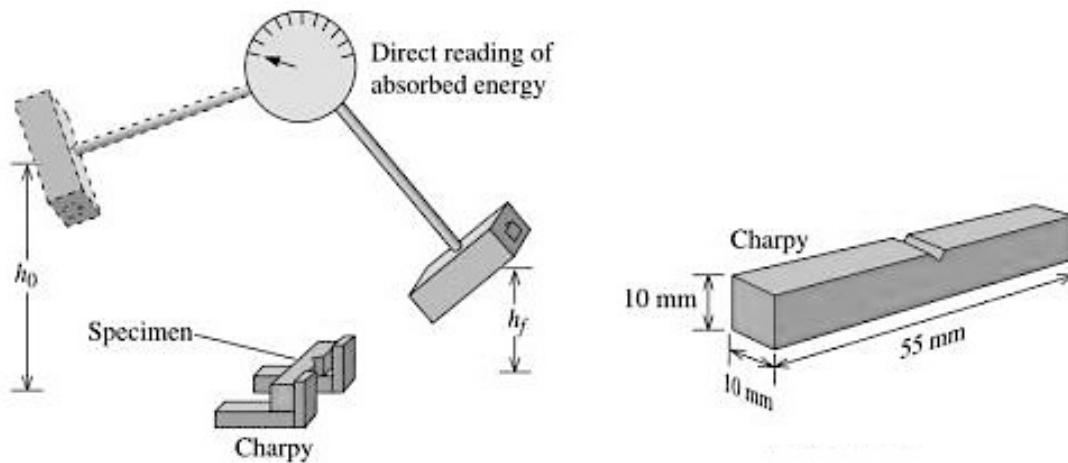


Figure 9. Charpy V-notch test and standard dimensions on the specimen [17].

The V-notched specimens are used to measure the resistance of the material to crack propagation. The impact toughness of the material is a measure on the ability to withstand an impact blow. The ductile to brittle transition is the temperature where the fracture changes from ductile to brittle. This is illustrated in Figure 10. The material subjected to an impact blow should have a transition temperature below the temperature to what the material is subjected to. Body centered cubic (BCC) metals have such a distinct transition temperature [17].

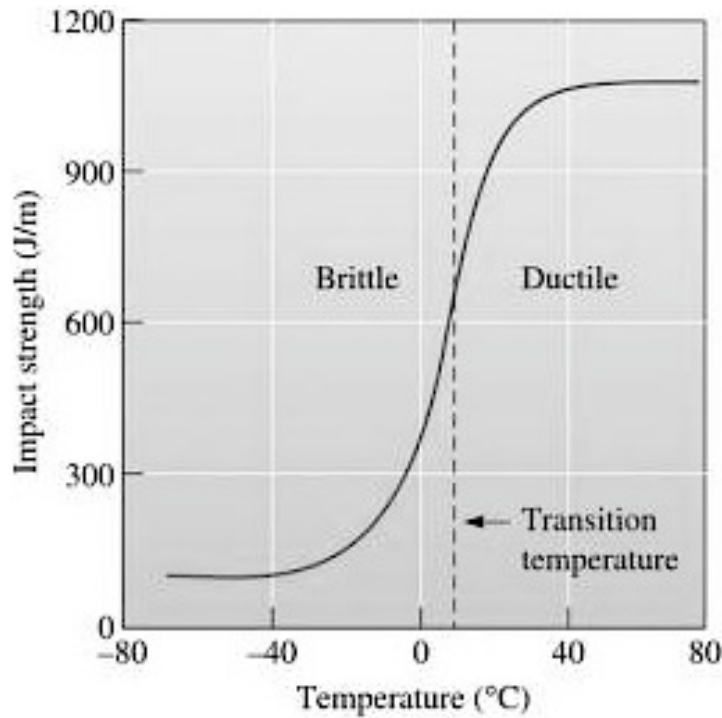


Figure 10. Ductile to brittle transition [17].

2.10 Scanning Electron Microscope

Scanning Electron Microscope (SEM) is an instrument used to observe the microstructure at magnifications not possible with optical microscope. Instead of using light to scan the surface of the specimen, it uses an electron beam and a detector to generate the image. When the beam hits the surface of the specimen, several signals are detected. This includes backscattered electrons, secondary electrons, auger electrons and x-ray radiation. When fracture surfaces are studied the depth of field is vital to obtain a good result and this is why the SEM often is preferred. The maximum height difference at a specimen surface where the image is focused is defined as the depth of field (D). This may be calculated through Equation (2). When the electron beam sweeps across the sample surface, the emission of secondary electrons vary as a function of the specimen surface topography, because of the good depth of field, it seems like the images are three-dimensional [18].

$$D = \left[\frac{\delta}{M} - d_p \right] \cdot \frac{1}{\alpha} \quad (2)$$

where δ is the resolution of the eye, M is the magnification, d_p the electron optical resolution and α the beam divergence. The resolution and the depth of field are two opposites, where one has to compromise when the other one improves. When the working distance (WD) is increased the D improves as it decreases α , but at the same time the resolution is reduced [18].

2.11 Electron Microprobe

This technique is a high performance thermal field emission electron probe micro analyser. It combines high SEM resolution with high quality X-ray analysis of submicron areas. The instrument used is equipped with an energy dispersive X-ray spectrometer (EDS) and 5 wavelength dispersive X-ray spectrometers (WDS). This makes it possible to analyse 16 elements EDS + 5 elements WDS and collect image signals from backscatter and secondary electron detectors. The WDS have high current and a small probe diameter and is capable to do extreme elemental analysis of sub-micron areas [19].

This method will give an elemental mapping of the specimen by the use of X-rays and give all the elements available at the area of interest. When the electron beam hits the sample, it emits X-ray photons. Every element in the sample has a characteristic X-ray with energy unique from others. The detector will collect all the different X-rays and this will produce a spectrum of elements. This is shown in Figure 11. It is possible to estimate the relative amounts of the elements from the size of the peaks [20].

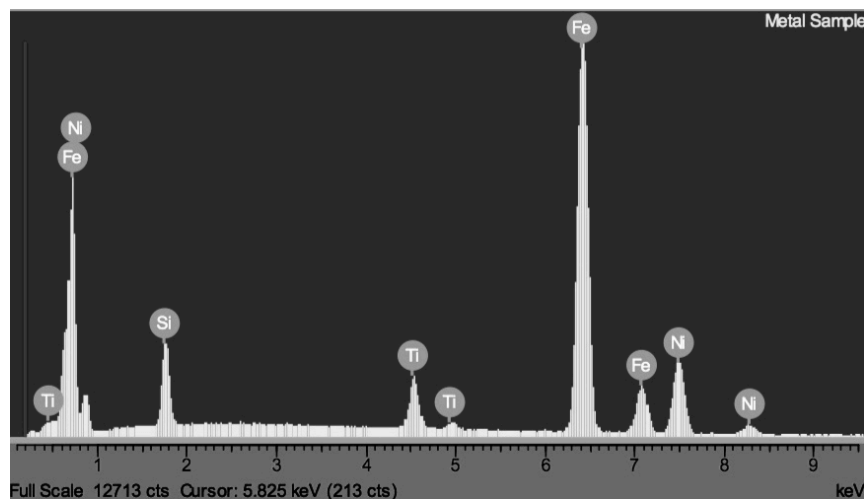


Figure 11. Example of X-ray spectrum [20].

2.12 Transmission electron microscope (TEM)

A transmission electron microscope (TEM) is capable of imaging the microstructure at a very fine scale. This technique has an ultimate of imaging and analysis of better than 0.1 nm and it combines different measuring techniques at the same time. It is possible to collect images, diffraction and different kinds of spectroscopy almost on the same time and from the same area [21]. Figure 12 illustrates the electron pathway in conventional TEM configuration.

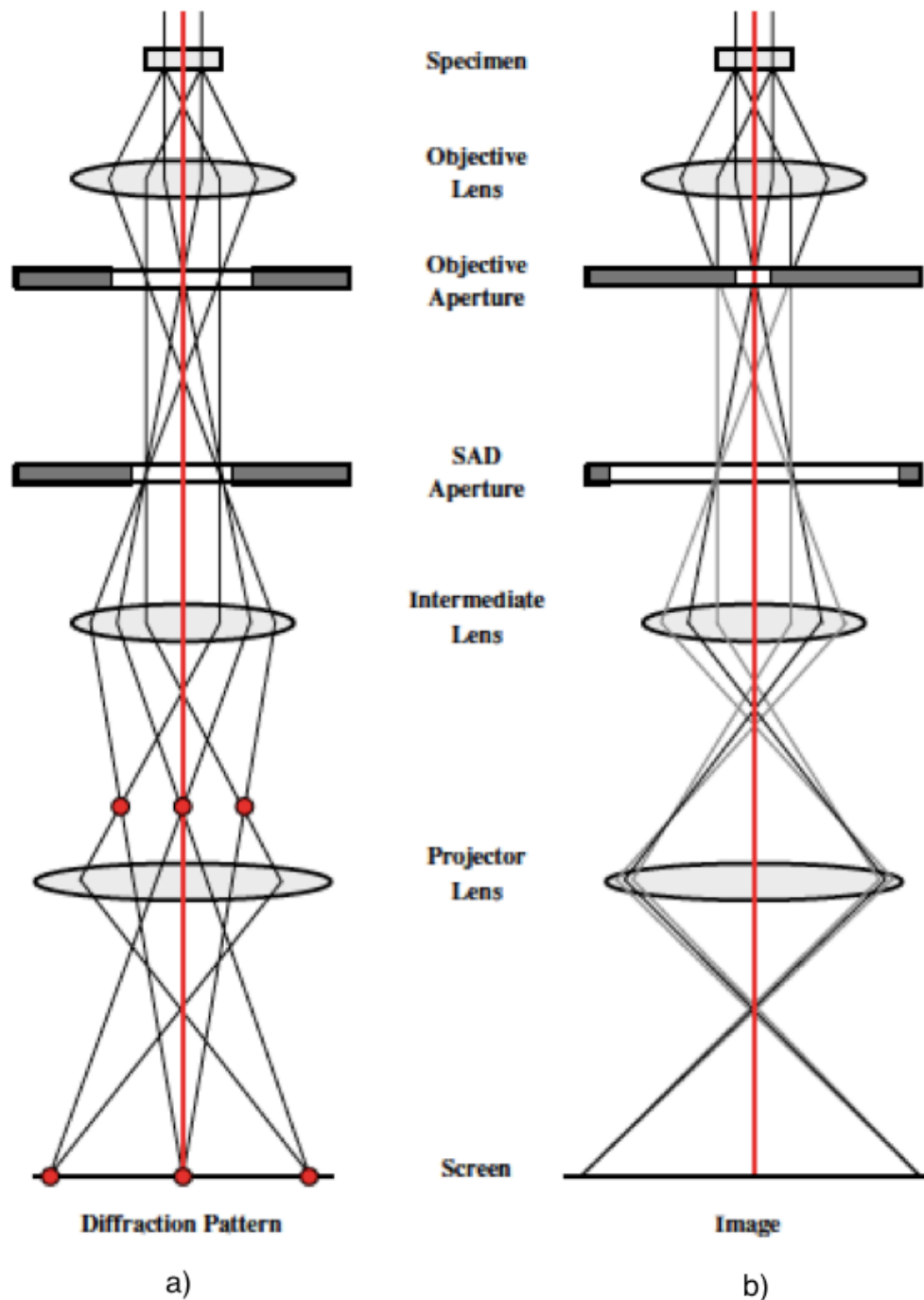


Figure 12. The TEM can be used to image the diffraction pattern of the specimen (a), or it can be used to image the specimen (b) [22].

For metallurgical analysis the instrument is often used to measure the size, composition and structure of the precipitates, since the mechanical properties of the alloy is crucial for it's usage and the precipitates can influence this. The precipitates are part of the microstructure and are important to understand the overall microstructure. It is also possible to study the boundary between the precipitations and the matrix or between different grains. It is essential for all transmission electron microscopy that the samples are sufficiently thin so that the electrons may penetrate the sample [21]. To make this possible it is standard to use a sample with a diameter of 3 mm, while the thickness

needs to be less than about 0,1 μm to allow most of the high energy electrons to pass through the sample without suffering too much energy loss. The TEM also uses electromagnetic lenses to make the final image observed on a fluorescent screen that converts the high-energy electron image to a visible image to the eye. It is also possible to record the image onto a film or use a digital camera. The whole electron microscope column must be kept under vacuum, since the high-energy electron beam has limited path length in air. A TEM has high spatial resolution, which makes it possible to determine different crystalline regions and between crystalline and amorphous regions at small length scales ($\sim 1\text{-}10\text{ nm}$). The diffraction mode in the TEM was used to determine the orientations and the STEM was used for composition analysis and mapping [23].

2.12.1 Diffraction patterns

The crystal structure of a crystalline material can be analyzed using electron diffraction. When the electron beam hits the specimen the electrons will spread away from the incident beam due to both elastic and non-elastic scattering (diffraction). In elastic scattering, also called Bragg-scattering, the direction of the electrons is altered, while in non-elastic scatter both the direction and speed (energy) is changed [21].

Atoms having regular formation relative to each other in a crystal lattice form a crystal. Each atom scatters the incident electron beam in all directions and it interferes either constructively or destructively in certain directions. The directions of constructive interference are dependent on the crystal structure and how the crystal is oriented relatively to the incident beam. Constructive interference occurs in a direction where the difference between successively reflected single-beams are similar to a whole number n wavelengths. This is expressed mathematically through Bragg's law:

$$2 \cdot d \cdot \sin \theta = n \cdot \lambda \quad (3)$$

where d is the interplanar spacing, θ is the incident angle and λ is the wavelength of the incident beams. n is the order of reflection [21].

When the TEM is set to diffraction mode a diffraction pattern is magnified and displayed on a fluorescent screen. The objective lens collects parallel beams in one point at the focal point of the lens, and a diffraction pattern arises. For every direction with constructive interference a point in the diffraction pattern occurs. In diffraction images from thin specimens only reflections are seen, but from thicker specimens two other effects are also observed, one light diffuse background intensity containing dark and bright lines called Kikuchi pattern [21] (Figure 13).

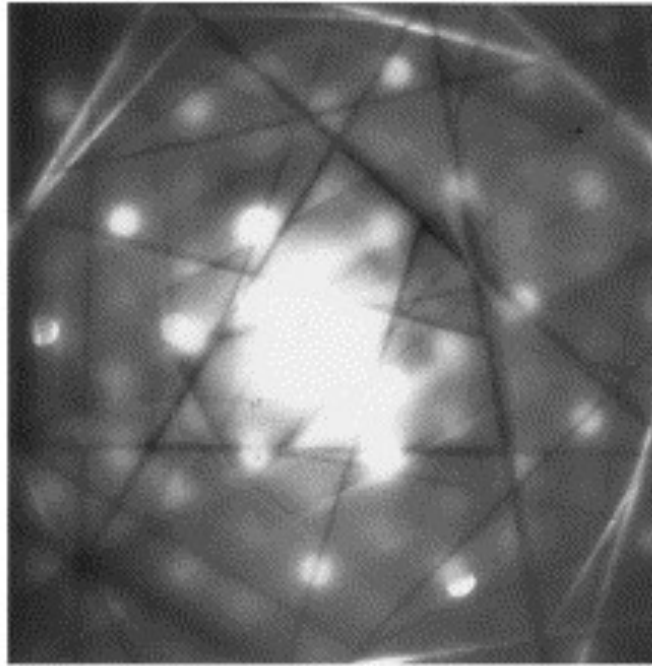


Figure 13. Example of Kikuchi pattern in TEM [24].

It is possible to observe patterns with reflections originating from several orders “n” from the same lattice, even though Bragg’s law says that only one reflection is obtained from one set of planes at the same time. This makes it possible to observe familiar diffraction patterns as illustrated in Figure 14. This is a result caused from three things [21]:

- The incident beams are not completely parallel
- The sample is always bent
- Deviations from Bragg’s law may occur on such thin specimens

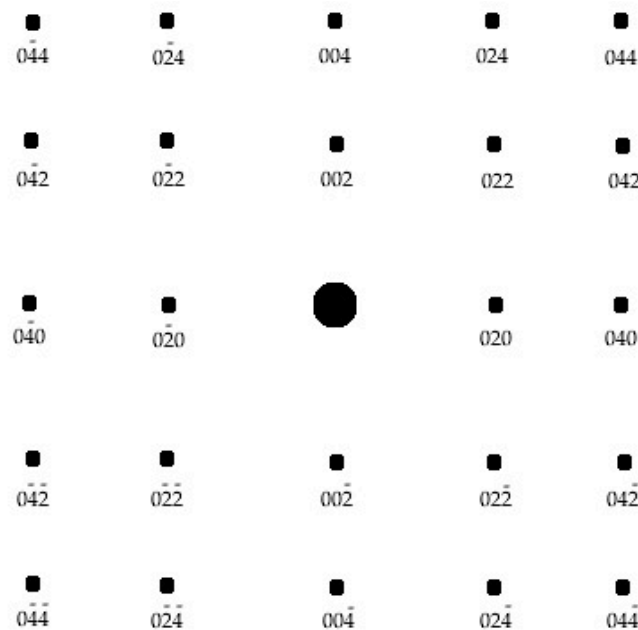


Figure 14. FCC diffraction pattern with incident beam along the $[100]$ direction.

There are also extinction rules for both FCC and BCC crystals.

FCC	Allowed reflections:	hkl all even or odd (example: 224)
	Forbidden reflections:	hkl mixture of even and odd (example: 310)
BCC	Allowed reflections:	$h + k + l = \text{even}$ (example: 110)
	Forbidden reflections:	$h + k + l = \text{odd}$ (example: 111)

2.12.2 Particles in TEM

TEM is an excellent instrument to investigate small inclusions in a specimen because of the possibility to use a large magnification and the use of diffraction from very small areas. Particles in a steel matrix are incoherent meaning that they have a different crystal structure than the surrounding matrix, and therefore satisfy different diffraction conditions. The diffraction contrast produced by elimination of diffracted electrons, with an objective aperture, makes diffracting regions of the sample appear dark. Particles will appear dark in the image. The corresponding diffraction can be obtained and this gives information about the crystallography and orientation of the precipitate. When the bright field is used, the particle will be imaged darker than the surrounding matrix [21]. This is illustrated in Figure 15. It is opposite when the dark field function is used.

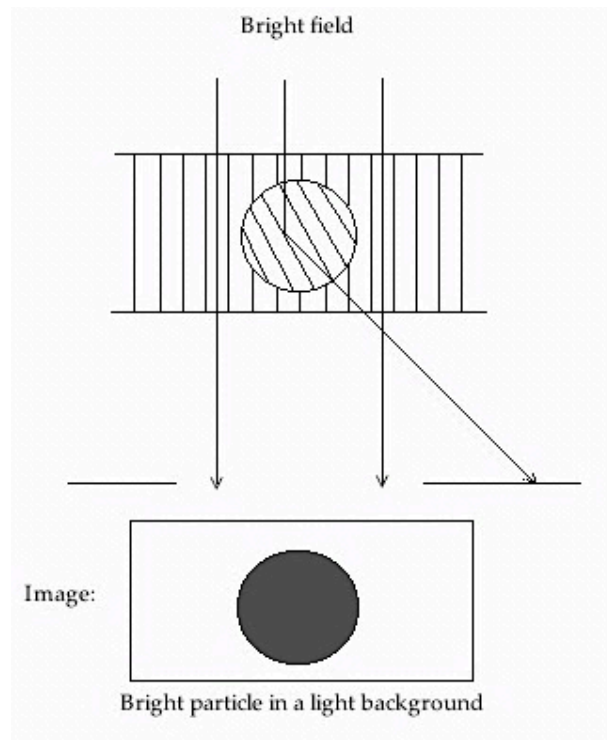


Figure 15. Imaging of a particle in bright field.

Chapter 3 Experimental work

3.1 Materials

The base metal used in this experiment is the same for all three welds and is a 50 mm thick plate of 420 MPa HSLA-steel (High Strength Low Alloy steel). The chemical composition of the base metal is shown in Table 2. Results from earlier experiments on these weld metals show both the Charpy V notch toughness and fracture toughness from CTOD tests varied between the specimens [25].

Table 2. Alloying elements in base metal [26]

Chemical composition (%)																
C	Si	Mn	P	S	Cu	Ni	Cr	Mo	Ti	B	Al	As	V	Sb	Pb	Nb
0.05	0.33	1.35	0.015	0.005	0.23	0.97	*	*	*	*	*	*	*	*	*	*

* Below specified minimum

As shown in Table 3 there are some variations in the chemical composition of the three different weld metals. Notice especially the variations of manganese, nickel, molybdenum, aluminum and titanium content. Additional analysis of the oxygen content showed that there were significant variations in the three welds. This is illustrated in Table 4.

Table 3. Chemical composition (wt%) of weld metal [25].

Weld No.	C	Si	Mn	P	S	Ni	Mo	Al	Ti	N
2.1	0.07	0.30	1.12	0.006	0.006	2.47	0.009	0.006	0.065	0.005
3.1	0.06	0.26	1.12	0.006	0.001	1.00	0.009	0.92	0.003	0.028
5.2.1	0.06	0.27	1.65	0.010	0.003	0.80	0.12	0.013	0.002	0.004

Table 4. Oxygen content in weld metal [27].

Element	Specimen 2.1	Specimen 3.1	Specimen 5.2.1
Oxygen (ppm)	530	120	350

The welding was done with half-V grooves and was prepared by gas cutting. Test panel 2.1 and 5.2.1 was welded in a flat horizontal position (PF), while test panel 3.1 was done in a transverse position (PC). Both positions are illustrated in Figure 16. Since the specimens were too big to fit into the specimen holders to use in the automatic grinding machine, the specimens were cut into smaller

parts. This included cutting across the weld, since the below area not needed to be examined. Figure 17 show how the specimens were cut. The identification of the three specimens is outlined in Table 5, while the welding parameters are shown in Table 6.

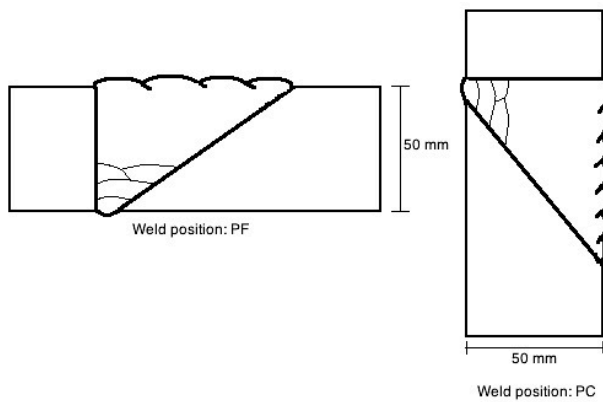


Figure 16. Weld positions used for the specimens.
Horizontal position on the left and transverse position on the right.

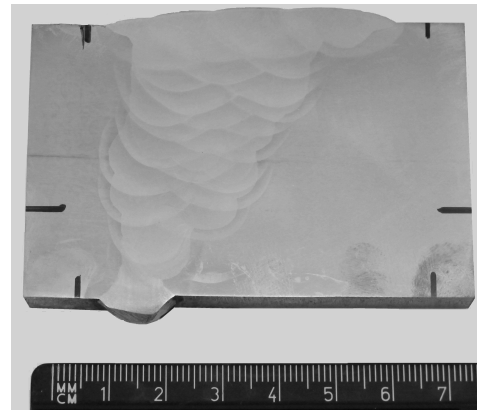


Figure 17. Photograph of marked specimen before reduction.

In addition, there was one specimen of each weld, which had been tested for fracture toughness by performing Charpy V-notch tests. Figure 18 shows how the specimens looked after the Charpy-tests.



Figure 18. Charpy V-notch specimens of all three welds.

Table 5. Identification of test panels [26].

Test panel number	Identification	Welding process	Wire
2.1	WS160F02 – 50E	GS-FCAW	*
3.1	WS160C10 – 50	SS-FCAW	NR 203 Nil
5.2.1	WS160A23 – 50A	SAW	OK15.24S

* Not a commercial wire, still under development.

Table 6. Welding parameters [26].

Test panel number	Max. interpass temp (°C)	Current (A)	Voltage (V)	Travel speed (mm/s)	Heat input (kJ/mm)
2.1	65	230	24-25	2-3	2.5
3.1	92	275	22	4.1	1.5
5.2.1	250	650	28	7.3	2.5

3.2 Sample preparation

Cutting of the specimens was done with Struers Discotom-5. The grinding and polishing of the specimens before optical microscope examination was done with Struers TegraPol 31 and were used with an automatic program. The following preparation steps were done.

- Grinding with SiC-paper from #80 to #2400.
- Polishing with MOL 3 μm .
- Polishing with NAP 1 μm .
- Etching for 1 minute in a 2 % Nital solution.

The Charpy V-notch specimens were cut into smaller parts, using the Discotom 2, since specimens going into the SEM should not be higher than 2 cm. This is to ensure that none of the parts inside the chamber was damaged. The surface was a fracture surface, and had therefore limited possibilities of cleaning before the examination in the SEM. The specimens were rinsed in acetone for 10 minutes using a electrolyte bath prior to the SEM investigation.

Before the specimens were examined in the TEM each specimen was cut into smaller samples of 1x2 cm and 1 cm thick, by using the Discotom 2. The Acutom 5 was then used to cut the specimens into a thickness of $\sim 1 \mu\text{m}$. After the specimens were cut they were grinded with SiC-paper from #120 to #2400 making the specimen as thin as possible. After this there were made several discs with a diameter of 3 mm from the original specimen 2.1, 3.1 and 5.2.1. Since the weld metal consist of several areas, each consisting of different microstructures, it was desired to cut the disc in such a way that

if was possible to know which area it originated from. All discs from the three specimens that were cut should originate from the primary weld metal. It is impossible to see where the primary weld metal ends and the reheated coarse-grained weld metal start without using a microscope to magnify the microstructure and is therefore difficult to do. Figure 19 shows how the original specimen was cut and how the discs from one of the specimens were stamped.

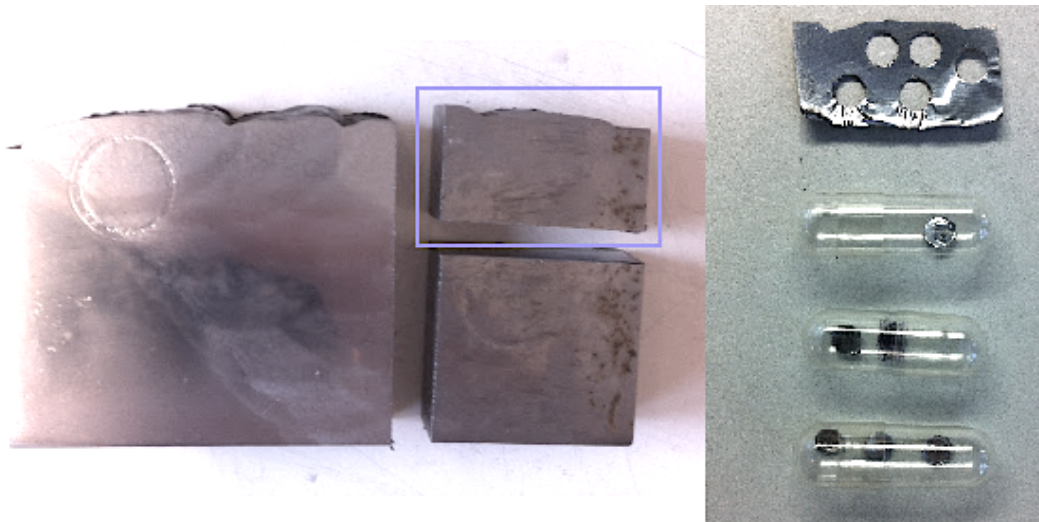


Figure 19. Illustration of how the specimen was cut. The marked part was the one prepared for TEM-investigation.

All discs where electro polished using Struers Tenupol-5 with the installed program Struers Method for low carbon steel. Table 7 shows the parameters used for the polishing. The specimens were polished from both sides simultaneously to achieve a thin foil with a center hole as small as possible. The thinning was controlled by an infrared light source, stopping the process as soon as the first light was able to pass through the established hole. Immediately after the polishing the specimen holder where placed in a container of methanol to rinse of, the specimen was then removed from the holder and rinsed in a new methanol container. The specimen was finally flushed with ethanol and dried.

Table 7. Parameters for electro polishing.

Parameters	Struers Method (low carbon steel)
Electrolyte	A8
Temperature	15 °C (22.8 °C)
Voltage	50 V
Time	No limit
Light stop value	Auto
Pump flow rate	16
Flow mode	Single flow
Graphic time scale	Auto

* A8: 50 ml perchloric acid, 950 ml ethylene glycol monobutylether

In addition, it was decided to do additional ion thinning on the specimens to achieve a large, thin area to examine in the TEM. The procedure is outlined in Table 8. The machine used to do this was Gatan Model 691 Precision Ion Polishing System (PIPS). The system is designed to produce high quality, TEM specimens with large electron transparent areas. It uses two penning ion guns with 10° to -10° milling angles, variable energy milling, liquid nitrogen to avoid heat built-up in the specimen and an oil-free vacuum system to obtain a clean specimen processing. The specimen were cooled to about -100°C .

Table 8. Procedure for ion thinning in PIPS.

Step	Time (min)	Beam energy (keV)	Angle gun (degrees)	Rotation (rpm)
1	30	3	4	1
2	10	2.5	4	1
3	10	1.5	4	1

3.3 Optical Microscope and SEM

All specimens had a microstructural characterization and where examined using Leica DM500 M. The area of interest was the fusion zone; consisting of both the primary and reheated weld metal. This is illustrated in Figure 20. In addition the microstructure were quantified to see the difference between primary weld metal and reheated weld metal. When quantifying the microstructure a grid consisting of 100 junctions where used to count which type of microstructure was underneath each junction. Three areas were examined in each specimen; primary weld metal, coarse-grained weld metal and fine-grained weld metal. In all areas five measurements were performed to ensure a valid result.

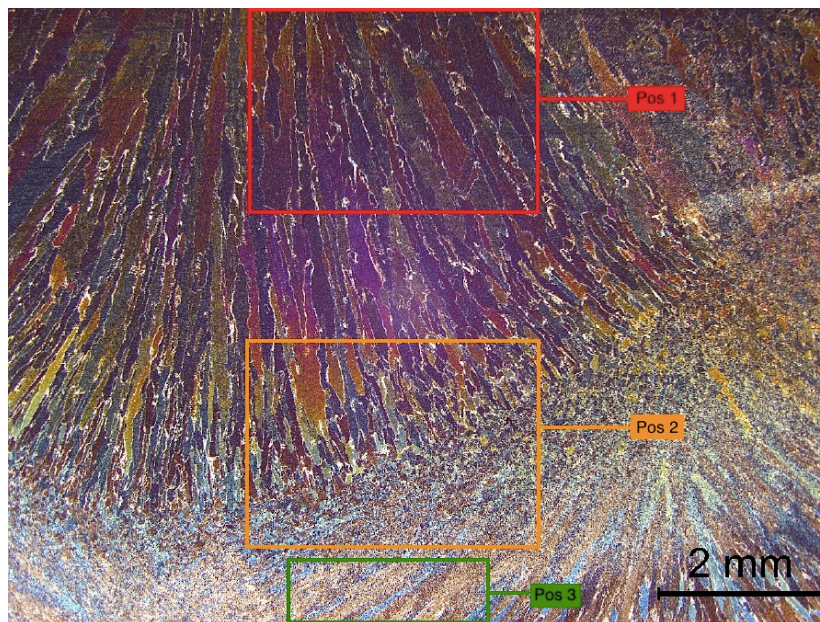


Figure 20. Illustration of primary WM in pos. 1 (red), reheated WM in pos. 2 (yellow) and partially reheated WM in pos. 3 (green).

The microscope used for the SEM-analysis was a Zeiss Gemini Supra 55VP LVFESEM, which is a Low Vacuum Field Emission Scanning Electron Microscope. All specimens were examined from one edge to the other, and from the machined V-notch and further into the cracked material. The examination was done with secondary electron imaging and Table 9 gives an overview of the parameters used for the examination of the specimens. It was decided to use a large aperture and long working distance to achieve the best possible depth of field, in addition high current were used. The images were taken at relatively low magnification (50-1000X) and the resolution was not affected too much by these settings.

Table 9. Parameters used in SEM.

Operation mode	SE
Acceleration voltage	10 kV
Working distance (WD)	34-40 mm
Aperture diameter	300 μm
Current mode	High current
Tilting	0°

3.4 Electron Microprobe

To analyze the chemical composition of the non-metallic inclusions the Jeol JXA-8500F Hyperprobe were used. Since this equipment is very complicated and difficult to use it requires a trained operator. The system is highly automated and controlled by a powerful SUN workstation system. Both backscatter and secondary electron images were collected in addition to the element analyze in the same areas [19]. All three specimens were examined for the following elements, Oxygen, Titanium, Manganese, Magnesium, Sulfur, Aluminum, Iron, Nitrogen, Copper, Carbon, Calcium, Zirconium and Silicon.

3.5 Size distribution

The backscatter images captured in the microprobe were further used to decide the size distribution of the inclusions. The images were examined in the computer program Solution DT. This program analysis all pixels in the grey-scaled image and combine automatic and manually control of the settings. The result from this analysis was then transferred to a Microsoft Excel worksheet and a diagram presenting the results was constructed.

3.6 Transmission electron microscopy

The specimens were examined in a Jeol-2100F transmission electron microscope (TEM) operating at 200 kV. Standard specimens with a diameter of 3 mm and with a thickness around 0.1 μm were examined. This equipment requires great understanding and long experience to achieve good results. In addition there were time limitations in this thesis and it was therefore decided to use an experienced operator to do the examination in collaboration with the author. The interesting areas was examined and discussed together to achieve the desired results from the examination. Different modes were used during the examination, microscope mode (bright field and dark field), diffraction mode and STEM.

An Oxford Instruments X-Max X-ray detector was used for composition measurement. The INCA EDX software was used to record the chemical analysis and store it as composition maps, along with Annular Dark Field (ADF) images of each inclusion that was examined. The maps contain complete X-ray spectra of each pixel in the map and the composition distribution within the particle can be displayed for each element. This information can be combined with diffraction to identify the phases that are present.

3.7 Indexing of the diffraction patterns

To index the different diffraction patterns collected from the TEM two programs were used. One was the Gatan Digital Micrograph 2.31, that was used to measure the lengths x and y as illustrated in Figure 21 that are used to measure the interplanar spacing, d . The other program was MacTempasX that was used to simulate electron diffraction patterns and compare the theoretical d with the one calculated from Equation 4 using experimental data from the diffraction patterns and finally index the diffraction patterns.

To index the diffraction patterns from the inclusions it was necessary to use a reference to calibrate the collected diffraction patterns. In this report a silicon sample with a known reciprocal lattice, was used. The information needed on the silicon sample is listed in Table 10. The needed information to index the composition of the unknown diffraction pattern was extracted from the X-ray laboratory. There were some compositions that were expected and the documents of the one used in this report are attached in Appendix C. The calibrated Si diffraction pattern was used to calculate the different d -values for the experimental diffraction patterns. The formula for this is showed in Equation (4).

$$d = 1.92 \text{ \AA} \cdot \frac{x_{Si}}{y_u/r} \quad (4)$$

where x_{Si} is the length of the red line in Figure 21 and y_u is the length of the red line in the unknown pattern illustrated in Figure 21. r is the number of reflections that the line stretches over. The two red lines stretch over several reflections to achieve a more precise d .

Table 10. Silicon sample used for calibration.

Sample	d (Å)	r	X_{Si} (pixel) / r
Silicon (Si)	1.92	4	$1321, 3 / 4 = 330,325$

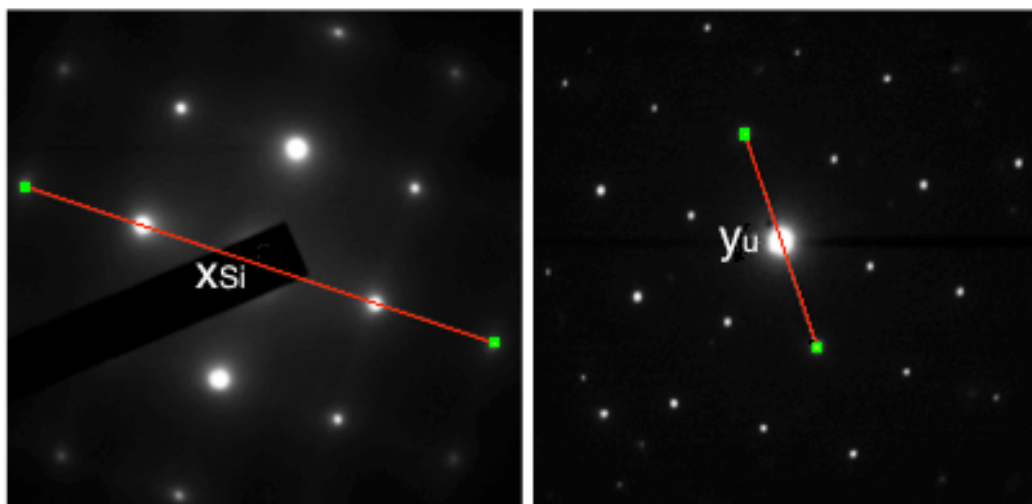


Figure 21. Diffraction pattern of calibrated Si illustrating the length x_{Si} and a experimental diffraction pattern with the length y_u from the unknown composition.

It was decided to measure three different d-values in each diffraction pattern and compare them to three theoretical d-values to see if they correspond well with each other. The inclusion with the two interesting areas is shown in Figure 22. To get the d-values this it was necessary to measure three y-lengths in both experimental diffraction patterns, this is shown in Figure 23. From this it was possible to calculate the zone axis and construct a theoretical diffraction pattern and compare this to the experimental patterns. Zone axis orientations were studied where diffraction vectors were present in two directions and indexed consistently by comparison with the simulated patterns.

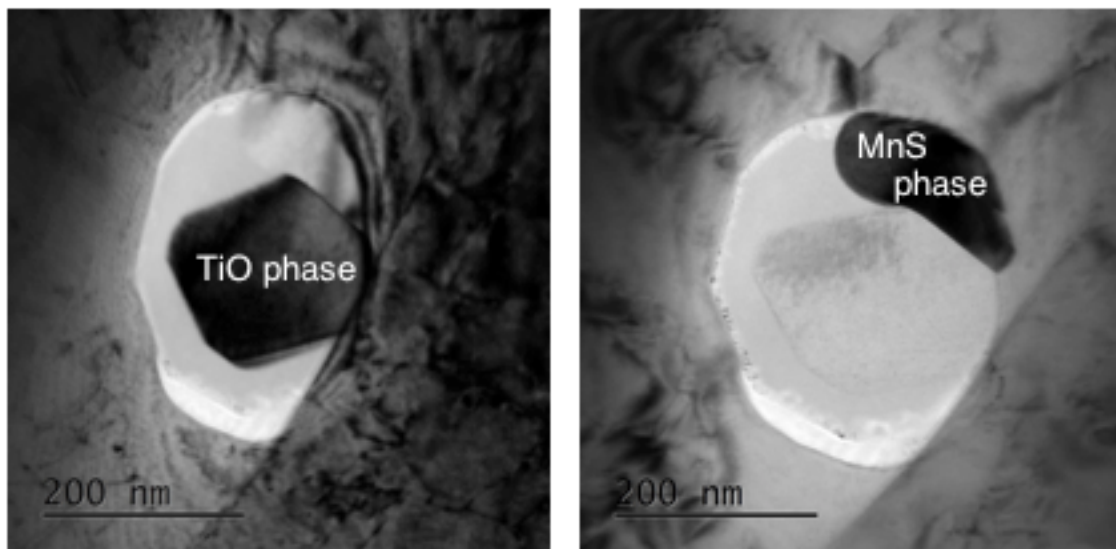


Figure 22. Non-metallic inclusion in specimen 2.1 examined to determine the different compounds inside. It was expected to find a titanium oxide core and manganese sulphide on the edge.

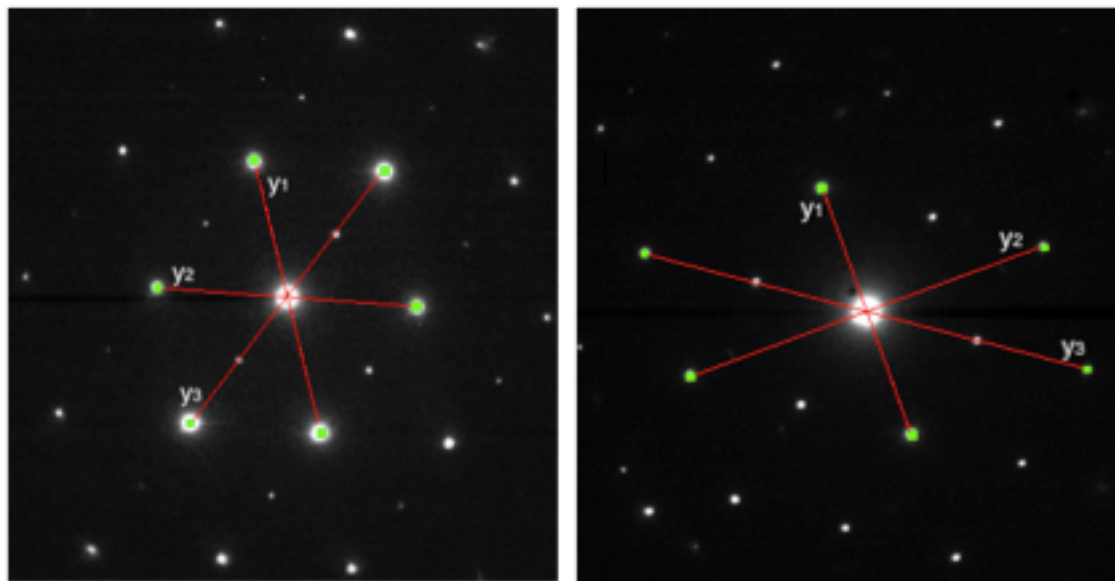


Figure 23. Diffraction pattern from the titanium oxide core (left) and the manganese sulphide (right) with length y_1 , y_2 , y_3 .

Chapter 4 Results

4.1 Microstructural characterization and quantification

This examination was done during the specialization project, but is presented here to provide clarity to the other results. The examination of the microstructure was done both of the primary weld metal microstructure and the reheated microstructure. The primary weld metal of specimen 2.1 is shown in Figure 24 and mainly consists of acicular ferrite (AF) with some polygonal ferrite (PF) and grain boundary ferrite (GBF). It is possible to see the inclusions that nucleate acicular ferrite as small dark spots in this figure. The coarse-grained reheated weld metal also consists of acicular ferrite, as shown in Figure 25. The fine-grained reheated weld metal shown in Figure 26 contains a mixture of acicular ferrite and polygonal ferrite.

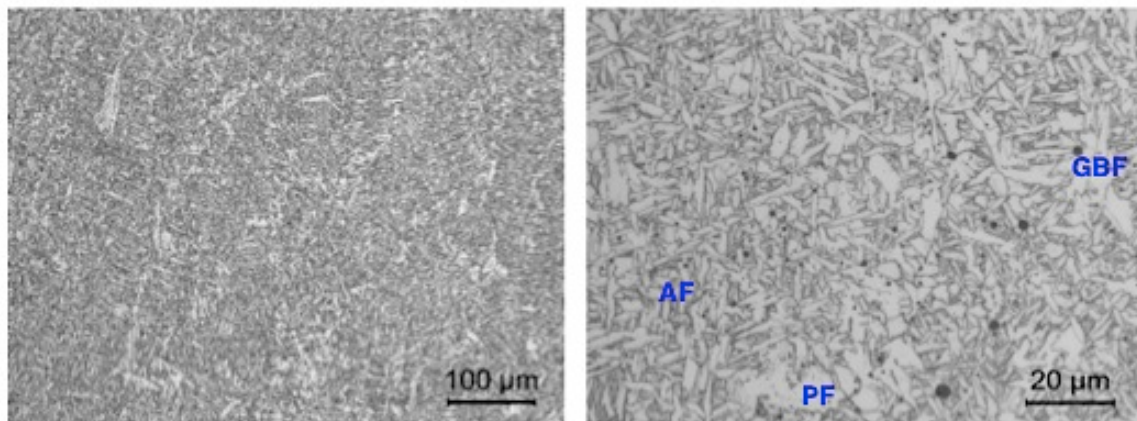


Figure 24. Primary weld metal of specimen 2.1.

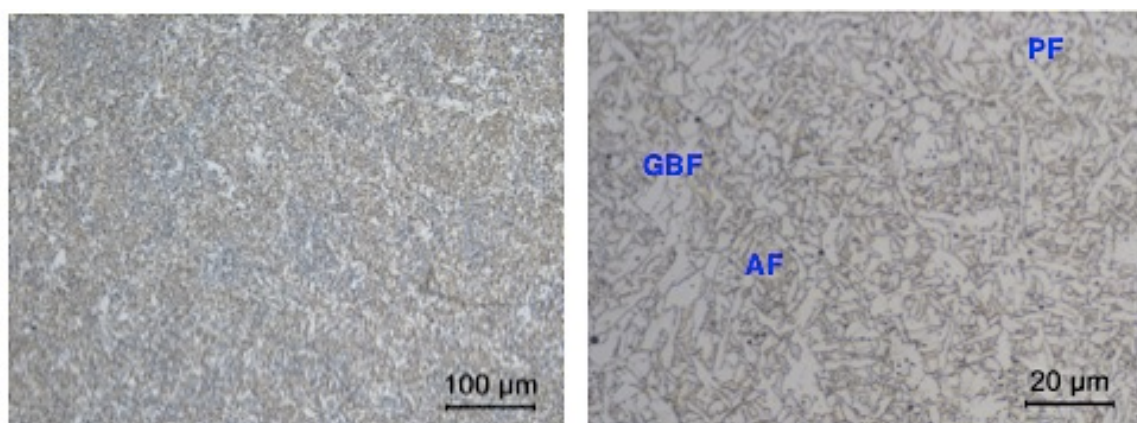


Figure 25. Coarse-grained weld metal of specimen 2.1.

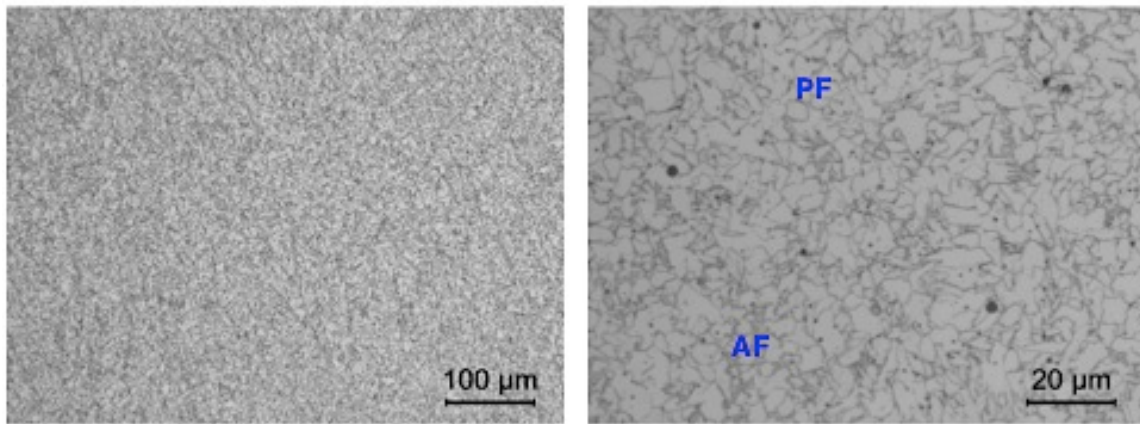


Figure 26. Fine-grained weld metal of specimen 2.1.

Specimen 3.1 was welded with a self-shielded wire and was done without any extra shielding gas. This wire contained 0.9 %Al. The primary weld metal microstructure consists of upper bainite (UB), polygonal ferrite and a limited amount of acicular ferrite, as shown in Figure 27. Figure 28 show that the acicular ferrite is almost absent in the coarse-grained reheated weld metal, and has instead formed coarse upper bainite and polygonal ferrite. Figure 29 show that the fine-grained reheated weld metal also is a bit coarse. Some upper bainite is observed in the microstructure.

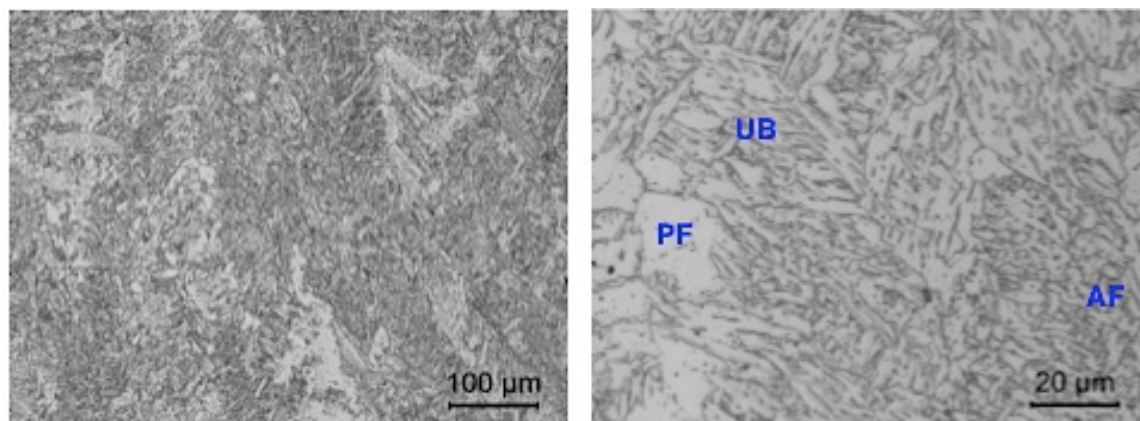


Figure 27. Primary weld metal of specimen 3.1.

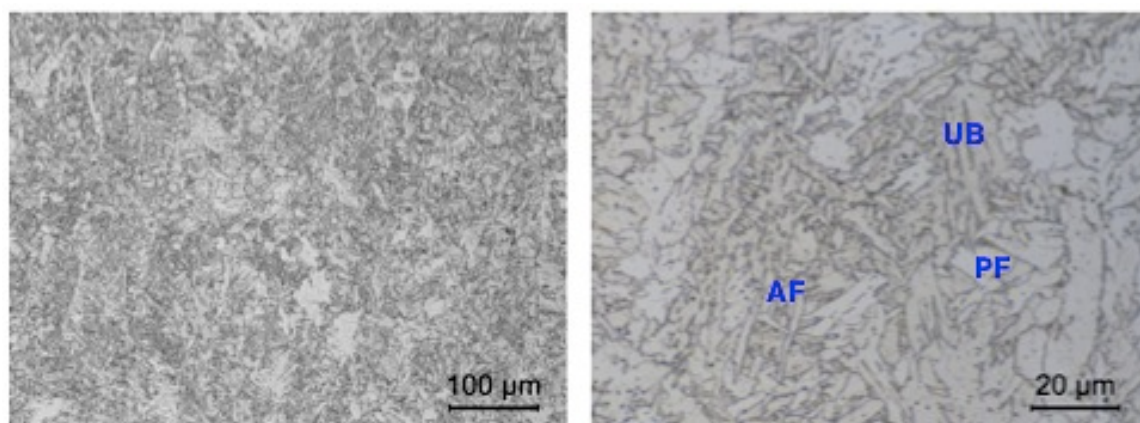


Figure 28. Coarse-grained weld metal of specimen 3.1.

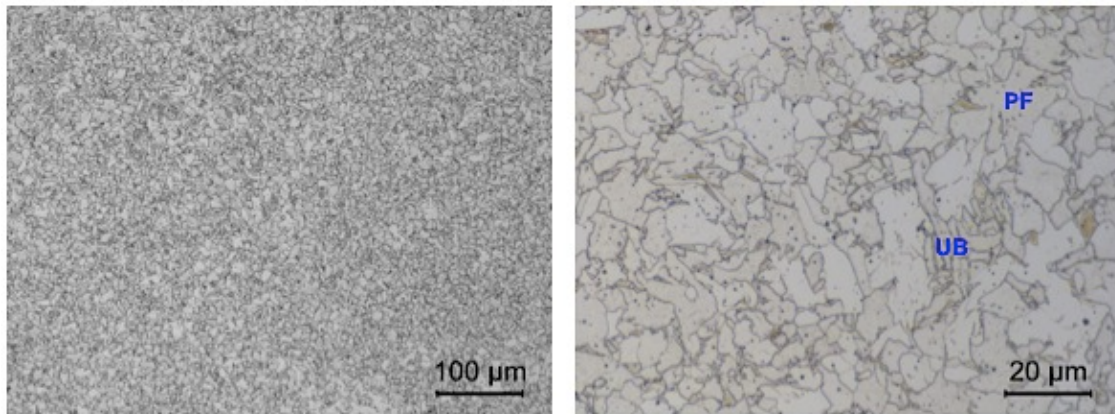


Figure 29. Fine-grained weld metal of specimen 3.1.

The third specimen, 5.2.1, was welded with submerged arc welding, using a flux-cored wire. The primary weld metal contains a mixture of microstructures, with polygonal and grain boundary ferrite, which decorate the austenite grains. Also some Widmanstätten ferrite (WF) is observed. The interior of the grains consists of acicular ferrite and polygonal ferrite. This is shown in Figure 30. Figure 31 shows the coarse-grained weld metal, which are a bit coarser, but with high volume fraction of acicular ferrite and some polygonal ferrite. In the fine-grained weld metal the dominating microstructure is polygonal ferrite, with the presence of acicular ferrite. This is shown in Figure 32.

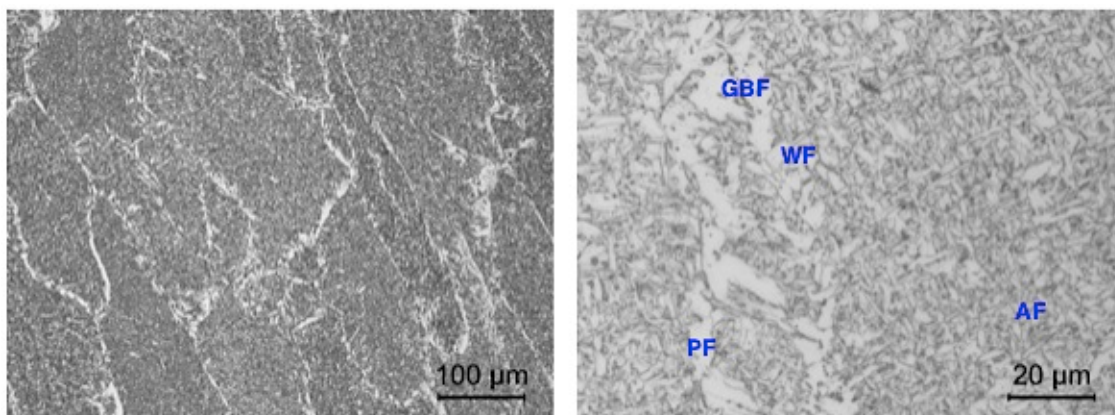


Figure 30. Primary weld metal of specimen 5.2.1.

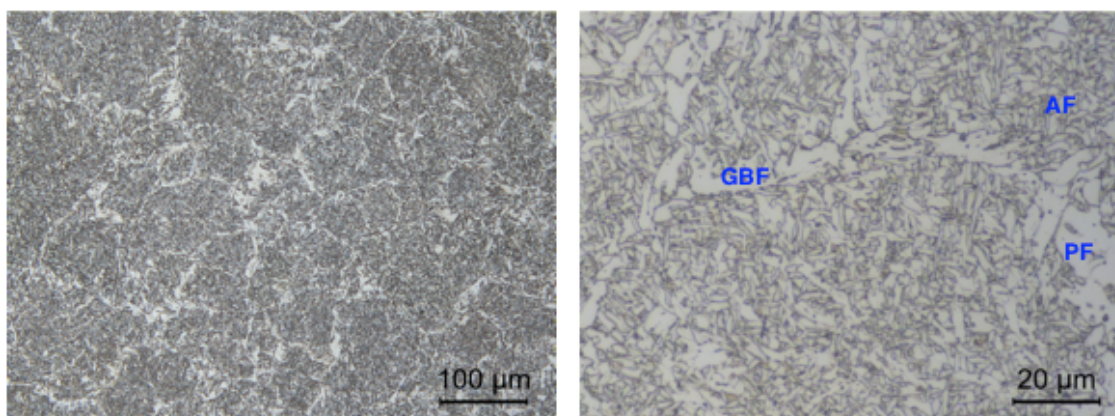


Figure 31. Coarse-grained weld metal of specimen 5.2.1.

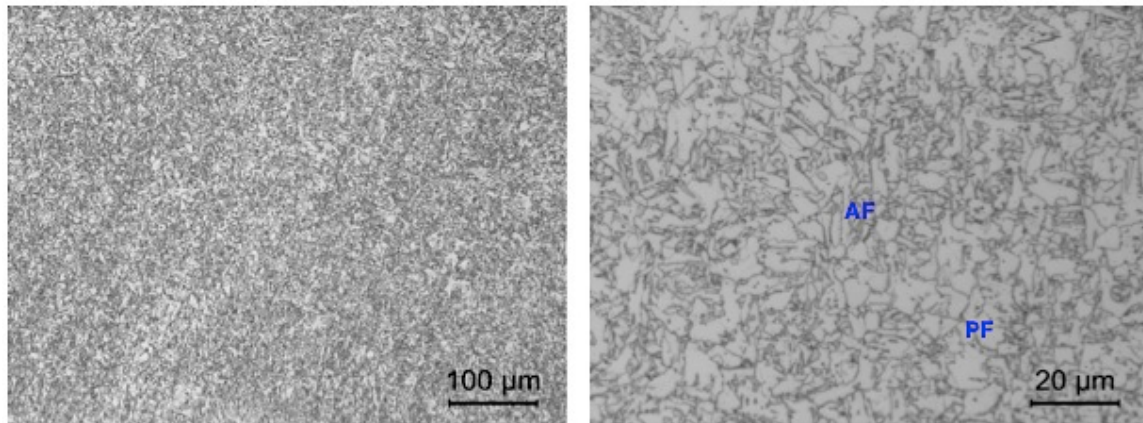


Figure 32. Fine-grained weld metal of specimen 5.2.1.

A quantification of the microstructure was carried out after the microstructural characterization and the results from the primary weld metal, the reheated coarse-grained weld metal and reheated fine-grained weld metal was compared. This is illustrated in Table 11 presented as the average number of the five measurements that was performed. The numbers are given in volume fraction and are equal to area fraction. The results were also compared to the images from the microstructural characterization.

Results from the quantification of specimen 2.1 show that the coarse-grained weld metal has a small increased amount of acicular ferrite, compared to the primary weld metal. The polygonal ferrite has increased some and the grain boundary ferrite has decreased. The reheated fine-grained weld metal has reduced amount of acicular ferrite and increased amount of polygonal ferrite compared to the two other regions.

Specimen 3.1 has increased amount of polygonal ferrite and decreased amount of acicular ferrite and upper bainite, when comparing the primary weld metal to the coarse-grained weld metal. The reheated fine-grained weld metal have further increased amount of polygonal ferrite and decreased amount of upper bainite, when compared to the two other regions. Specimen 5.2.1 has almost the same content of acicular ferrite in the primary weld metal and reheated coarse-grained weld metal, but the reheated fine-grained weld metal has a significant reduction. The amount of polygonal ferrite increases from primary to reheated coarse-grained and further to reheated fine-grained weld metal, while the grain-boundary ferrite decreases.

Table 11. Microstructural quantification of all three specimens.

Weld No.	Region	Volume fraction			
		Acicular ferrite	Upper bainite	Grain boundary ferrite	Polygonal ferrite
2.1	Primary WM	64	1	15	20
	Reheated CGWM	66	2	1	31
	Reheated FGWM	47	1	2	50
3.1	Primary WM	13	52	-	35
	Reheated CGWM	8	47	-	45
	Reheated FGWM	9	41	-	50
5.2.1	Primary WM	54	6	17	23
	Reheated CGWM	52	1	12	35
	Reheated FGWM	37	1	1	61

4.2 Microprobe analyses

All three specimens were analyzed in the microprobe, searching the elements inside the weld metal, with a special attention to the non-metallic inclusions. The result is presented as one backscatter image (BEI) and the chemical composition of the same area as presented in the image. Specimen 2.1 and 3.1 were analyzed during the specialization project but the results are also presented here. Figure 33 shows the BEI of specimen 2.1, while Figure 34 shows the chemical analysis. The inclusions in the image show high oxygen, titanium and manganese content. Only the large inclusion on the right contains silicon. The iron matrix has high nitrogen content and some magnesium and zirconium.

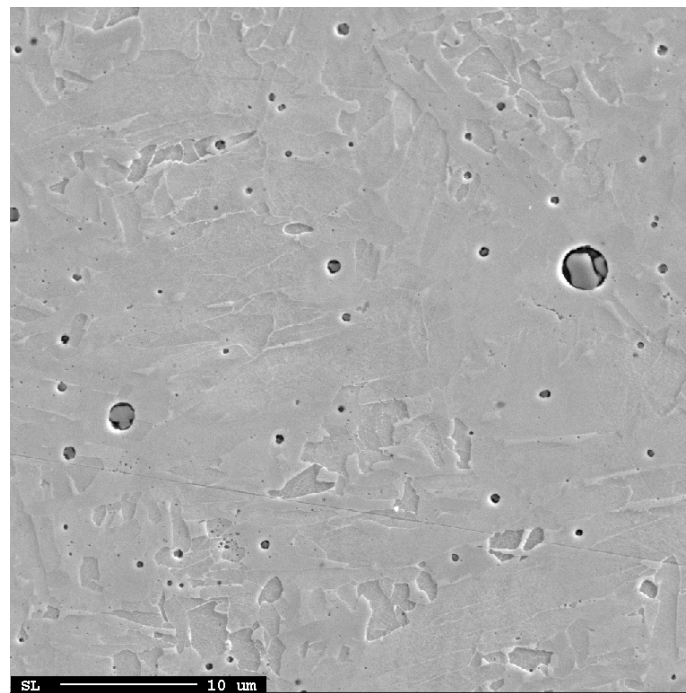


Figure 33. BEI of specimen 2.1.

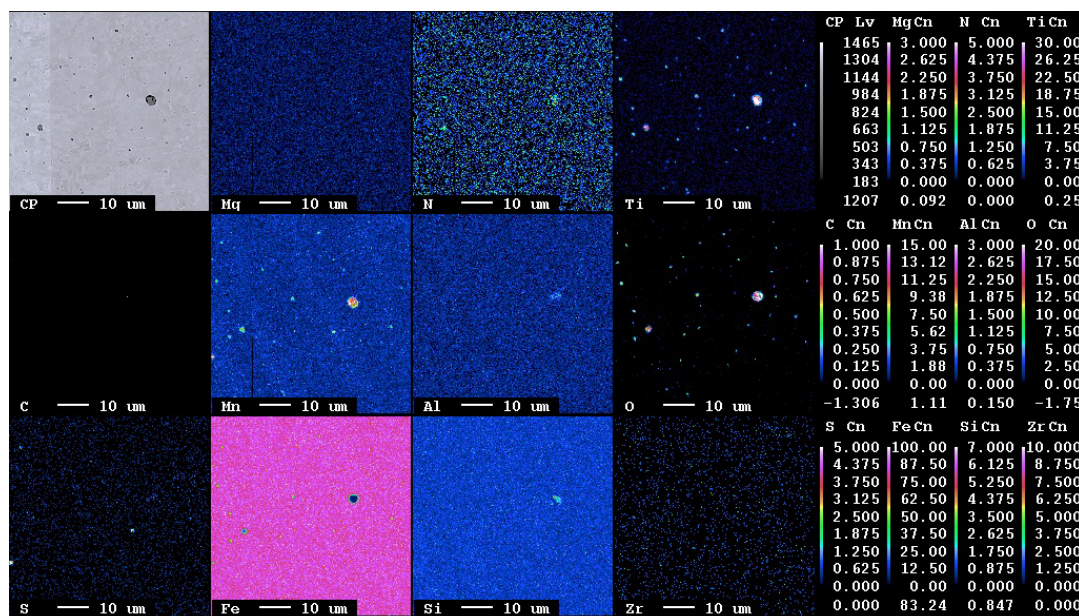


Figure 34. Specimen 2.1 analysed for chemical composition.

Figure 35 show the BEI of specimen 3.1 and Figure 36 present the chemical composition of the scanned area. The iron matrix consists of some nitrogen and magnesium. The inclusions show a large amount of aluminum, nitrogen and oxygen, in addition to some iron and zirconium. The large inclusions have higher nitrogen content than the smaller ones.

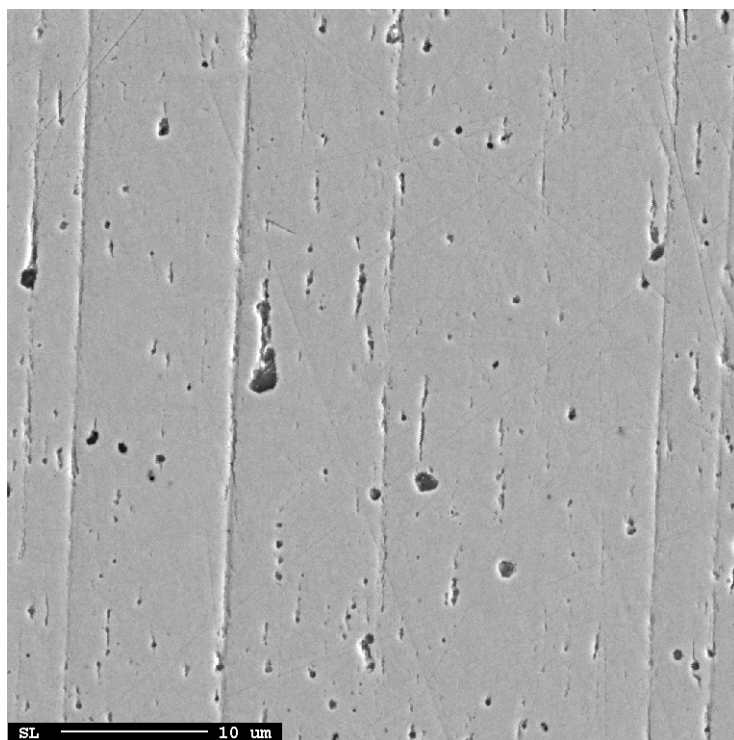


Figure 35. BEI of specimen 3.1.

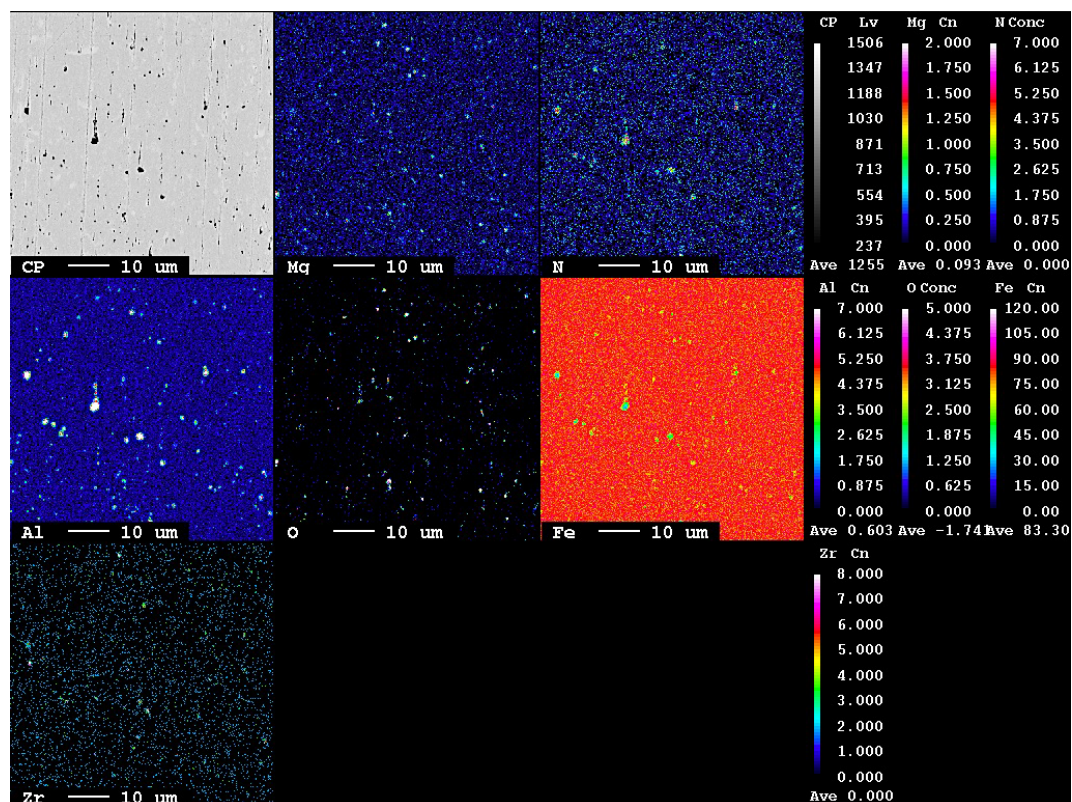


Figure 36. Chemical composition of inclusions in specimen 3.1.

Figure 37 shows the BEI of specimen 5.2.1 and Figure 38 shows that the inclusions are highly complex and consists of oxygen, aluminum, manganese, silicon and some sulfur. These elements may both create active and inert inclusions, depending on their composition.

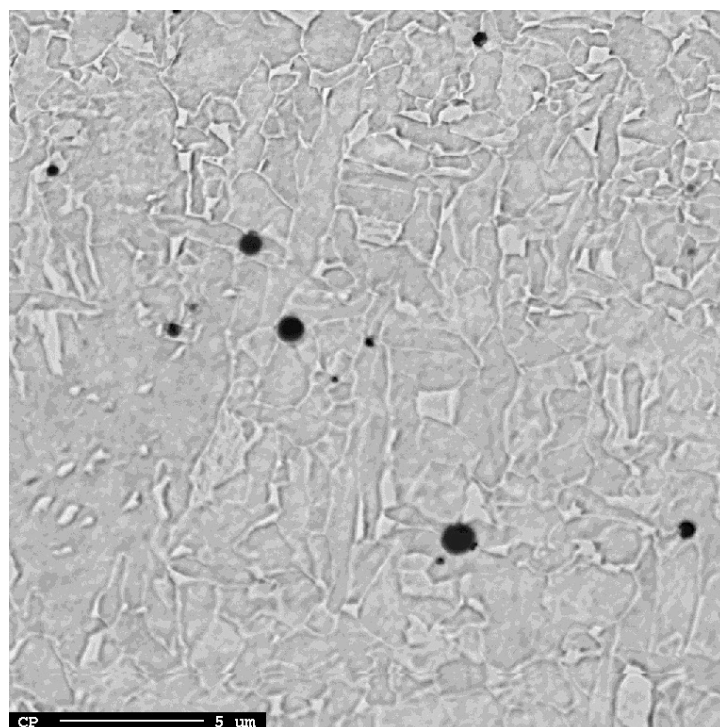


Figure 37. BEI of specimen 5.2.1.

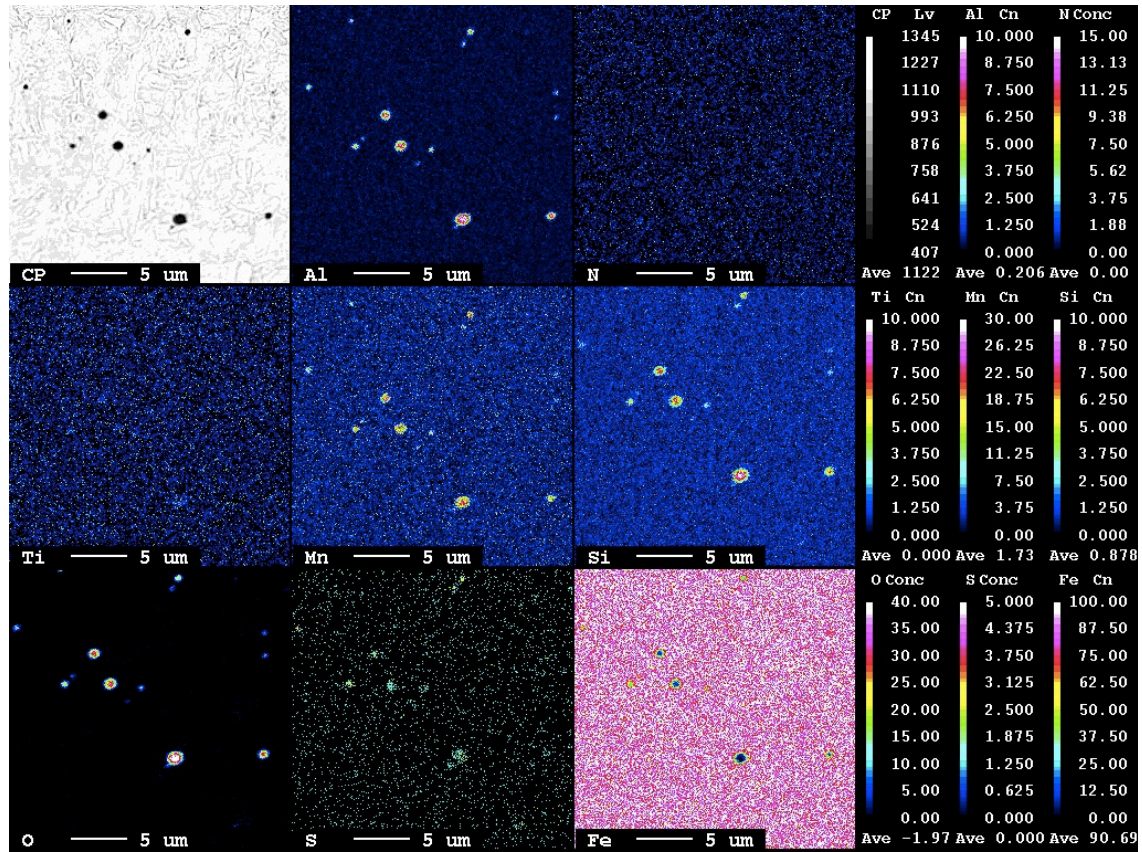


Figure 38. Specimen 5.2.1 analyzed for chemical composition.

4.3 Size distribution of non-metallic inclusions

One backscatter image (BEI) from each specimen was used to decide the size distribution of the non-metallic inclusions in the weld metal. The results from specimen 2.1 and 3.1 were presented in the specialization project but are also present here. The images used to decide the size distribution were the same as the BEI presented in chapter 4.2 for each specimen with a scale of 10 μm. The bar chart for all three specimens shows the inclusion diameter against the number of inclusions with this diameter. The inclusion diameter can be estimated from Equation (5) [4].

$$d = 0.35 \cdot (\eta E)^{\frac{1}{3}} \quad (5)$$

η is the arc efficiency and E (kJ/mm) is the gross heat input. By insertion of the values $\eta \sim 0.8$ for all welds, and E is 2.5 kJ/mm for weld 2.1 and 5.2.1 and 1.5 kJ/mm for 3.1, the average inclusion size is 0.44 μm for weld 2.1 and 5.2.1 and 0.37 μm for weld 3.1. Figure 39 shows a peak value in the size range of 0.2-0.3 μm for specimen 2.1. Figure 40 shows the results from specimen 3.1 and has consistently decreasing number of inclusion with increased inclusion diameter, with a peak value in the size range of 0.1-0.2 μm. Figure 41 presents the size distribution of specimen 5.2.1 with a distinct peak value of 0.4-0.6 μm.

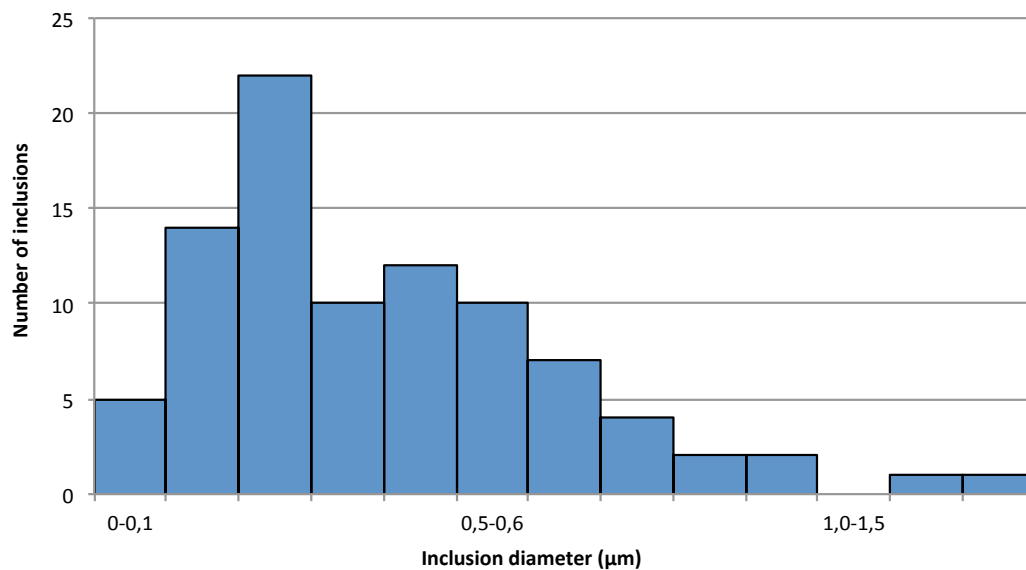


Figure 39. Size distribution of inclusions in specimen 2.1.

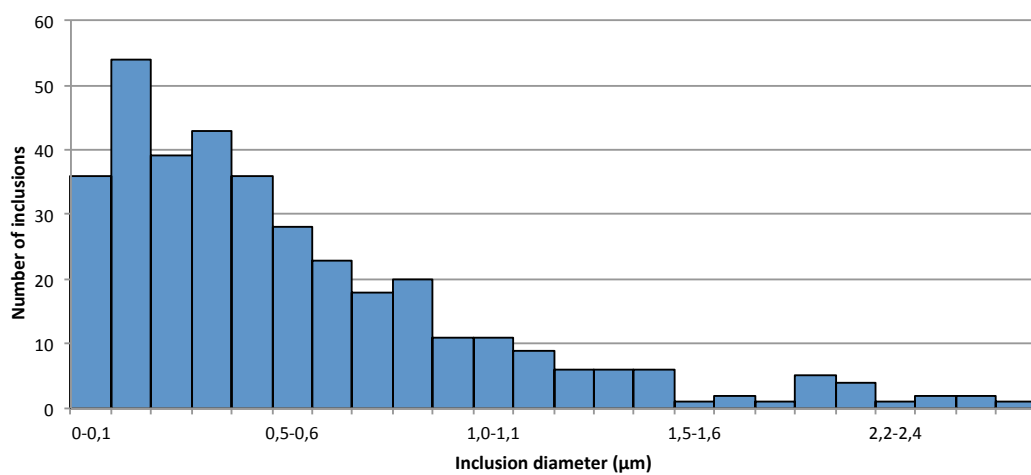


Figure 40. Size distribution of inclusions in specimen 3.1.

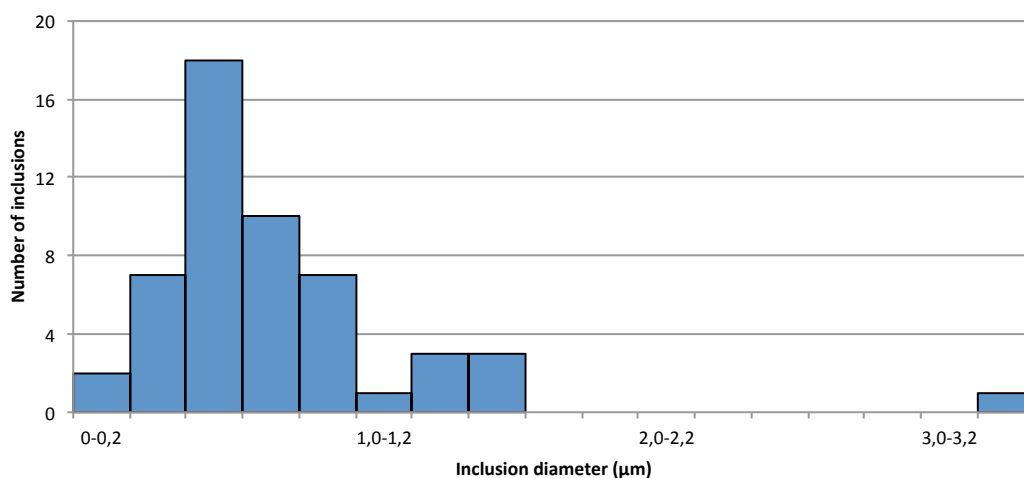


Figure 41. Size distribution of inclusions in specimen 5.2.1.

4.4 Fracture surface appearance

Prior to this thesis, Charpy impact tests were carried out at $-60\text{ }^{\circ}\text{C}$ so that the specimens would fail with as little ductile crack growth as possible. The absorbed energy during the impact for all three specimens is presented in Figure 42. As illustrated in Figure 42 weld 5 possesses the highest impact energy for toughness, while weld 3 has the lowest.

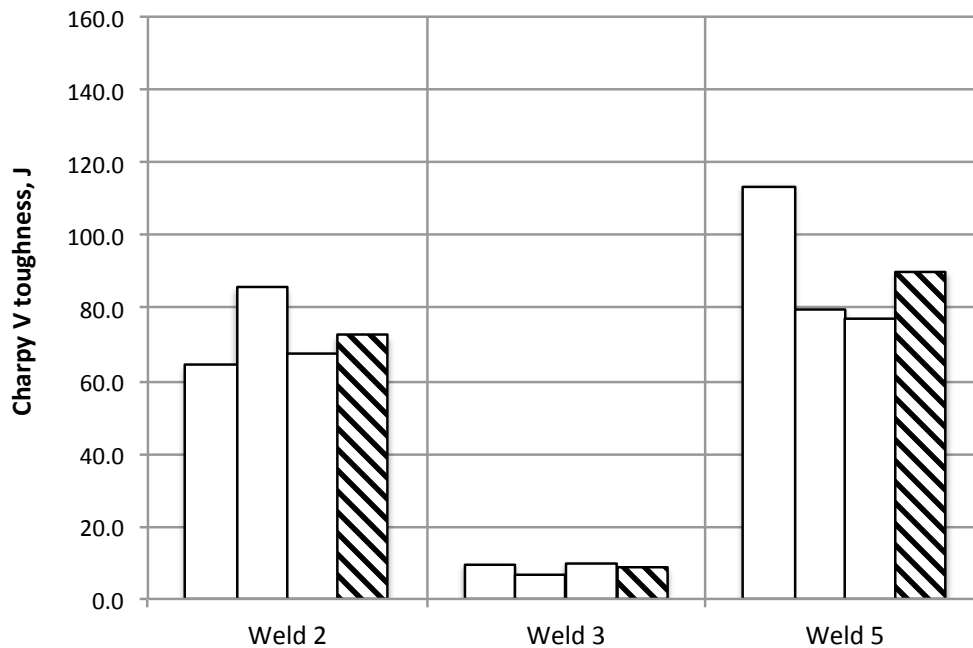


Figure 42. Charpy V notch test executed at $-60\text{ }^{\circ}\text{C}$ [25]. The striped column represents the mean value of the results.

Figure 43 presents the SEM macrographs from the Charpy V notch fracture surface. Visual inspection of the fractographs images of specimen 2.1 and 5.2.1 shows that a very large distortion has occurred during the fracture. While, for specimen 3.1, the fracture cross-section is almost perfect square. This indicates that the fracture occurred without almost any plastic deformation. In all of the images of the Charpy V notch specimens the notch is placed at the top.

Both specimen 2.1 and 5.2.1 possess a large area of ductile fracture before the brittle fracture. Figure 44 shows the borderline between the ductile and the brittle areas in specimen 2.1. Figure 44 reveals the ductile area as a dimpled surface, while the brittle area clearly shows Chevron patterns in various directions. Specimen 3.1 has a much smaller ductile area before the brittle fracture. This is expected due to the microstructure in this weld. Specimen 5.2.1 is quite similar to specimen 2.1, with a large ductile area before the brittle fracture.

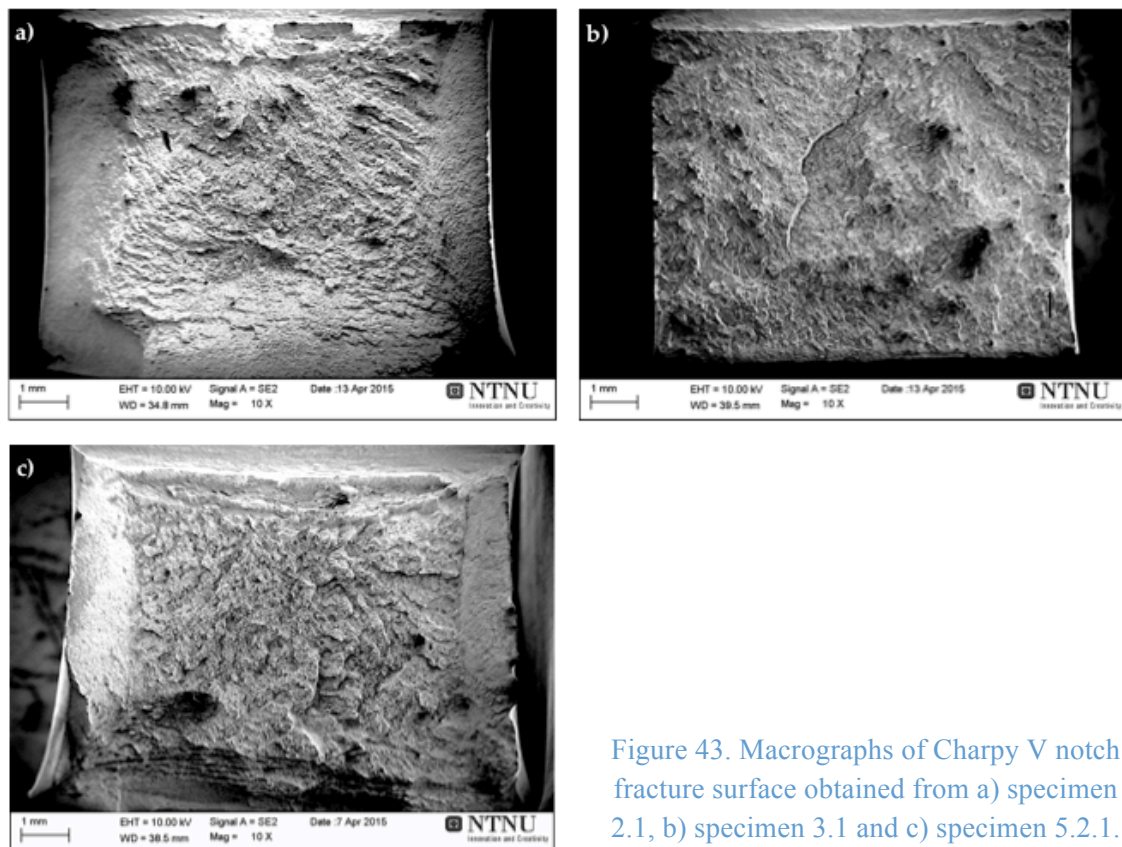


Figure 43. Macrographs of Charpy V notch fracture surface obtained from a) specimen 2.1, b) specimen 3.1 and c) specimen 5.2.1.

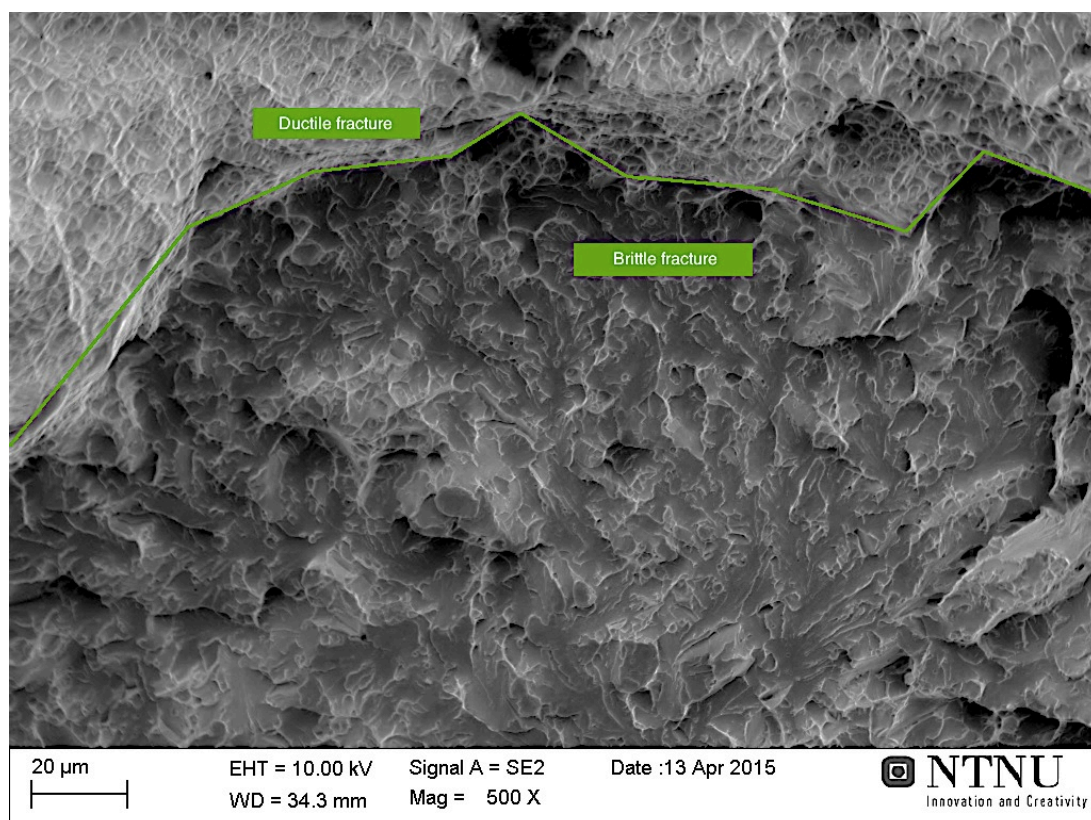


Figure 44. The borderlines between the ductile and brittle fracture in specimen 2.1.

Figure 45 shows an initiation point in the middle of the image (red square) in specimen 2.1. The initiation point is spreading away from the ductile area at the left and topside in the image.

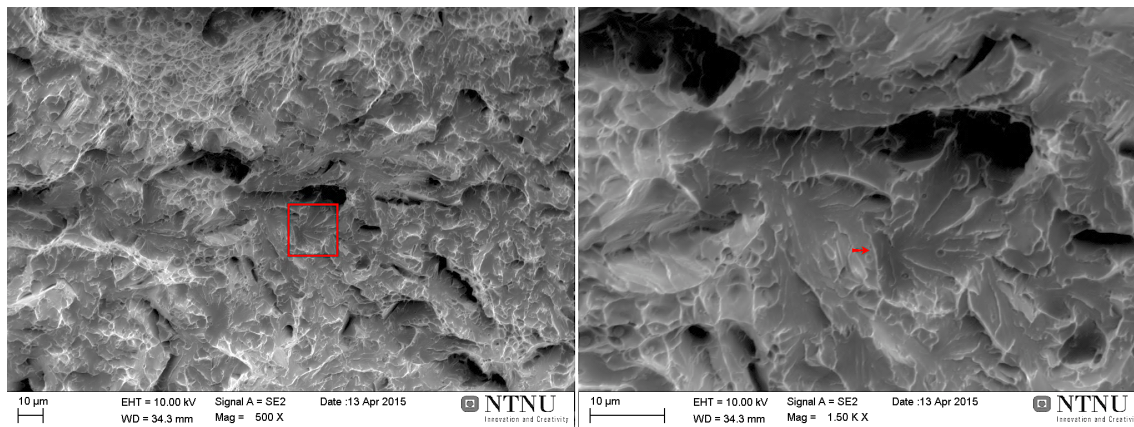


Figure 45. Initiation point in the brittle area of specimen 2.1 stretching from the ductile area at the left and topside.

Figure 46 shows an initiation point, marked with a red square, in specimen 3.1. The fracture is spreading in several directions and it especially stretches up to the narrow ductile area at the top where the notch is. There seems to be two points in correlation to each other that have started the cleavage.

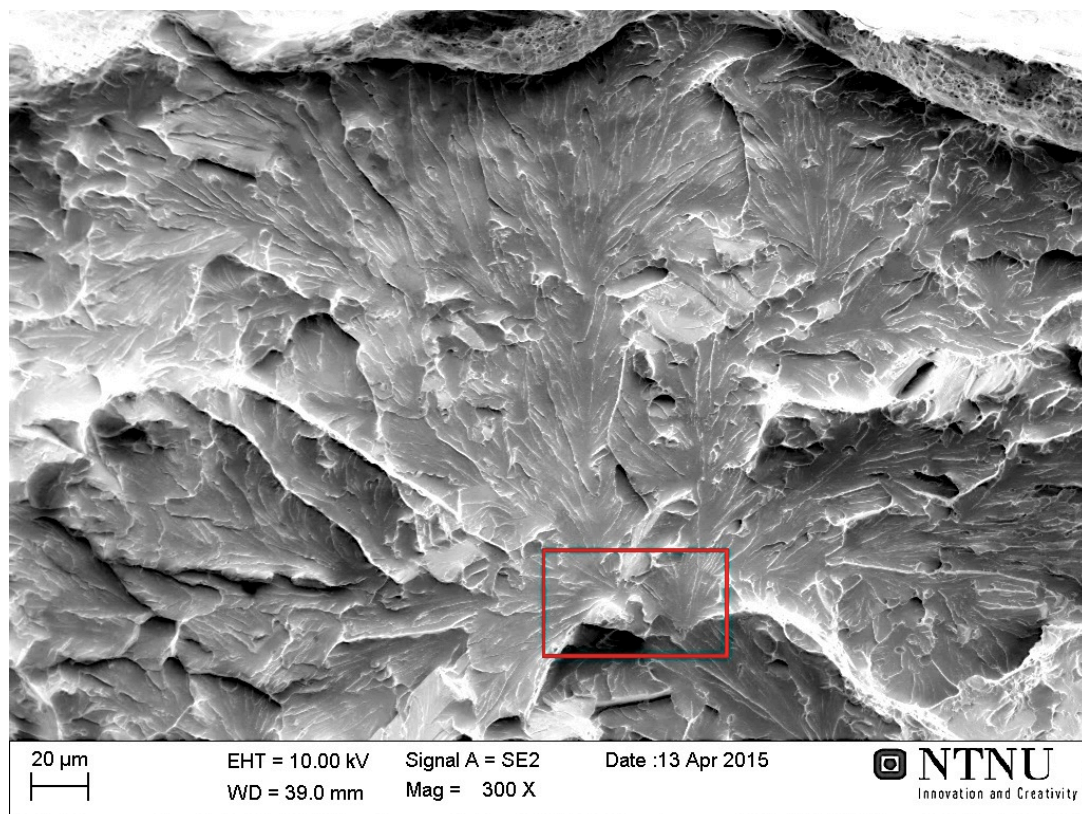


Figure 46. Initiation point of specimen 3.1 in brittle area. The fracture stretches towards the ductile area at the top where the notch is.

Figure 47 reveals an initiation point for a brittle fracture in specimen 3.1. This fracture spreads in every direction, also against the notch at the top of the image.

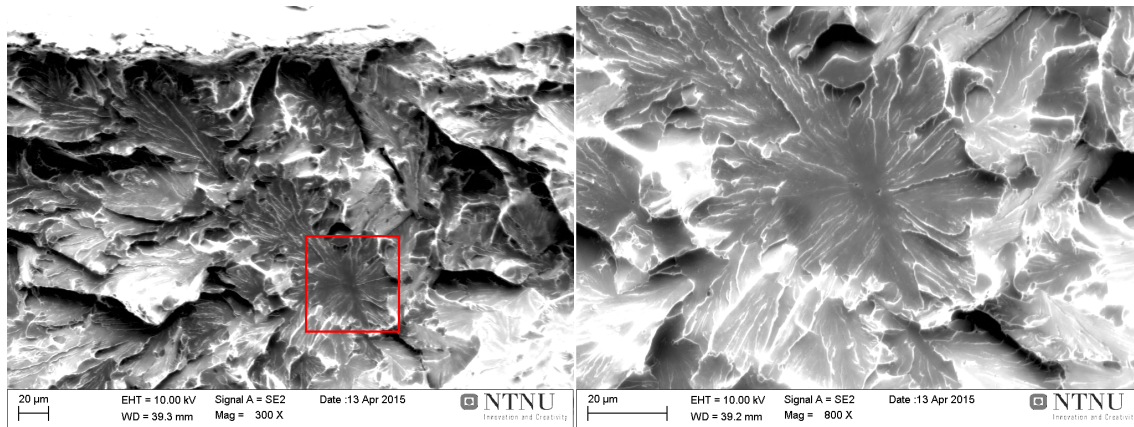
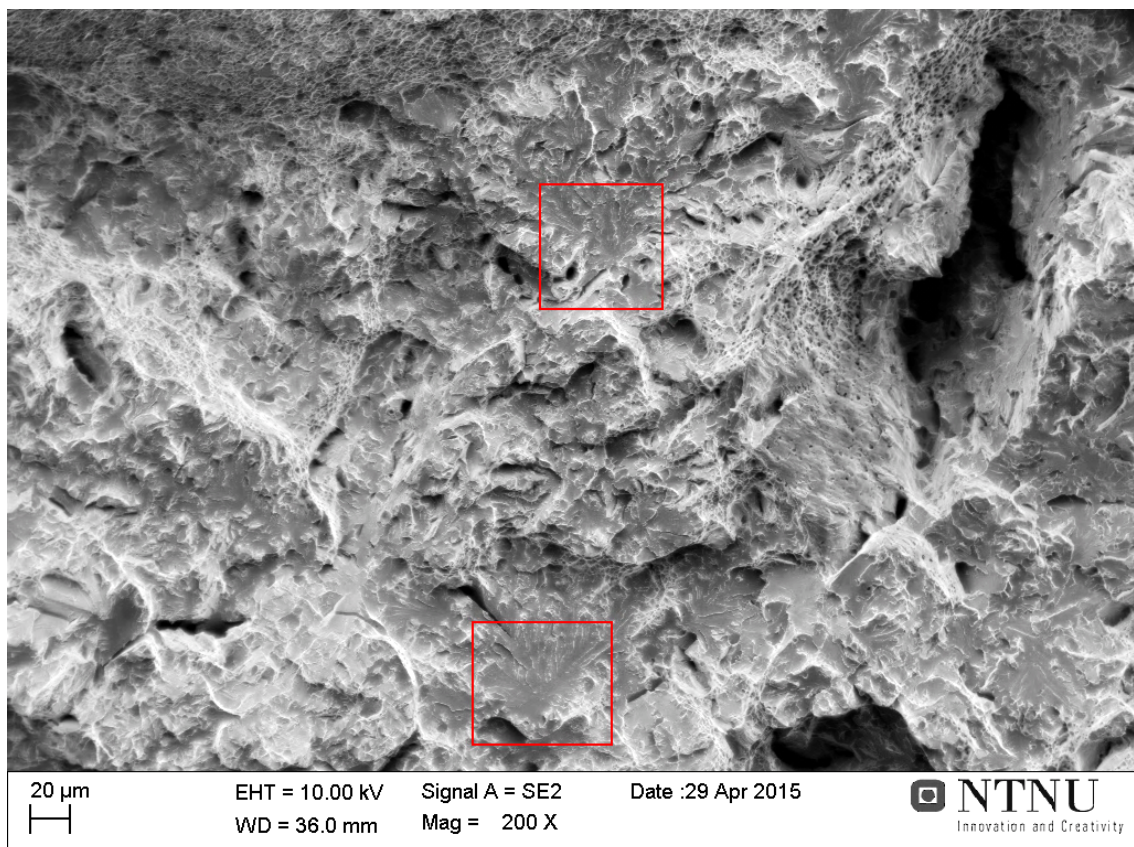
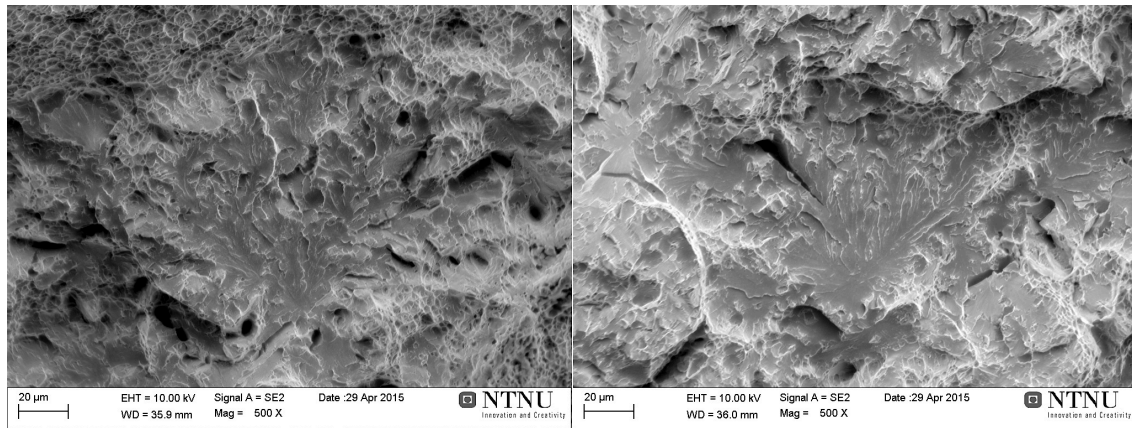


Figure 47. Brittle fracture in specimen 3.1. The initiation point is in the middle of the image and stretches in all directions.

Figure 48 shows two initiation points in the middle of specimen 5.2.1. Both are marked with a red square. The one on the top stretches towards the ductile area and the notch, while the other one is located further down in the weld. Both of them are spreading upwards.



a)



b)

Figure 48. Initiation point in the brittle fracture in the middle of specimen 5.2.1. a) Shows two initiation points; one stretching to the ductile fracture at the top and one further down in the specimen. b) shows a magnified image of both initiation points.

Figure 49 shows one example of an area in specimen 5.2.1 consisting of some ductile fracture surrounded by brittle fracture. There were several areas in this specimen similar to this.

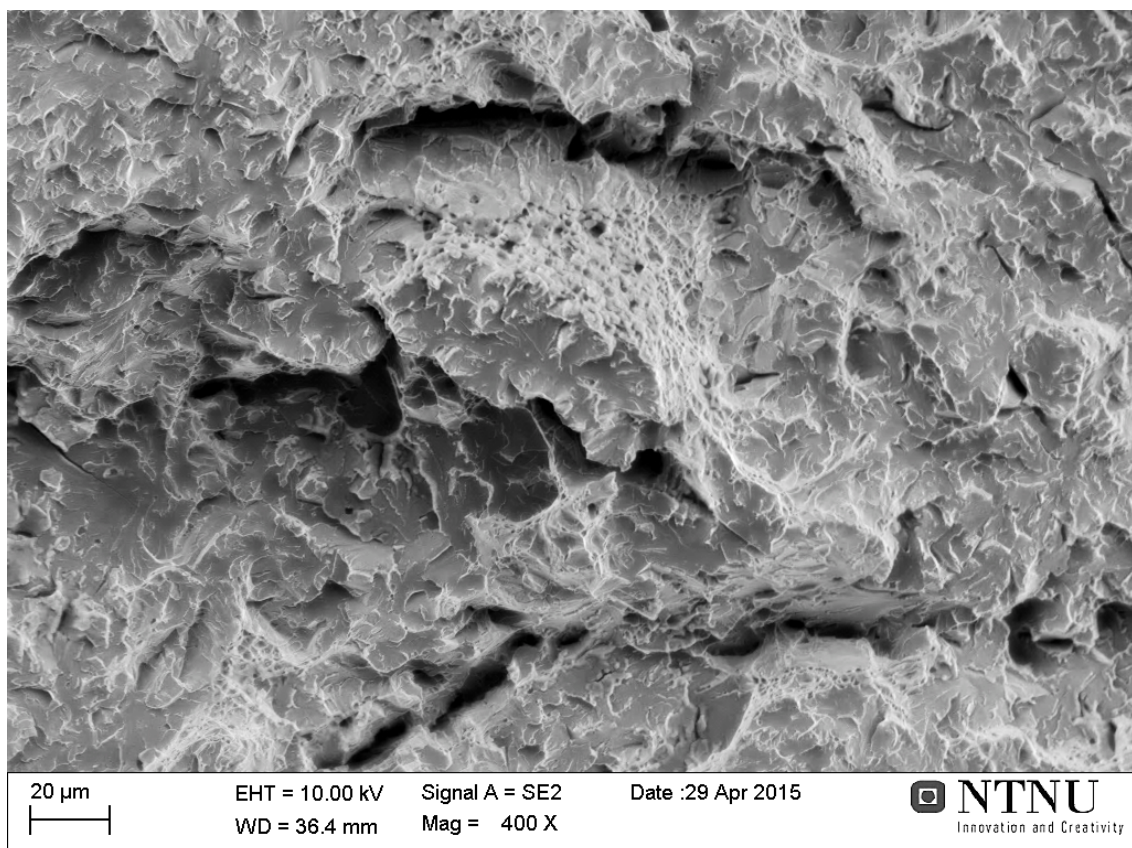


Figure 49. Mixture of brittle and ductile fracture in specimen 5.2.1.

4.5 TEM

4.5.1 Type and composition

Figure 50 shows the result from the chemical analysis of one inclusion and the surrounding matrix in specimen 2.1. The chemical analysis is presented with the Annular Dark Field (ADF) image first and the different elements detected in the following images. The ADF-image shows a core containing a titanium oxide phase, surrounded by a layer of oxygen, silicon, sulfur and manganese. On the right side there is an increased amount of manganese and sulfur, indicating a manganese sulphide phase.

By extracting a line-scan across the inclusion it was possible to further present the increased amount of manganese and sulfur. This is presented in Figure 51. This scan was done additionally to show if any manganese depletion has occurred around the surface of the inclusion, especially around the area of the manganese sulphide phase on the right side of the inclusion.

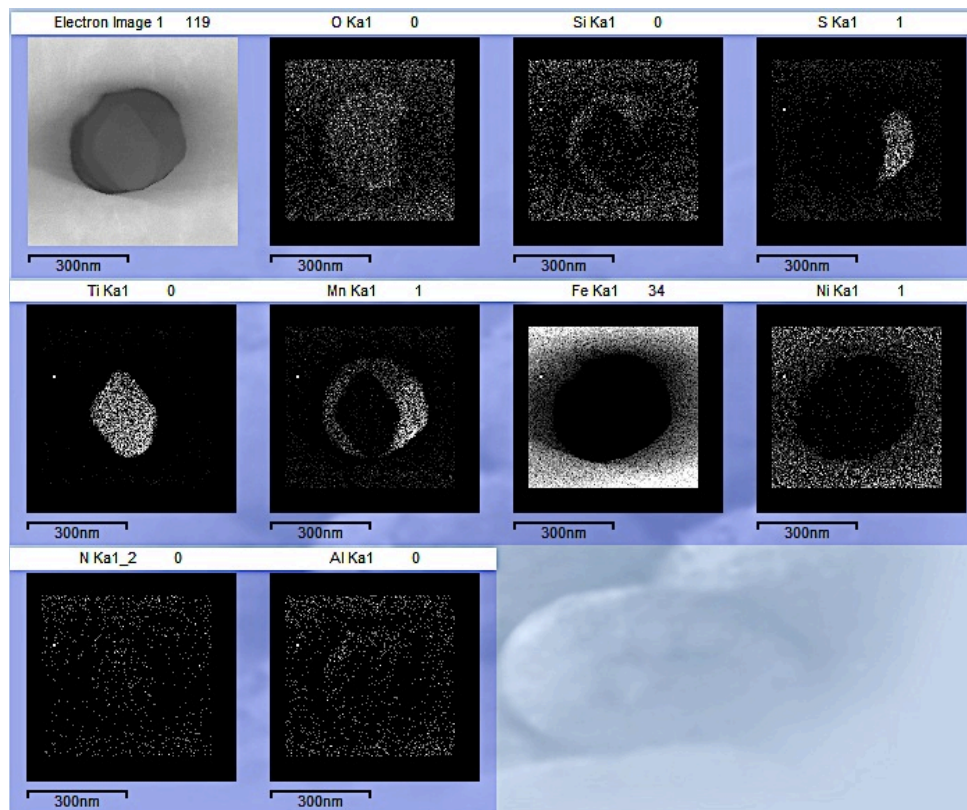


Figure 50. Chemical analysis of inclusion in specimen 2.1.

Figure 51 shows that the manganese content is consistent outside the inclusion, with only minor variations, but this may be noise caused by the weak signal. The content gets a significant increase in the area of manganese sulphide. Figure 52 gives shows that there is an increased amount of manganese and sulfur occurring in the same spot.

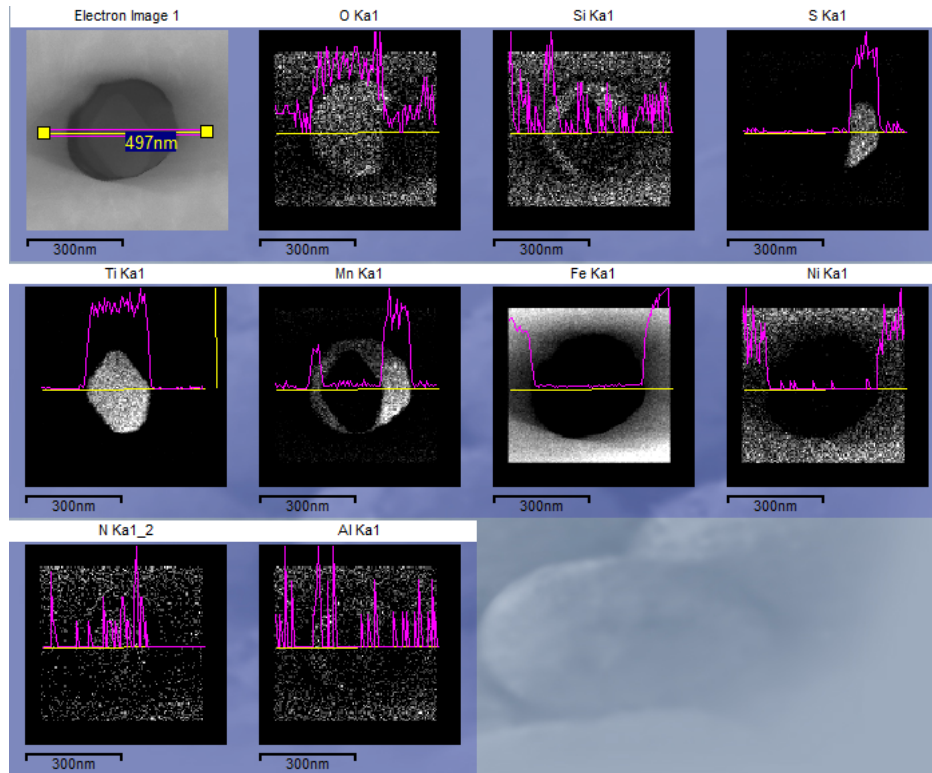


Figure 51. Line-scan executed on specimen 2.1.

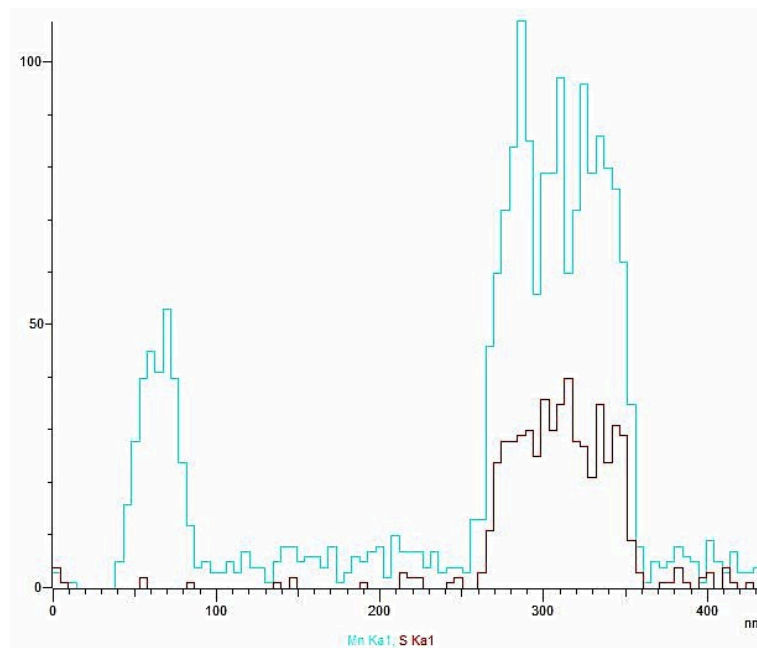


Figure 52. Illustration on the manganese (turquoise) and sulfur (red) content in the inclusion from Figure 50.

Figure 53 shows the result from the chemical analysis of two inclusions in specimen 2.1. Also these two inclusions have a large area containing oxygen and titanium, in addition to small amounts of nitrogen. Both inclusions have a small area on the edge consisting of manganese and sulfur. There is silicon as a thin layer on the surface of both inclusions and may be a silicon oxide phase.

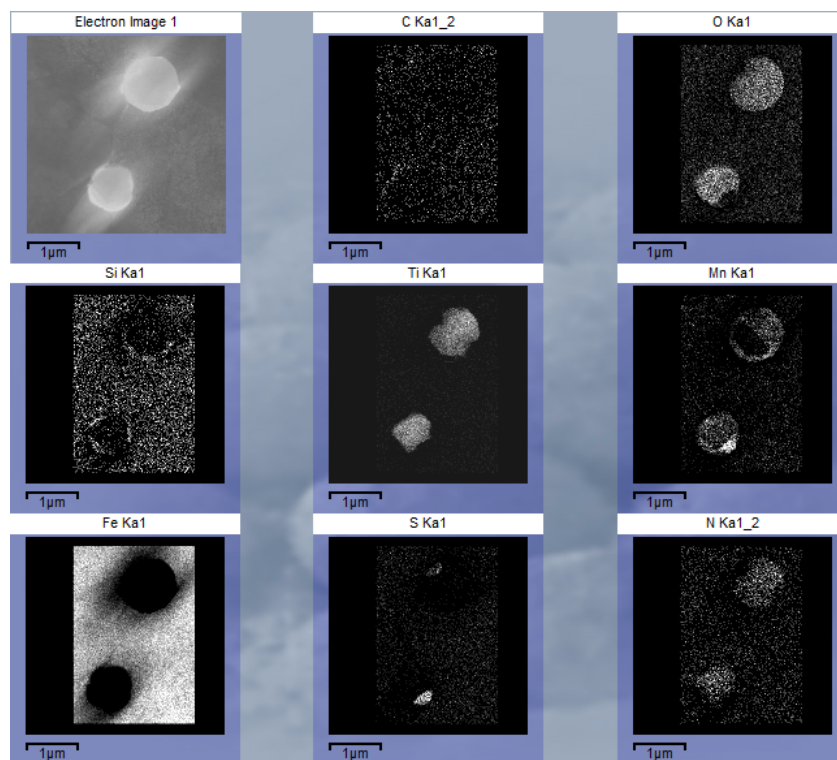


Figure 53. Chemical analysis of two inclusions in specimen 2.1.

Figure 54 shows the line-scan of two inclusions in specimen 2.1. The graph in Figure 55 is extracted from Figure 54 and show the manganese (red) and sulfur (blue) coexist inside both inclusions.

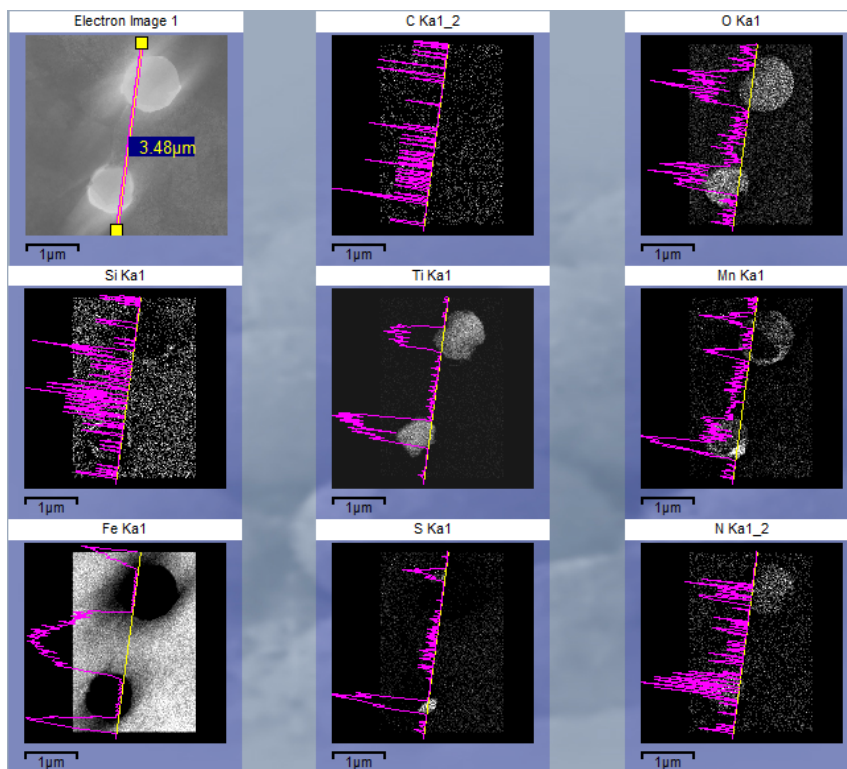


Figure 54. Line-scan of two inclusions in specimen 2.1.

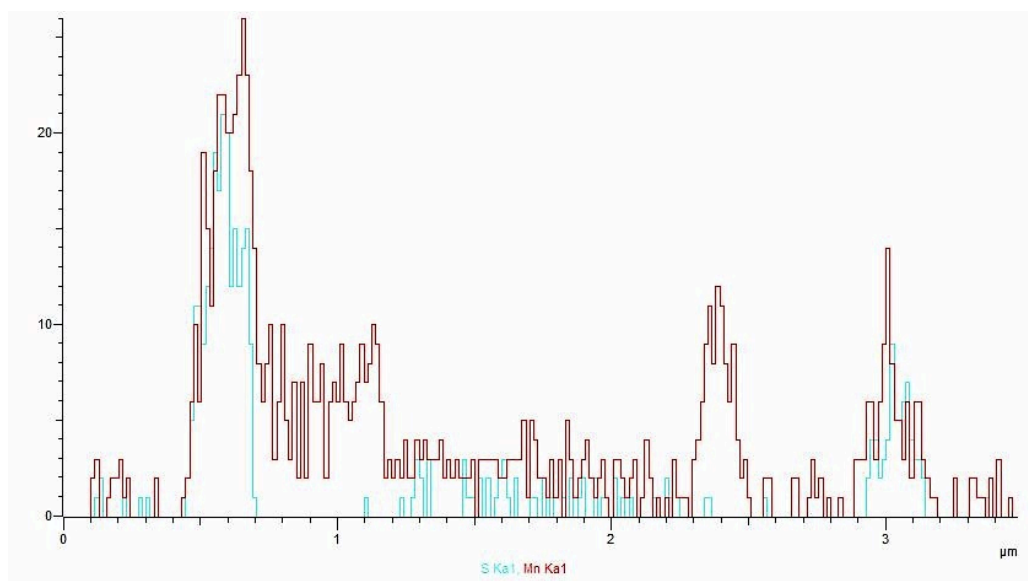


Figure 55. Illustration of manganese (red) and sulfur (turquoise) occurring in the same area.

Figure 56 shows one inclusion analyzed in specimen 3.1 containing a complex composition of nickel, oxygen, magnesium and aluminum. In addition there are some small areas scattered around the inclusion containing sulfur and zirconium.

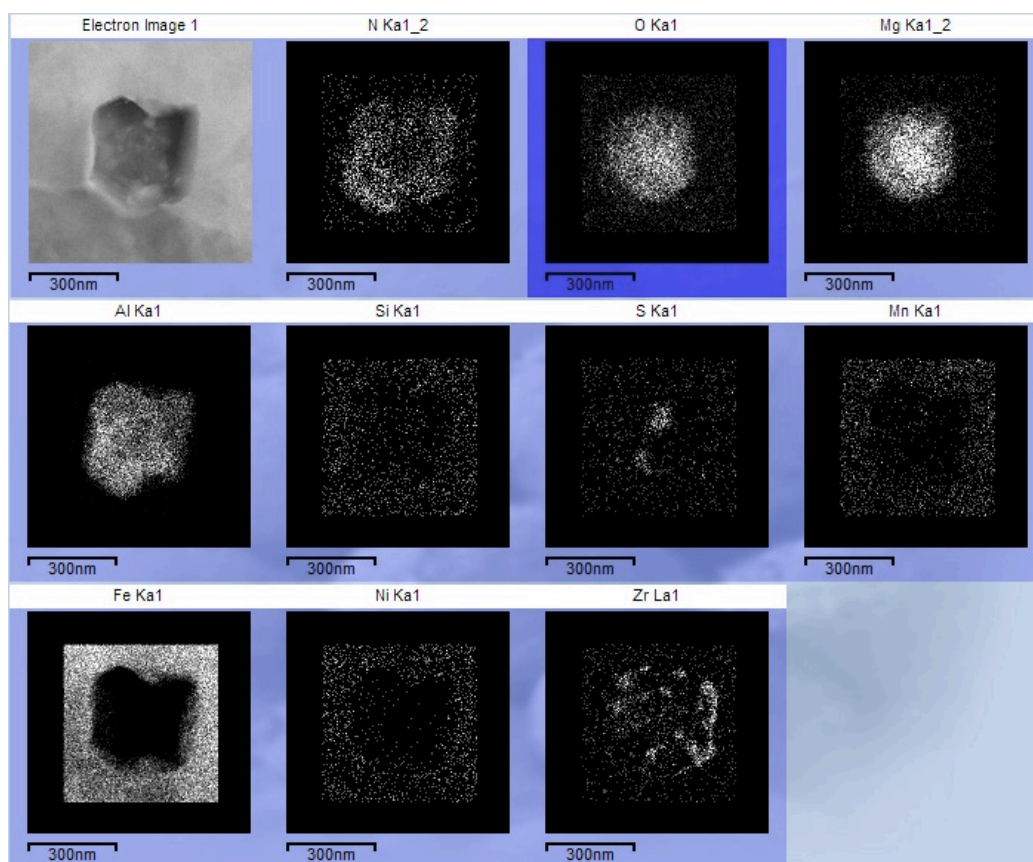


Figure 56. Chemical composition of inclusion in specimen 3.1.

Figure 57 shows the second inclusion analyzed in specimen 3.1. This inclusion is even more complex with several areas inside the inclusion consisting of different compounds. This inclusion has a core consisting of nickel, oxygen, magnesium, aluminum and some silicon and argon. Almost all of these elements are also in the surrounding layer but with somewhat different concentration. Zirconium is present as small areas scattered around the inclusion.

Line-scans were also extracted from the maps from inclusions in specimen 3.1 and the result from one of the inclusions is presented in Figure 58. The scan clearly shows that the elements magnesium, oxygen and aluminum increase in the same area and has a complex compound, this is presented in Figure 59.

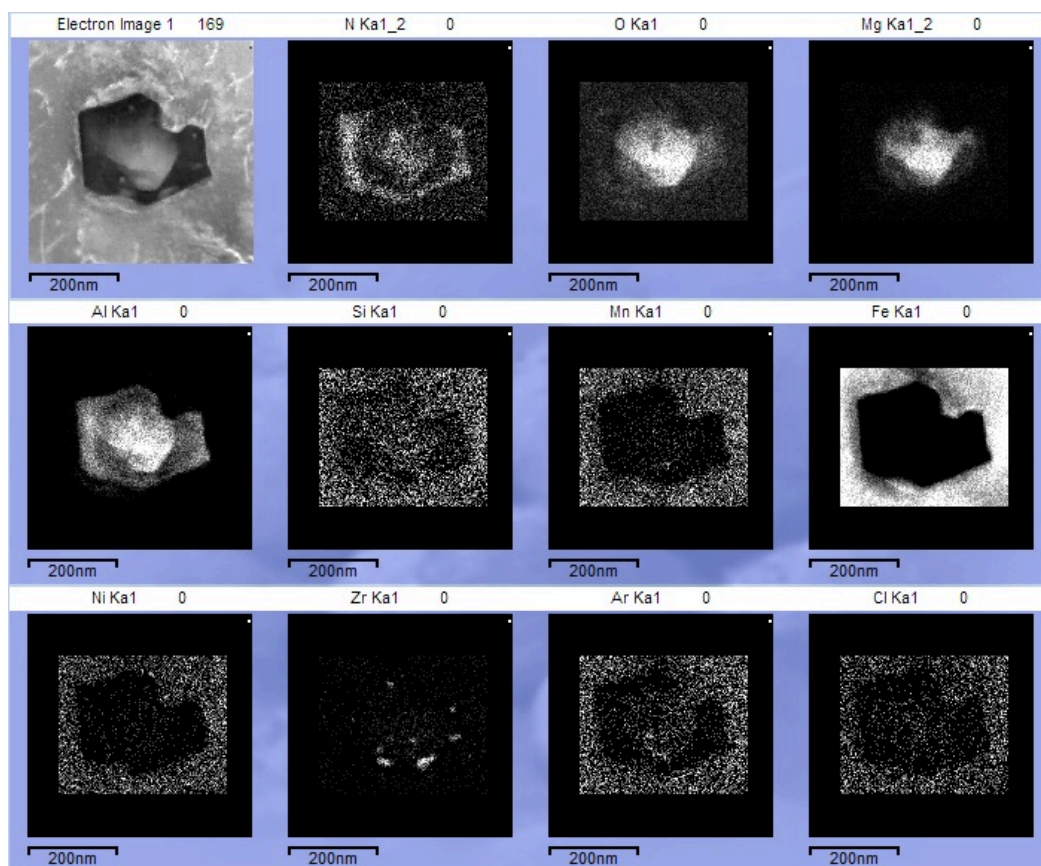


Figure 57. Chemical analysis of a second inclusion in specimen 3.1.

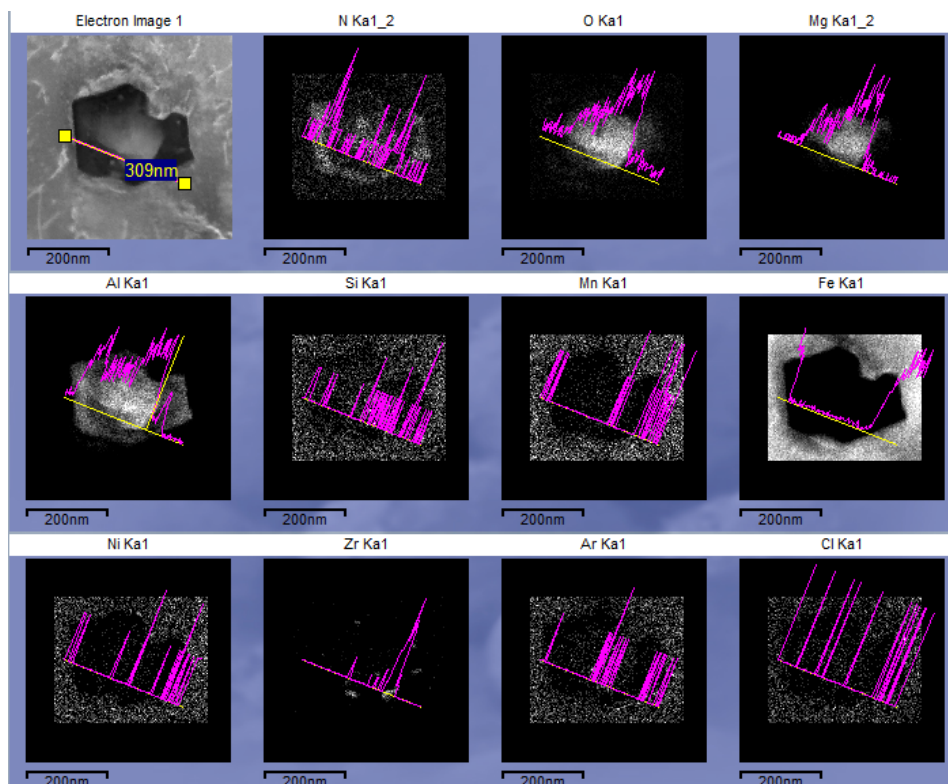


Figure 58. Line-scan of second inclusion in speciemen 3.1.

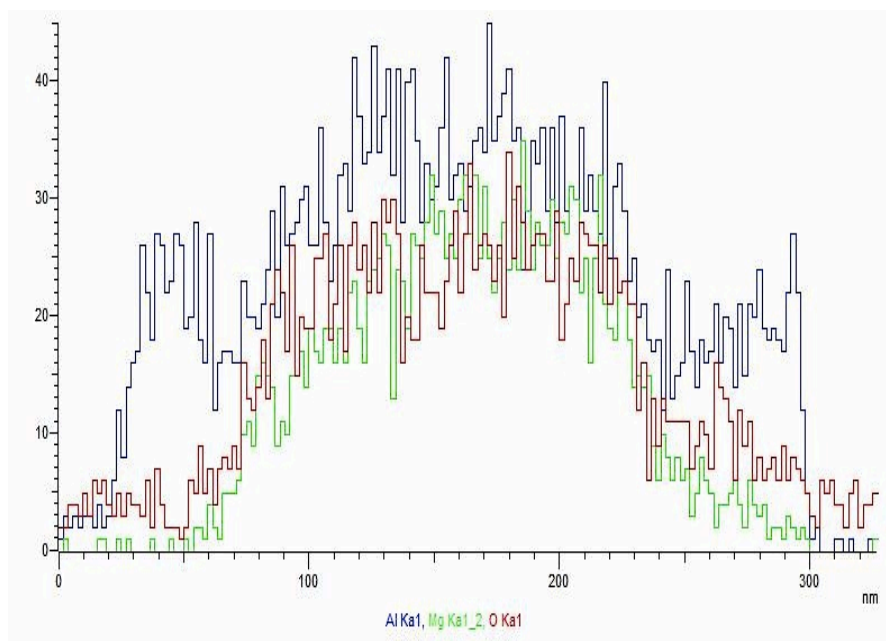


Figure 59. Results from line-scan of one inclusion in specimen 3.1. Aluminum (blue), magnesium (green) and oxygen (red) are increased in the same area.

Figure 60 show one inclusion from specimen 5.2.1 and it seem to have a uniform distribution of oxygen, aluminum, silicon and manganese. There is more titanium in the core and in one area at the surface where the sulfur content is increased. Line-scan for the same inclusion show that there is a compound consisting of manganese, silicon, aluminum and oxygen. This is presented in Figure 61.

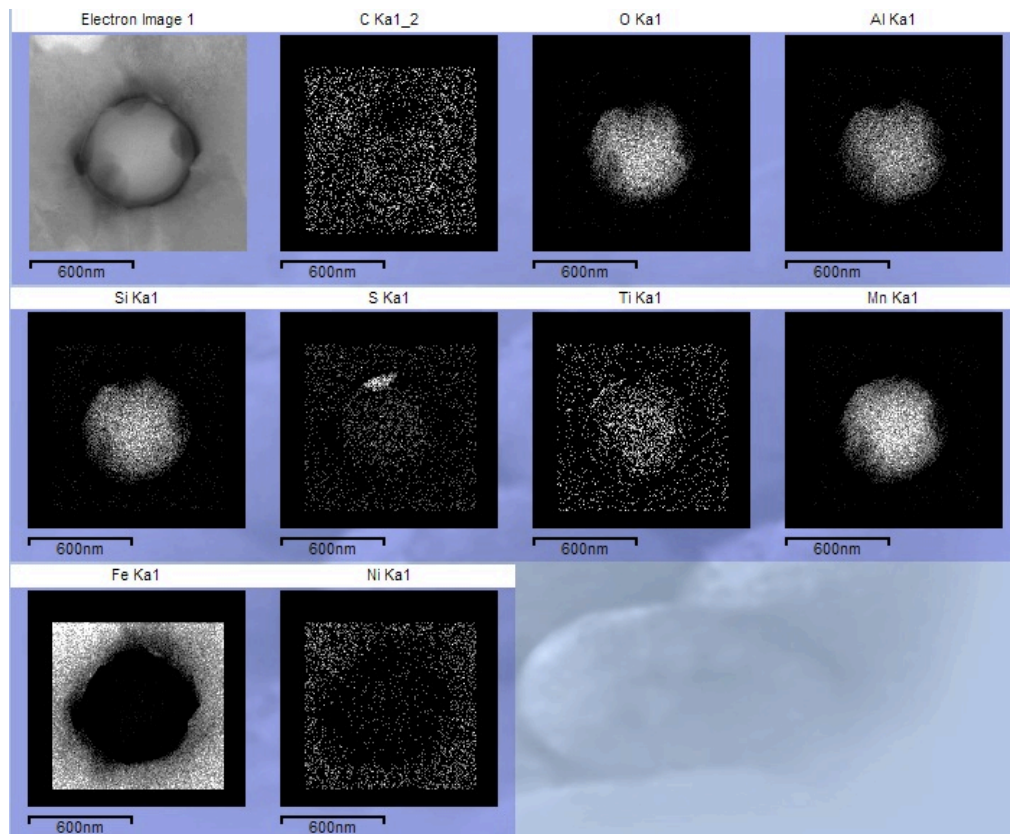


Figure 60. Chemical analysis of inclusion in specimen 5.2.1.

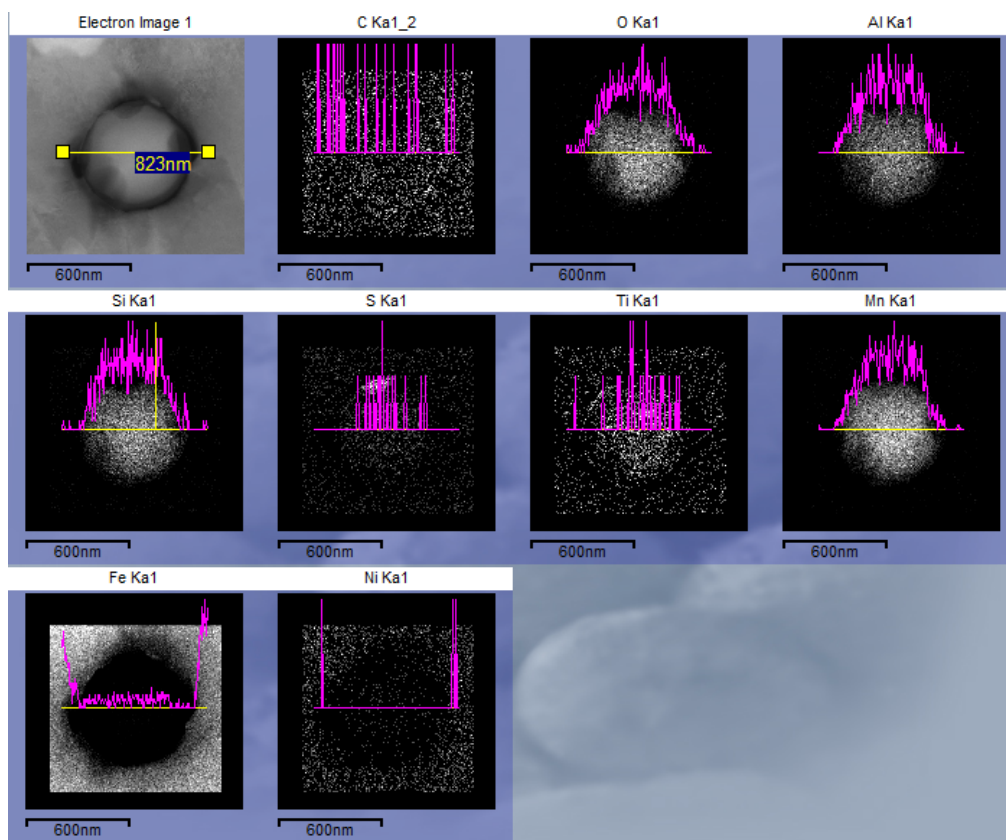


Figure 61. Line-scan of one inclusion in specimen 5.2.1.

Figure 62 shows how the elements manganese, silicon, aluminum and oxygen have an increased amount in the same area.

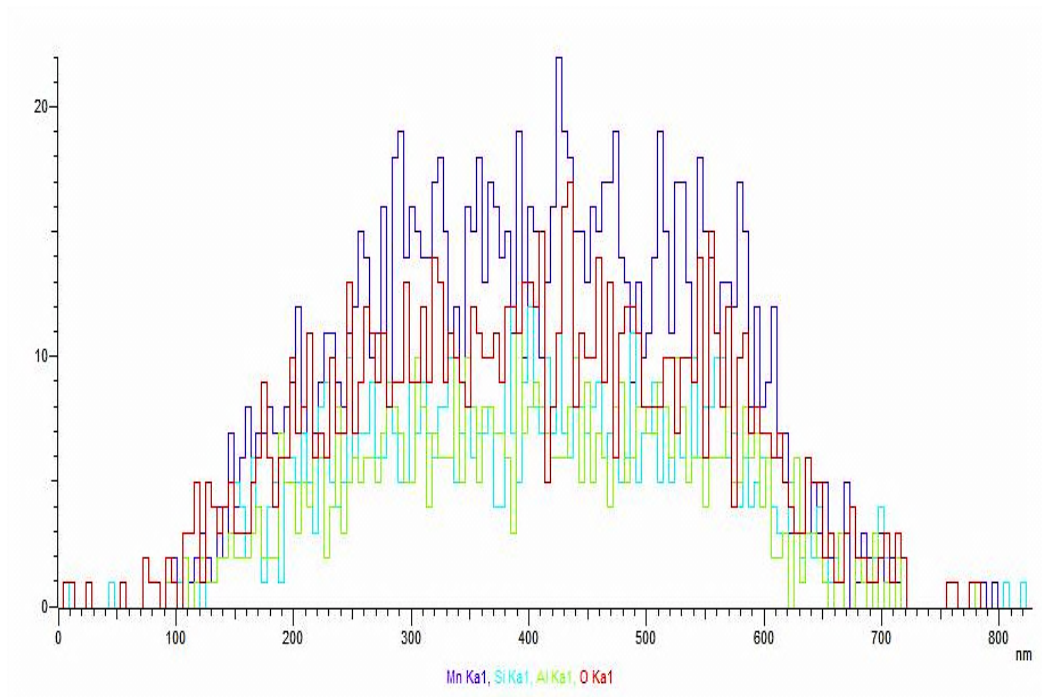


Figure 62. Result from line-scan of the inclusion in Figure 57, with manganese (purple), silicon (blue), aluminum (green) and oxygen (red).

4.5.2 Indexing of the inclusions

Due to time limitations there are only indexing results from one inclusion presented in this report. The inclusion that was indexed is the same one as in Figure 50-52. There were two interesting areas in this inclusion. One was the core, that contained a titanium oxide phase and the other was the manganese sulphide phase on the edge, both presented in Figure 22. Table 12 gives the calculations and the result from indexing the two areas.

Table 12. Results from indexing one inclusion in specimen 2.1.

Compound	y (pixel)	$d \text{ (Å)} = 1.92 \cdot \left(\frac{330.325}{y/r} \right)$
Titanium oxide	$y_1 = 473.7$	$d_1 = 2.678$
	$y_2 = 440.2$	$d_2 = 2.882$
	$y_3 = 532.0$	$d_3 = 2.384$
Manganese sulphide	$y_1 = 482.1$	$d_1 = 2.63$
	$y_2 = 689.3$	$d_2 = 1.84$
	$y_3 = 841.7$	$d_3 = 3.014$

The experimental d-values from Table 12 were then compared to the theoretical d-values for the compounds Ti_3O_5 and MnS . As Table 13 illustrates, the d-values corresponds well together. By calculating the zone axis using two of the directions for each compound presented in Table 14, a theoretical diffraction patterns could be constructed. Figure 63 and 64 gives the theoretical and the experimental diffraction patterns for Ti_3O_5 and MnS , respectively. The measured d values are located in the same direction as the theoretical ones.

Table 13. Comparison of experimental and theoretical d-values and the direction for Ti_3O_5 .

Compound	Experimental d-values	Theoretical d-values	Direction	Zone axis
Ti_3O_5	2.678	2.66	310	$13\bar{1}$
	2.882	2.93	$11\bar{2}$	
	2.384	2.38	202	
MnS	2.63	2.66	002	$1\bar{1}0$
	1.84	1.85	220	
	3.014	3.02	111	

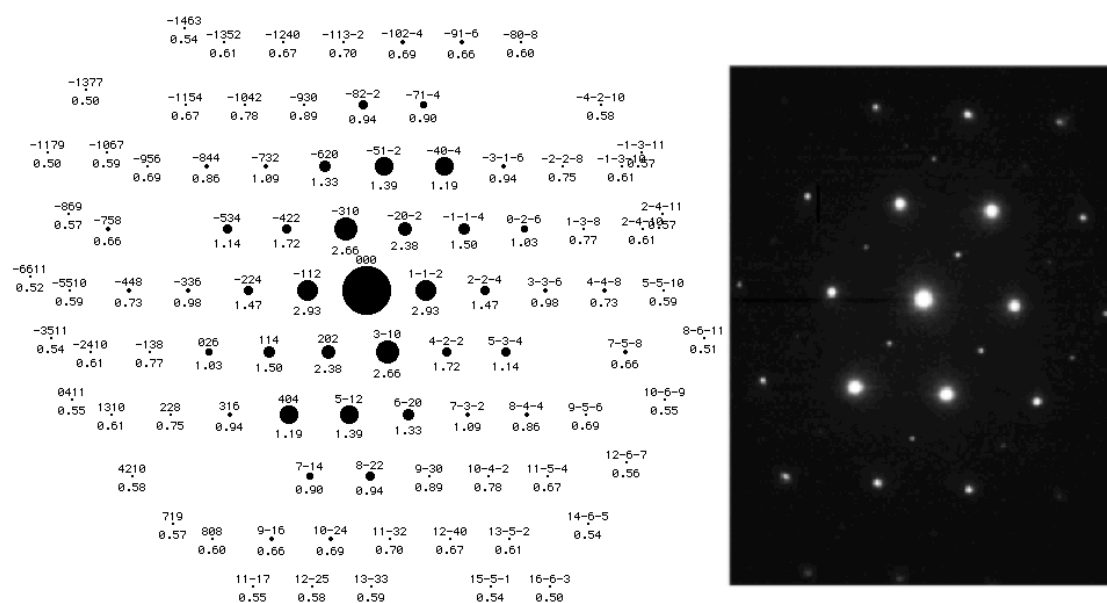


Figure 63. Theoretical diffraction pattern for Ti_3O_5 (left) with zone axis $[13\bar{1}]$ and the experimental diffraction pattern (right).

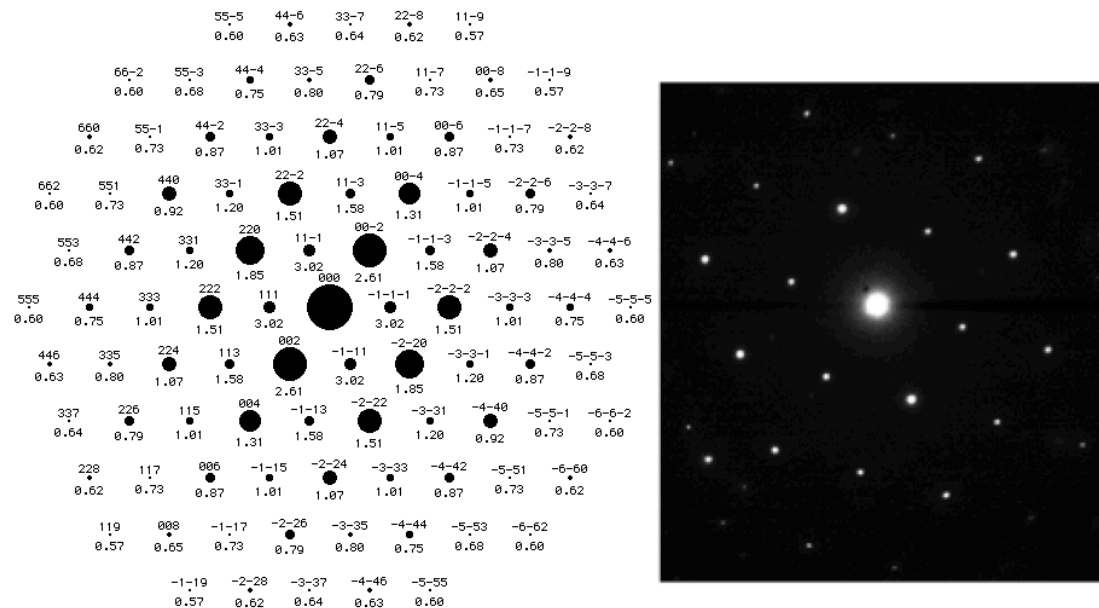


Figure 64. Theoretical diffraction pattern for MnS (left) with zone axis $[1\bar{1}0]$ and the experimental diffraction pattern (right).

4.5.3 Orientation relationship

If the inclusion had any effect on the nucleation of the surrounding iron matrix there should be an orientation relationship between them, otherwise the matrix is unaffected by the present inclusion. There was not a lot of time left to try and decide if an orientation relationship existed between the iron matrix and multiple inclusions in the three different weld metals. Although, looking at the diffraction pattern given in Figure 65 from specimen 2.1 in an area expected to consist of manganese sulphide, there seems to be some kind of orientation relationship occurring between the iron matrix and the manganese sulphide. It is possible to see that the diffraction pattern is similar to the manganese sulphide in Figure 64, but with some interference occurring in the outer edge of the pattern, the interference is marked with red arrows.

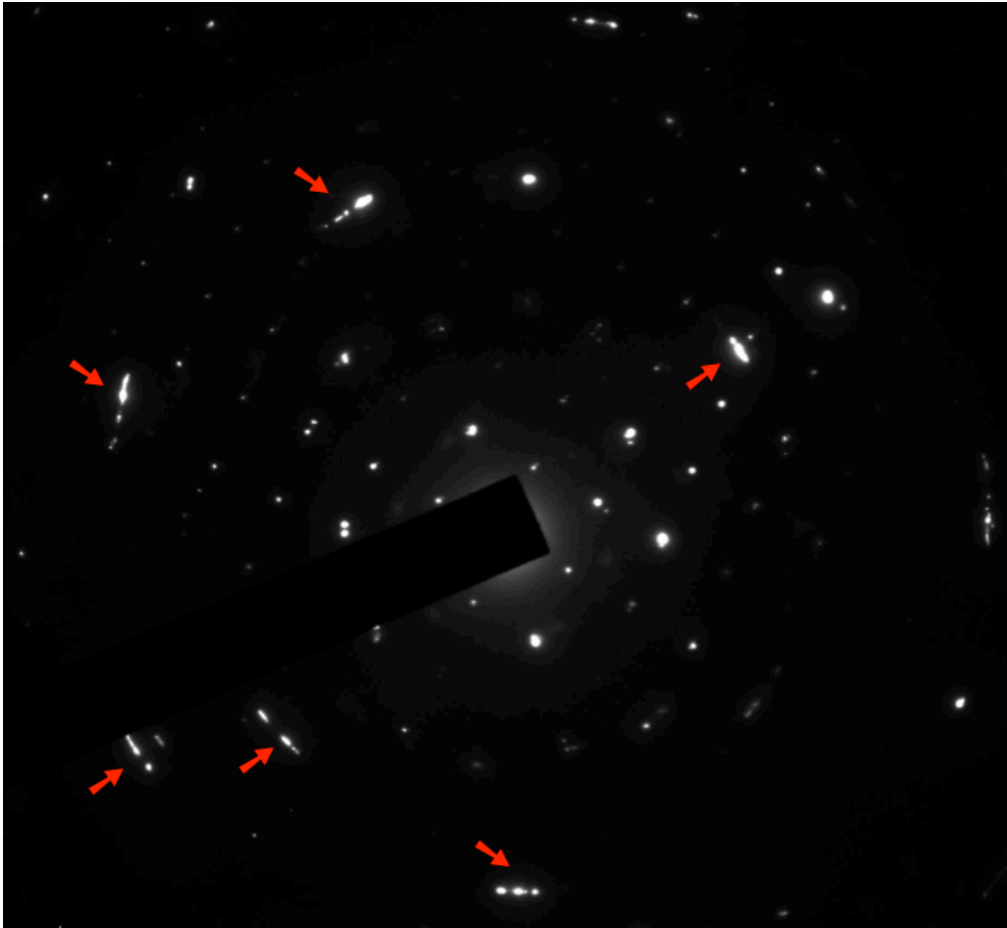


Figure 65. Diffraction pattern from specimen 2.1 illustrating possible orientation relationship between the iron matrix and the inclusion.

Chapter 5 Discussion

5.1 Microstructure

Specimen 2.1 consists mainly of acicular ferrite, with some reduction in the reheated areas with more polygonal ferrite. The acicular ferrite is fine-grained with grain size in the region of 1-3 μm , which result in high fracture toughness in low temperature environments. This makes it possible to conclude that the toughness test results in [25] are in good agreement with the microstructure. This weld has considerably higher titanium content than the two other welds (0.065 wt% against 0.003 wt% and 0.002 wt%), and this seems to have had a positive effect on the nucleation of acicular ferrite. In the theory chapter 2.5 a nickel content of 3 wt% is presented to be optimum to increase the amount of acicular ferrite [2]. With a content of 2.47 wt% in this weld, it seems that nickel may have contributed to nucleation of acicular ferrite. It is also worth mentioning that increased oxygen and sulfur content, according to the theory in chapter 2.2 and Equation (1), should produce higher volume fraction of inclusions. Specimen 2.1 have the highest content of both oxygen (530 ppm) and sulfur (0.006 wt%) of all three welds. It should therefore have the highest volume fraction of inclusions and have the best ability to produce acicular ferrite, assuming that the inclusions are active.

The microstructure in specimen 3.1 is very different from those found in specimen 2.1. The structure is mainly upper bainite without any grain boundary ferrite. The microstructure in the reheated areas is quite similar. The differences in these two welds may be caused by the lower heat input used in specimen 3.1 (1.5 kJ/mm), compared with specimen 2.1 (2.5 kJ/mm). Also, the absence of grain boundary allotriomorphic is not desirable for the nucleation of acicular ferrite. The theory says that small amounts of boron may contribute to acicular ferrite nucleation, but here the boron content is negligible. Specimen 3.1 was welded with a self-shielded wire, which makes it possible to weld in all positions, with no extra gas bottles and it is precise. Unfortunately, in this case, the weld metal did not possess an optimal composition or the right volume fraction of non-metallic inclusions to nucleate acicular ferrite. Also, the oxygen content for this weld (120 ppm) is significantly lower than specimen 2.1 (530 ppm), which may show that oxygen plays an important role in nucleation process of acicular ferrite.

Specimen 5.2.1 has a high volume fraction of acicular ferrite in the primary weld metal, despite the low titanium content (0.002 wt%). The structure is fine grained, which may be caused by the high Mn content (1.65 wt%) in the weld. This may push the transformation to lower temperatures, and promote refinement of the microstructure. Although, this fine microstructure in the primary weld have low toughness results in the CTOD test [26], which may have been caused by the low Ni content (0.80 wt%) increasing the transformation-temperature. There seem to be larger differences in the fine and coarse-grained reheated areas in this weld than for specimen 2.1, and more

bainite and elongated ferrite in the reheated zones. The oxygen content (320 ppm) is lower than specimen 2.1 (530 ppm), but much higher than specimen 3.1 (120 ppm), which again is an indication that oxygen plays an important role in nucleating acicular ferrite.

5.2 Micro probe and size distribution

Results from the analysis of specimen 2.1 show that the non-metallic inclusions consist of large amounts of titanium, oxygen, nitrogen and manganese. This is in good agreement with the theory stated in chapter 2.5. As illustrated in Table 1 the most effective inclusions for acicular ferrite nucleation is simple and complex titanium oxides and nitrides, which is found located in this weld metal. Some large inclusions are also found, which have the additional element silicon. This element is often found in inert inclusions and do not nucleate acicular ferrite. This may be why the microstructure does not have an even higher content of acicular ferrite.

The analysis of specimen 3.1 reveals small inclusions consisting of aluminum, oxygen, nitride and manganese. This confirms the theory (chapter 2.5) of inert inclusions made of simple and complex oxide, containing aluminum and manganese. The effect of nitride in these inclusions is unclear. But is clear that the aluminum nitride in this weld metal not is an active inclusion for nucleation of acicular ferrite. Titanium nitrides may act as both active and inert inclusions, but in this case, there is no titanium in the inclusions. The analysis also shows zirconium content in the weld metal. It is not clear how this ended up in the weld, but it may have originated from the flux in the welding wire.

The results from the quantification of specimen 5.2.1 showed that the weld consist of multiple structures, including acicular ferrite. This may be a result from the inclusions being both active and inert. The inclusions found in this weld are highly complex but have a low content of titanium. Since titanium is an important element to nucleate acicular ferrite, this low content may be one of the reasons that this weld consists of several microstructures. The nitrogen content is not elevated inside the inclusion, indicating that the inclusions contain different types of sulfides and oxides. Although the aluminum content in the weld metal is quite low, several of the inclusions have a high content of some kind of aluminum oxide. They may act as active or inert inclusions depending on the composition.

Specimen 2.1 seems to have a large number of inclusions in the region of 0.1-0.7 μm . When comparing this with the theory on which sizes being most active in nucleating acicular ferrite, there are some similarities, even though the theory in chapter 2.5 claims that inclusions in the size range of 0.5-0.8 μm is most effective in nucleating acicular ferrite. The theory also says that increased titanium content decreases the size of the inclusions, which may have been the case for specimen 2.1.

Specimen 3.1 shows that the majority of the inclusions are much smaller than for specimen 2.1. Both the welding parameters and the chemical composition of this specimen is quite different from specimen 2.1 and makes it difficult to decide what may have caused this marked reduction. Both the aluminum and nitrogen content is increased for this weld.

Specimen 5.2.1 seem to have a large number of inclusions in the region of 0.4-0.8 μm . When comparing this with the theory in chapter 2.5 on which sizes being most active in nucleating acicular ferrite, it corresponds very well. In chapter 2.5 former research states that optimal Ti content is around 0.07 wt %, resulting in more and smaller inclusions, this weld have a much lower Ti content (0.002 wt %). This may be the reason that the inclusions are larger in this weld than in weld 2.1. Except the heat input (2.5 kJ/mm), the welding parameters are very different from specimen 2.1. The travel speed especially, which is very fast for specimen 5.2.1 (7.3 mm/s) compared to the two other welds (2-3 mm/s and 4.1 mm/s).

In the theory in chapter 2.4 it is stated that heat input is one of the factors controlling the size of the inclusions, and the results here indicate that higher heat input (specimen 2.1 and 5.2.1 have 2.5 kJ/mm) gives larger inclusions than lower heat input (specimen 3.1 with 1.5 kJ/mm), which corresponds well with the theory in chapter 2.4.

It should be mentioned that there are large uncertainties concerning the results in size distribution. The results are based on only one location from one image of the specimens.

5.3 Fracture surface

When comparing all three specimens in the first overview image (Figure 43), it is clear that specimen 2.1 and 5.2.1 has been subjected to an extensive amount of plastic deformation before fracture. Specimen 3.1 shows that little or no plastic deformation has happened before the fracture and therefore has kept the original square shape.

Specimen 2.1 has a large ductile area beneath the notch, indicating good ductility and toughness in the weld metal. The fracture appearance in the brittle area reveals small facets, which are poorly defined. Small Chevron patterns are seen, but they do not stretch as long as in specimen 3.1. There were not detected any clear indications on what started the fracture.

The fracture appearance of specimen 3.1 has elongated facets. Nearly parallel ridges separate these facets. In the cleavage there are several parallel branches of chevron patterns, indicating a fracture surface characteristic with brittle fracture in bainite. When examining the initiation areas it was difficult to see what could have caused the fracture.

The grain size is larger and the inclusions are fewer. These factors influence the plastic flow and will affect the ductility, as stated in chapter 2.9.2.

Specimen 5.2.1 contains a mixture of several microstructures, especially acicular ferrite and upper bainite. Also the fracture seems to be a mixture of the two morphologies described in specimen 2.1 and 3.1. Equally to specimen 2.1 this specimen also have a large ductile area before the brittle fracture appears. In the brittle area there are small spots with dimples indicating that a ductile fracture has happened in between the brittle fracture. This may be one of the reasons that specimen 5.2.1 has such high impact energy in the Charpy V notch test presented in Figure 42.

5.4 TEM

5.4.1 Chemical analysis

Three different inclusions from specimen 2.1 are presented as they represent the multiple numbers of inclusions analyzed in the specimen. All of them had a core containing a titanium oxide phase. This may indicate that this compound was the first to form at higher temperature than the surrounding layer of manganese sulphide and other elements. The results from the line-scan do not show any indication of manganese depletion occurring around the surface of the inclusion as the theory in chapter 2.5 explains as one mechanism for acicular ferrite nucleation. It is therefore not possible to say whether the manganese sulphide had any impact on the acicular ferrite nucleation or not. It should be mentioned that this kind of measurements are difficult because the x-ray signal is dependent on sample thickness and the thinning around the particle is uneven.

Both inclusions presented from specimen 3.1 have a high content of aluminum, either as an aluminum oxide in the core or as a complex oxide in the whole inclusion. Both inclusions also contain small areas with zirconium, but only one of them detected sulfur. This shows that there are some differences in the composition of the inclusions, although they contain the same elements. Since complex oxides containing aluminum may be either active or inert, it is difficult to say if they are the reason to the low content of acicular ferrite. This weld contains large amounts of aluminum (0.9 wt %). Small amounts should, according to the theory in chapter 2.5, produce the much wanted titanium oxides, but it seems that this weld metal has too much aluminum for this to occur.

The inclusion examined from specimen 5.2.1 seems to mainly consist of a complex oxide, with magnesium, silicon, aluminum, oxygen and also some titanium. There is also a small area with increased amounts of sulfide, possibly due to the formation of manganese sulphide. This clearly shows the complexity of the inclusion. The titanium content of this weld (0.002 wt%) is much lower than for specimen 2.1, and may be the reason that there are no distinct area with a titanium oxide phase in this inclusion.

5.4.2 Indexed diffraction patterns

As the results show the two compounds indexed seem to be titanium oxide in form of Ti_3O_5 and manganese sulphide in form of MnS . This result was quite expected since the same compounds are found in similar weld metals in earlier research [2] [7] [28]. When indexing the titanium oxide there was several options found as relevant in previous research, among them were TiO , Ti_2O_3 and TiO_2 . None of these achieved similar d -values as the experimental values, and were therefore discarded.

5.4.3 Orientation relationship

There is no clear evidence that there is an orientation relationship between the iron matrix and the inclusion surface because it is difficult to conclude something from the experimental data as. Even so, there are some indications that an orientation relationship is present. The reason for the interference in the diffraction pattern (Figure 65) could possibly be from one of the MnS systematic rows being aligned with a matrix systematic row.

Chapter 6 Conclusion

Based on the experimental evaluations of three different weld metals, the following conclusions can be drawn:

- Enhanced oxygen content seems to have a positive effect on the non-metallic inclusions making them active in nucleating acicular ferrite.
- Specimen 3.1 had lower heat input than the two other specimens and may have contributed to the brittle microstructure with no or minimal amounts of acicular ferrite and smaller inclusions.
- Both alloying elements and micro alloying elements have a large impact on the weld metal microstructure. Titanium, nickel and manganese contribute to nucleation of acicular ferrite, while inclusions consisting of aluminum nitride phases are inert and will not nucleate acicular ferrite.
- The fracture surface appearance shows that specimen 2.1 and 5.2.1 have a large plastic distortion and have had a ductile fracture before the brittle fracture. Specimen 3.1 has a fracture surface characteristic to a brittle fracture in bainite.
- The three weld metals have very different content inside their inclusions.
- There is no evidence of manganese depletion occurring close to the inclusion surface when there is manganese sulphide on the edge of the inclusion.
- It is difficult to determine if there is an orientation relationship between the iron matrix and the manganese sulphide.
- One inclusion in specimen 2.1 contained at least two different compounds and was indexed as Ti_3O_5 and MnS.

Suggestions to further work

It is interesting to look closer on the chemical composition of the inclusions in the TEM and try to decide how the different types on inclusions affect the nucleation of different microstructures in the matrix.

It is also of interest to see more at which size the inclusions are insufficient to nucleate the desired microstructure acicular ferrite and instead are harmful to the weld metal causing a brittle microstructure.

Since there was a shortage of time to say much about the orientation relationship between the iron matrix and the different compounds in the non-metallic inclusions, it should be done further research on this area.

References

1. Lee, C.H., H.K.D.H. Bhadeshia, and H.C. Lee, *Effect of plastic deformation on the formation of acicular ferrite*. Materials Science and Engineering: A, 2003. **360**(1–2): p. 249-257.
2. Sarma, D.S., et al., *On the Role of Non-metallic Inclusions in the Nucleation of Acicular Ferrite in Steels*. ISIJ International, 2009. **49**(7): p. 1063-1074.
3. Kluken, A.O., Ø. Grong, and J. Hjelen, *The origin of transformation textures in steel weld metals containing acicular ferrite*. Metallurgical Transactions A, 1991. **22**(3): p. 657-663.
4. Grong, Ø., *Sveisemetallurgi*1990: Universitetet i Trondheim, NTH, Metallurgisk institutt.
5. Bhadeshia, H.K.D.H. and R.W.K. Honeycombe, *Steels - Microstructure and Properties*. 3rd edition ed 2006: Elsevier Ltd.
6. Bhadeshia, H.K.D.H. and J.W. Christian, *Bainite in steels*. Metallurgical Transactions A, 1990. **21**(3): p. 767-797.
7. T. Koseki, G.T., *Overview Inclusion assisted microstructure control in C–Mn and low alloy steel welds*. Materials Science and Technology, 2005. **21**(8): p. 867-879.
8. Kluken, A.O. and Ø. Grong, *Mechanisms of inclusion formation in Al–Ti–Si–Mn deoxidized steel weld metals*. Metallurgical Transactions A, 1989. **20**(8): p. 1335-1349.
9. Seo, J., et al., *Effect of titanium content on weld microstructure and mechanical properties of bainitic GMA welds*. Welding in the World, 2014. **58**(6): p. 893-901.
10. Harrison, P.L. and R.A. Farrar, *Influence of oxygen-rich inclusions on the $\gamma \rightarrow \alpha$ phase transformation in high-strength low-alloy (HSLA) steel weld metals*. Journal of Materials Science, 1981. **16**(8): p. 2218-2226.
11. Babu, S.S., *The mechanism of acicular ferrite in weld deposits*. Current Opinion in Solid State and Materials Science, 2004. **8**(3–4): p. 267-278.
12. Lee, D.N. and H.N. Han, *Directed Growth of Ferrite in Austenite and Kurdjumov-Sachs Orientation Relationship*. 2012: p. 128-133.
13. Dieter, G.E. and D. Bacon, *Mechanical Metallurgy*. SI metric ed 1988: McGraw Hill, London.
14. Colangelo, V.J. and F.A. Heiser, *Analysis of Metallurgical Failures*. 2nd ed 1987: Wiley, New York. 105-133.
15. Askeland, D.R., P.P. Fulay, and W.J. Wright, *The Science of Engineering of Materials*. 6th ed. ed, ed. C. Learning2011: Global Engineering. 252-258.
16. Hosford, W.F., *Mechanical behavior of materials*2010, Cambridge; New York: Cambridge University Press.

17. Askeland, D.R., P.P. Fulay, and W.J. Wright, *The Science and Engineering of Materials*, ed. C. Learning. Vol. 6th ed. 2011: Global Engineering. 227-228.
18. Hjelen, J., *Scanning elektron-mikroskopi* 1989: Metallurgisk institutt, NTH.
19. NTNU. *Index of /lab/material/equipment*. 2014 [cited 2014; Available from: <http://www.material.ntnu.no/lab/material/equipment/>].
20. Hjelen, J., *Lecture in TMT4300*, 2014.
21. Solberg, J.K. and V. Hansen, *Innføring i Transmisjons Elektronmikroskopi* 2014: Norwegian University of Science and Technology, University of Stavanger. 5-27.
22. Brandon, D. and W.D. Kaplan, *Transmission Electron Microscopy*, in *Microstructural Characterization of Materials* 2008, John Wiley & Sons, Ltd. p. 179-260.
23. Askeland, D.R., P.P. Fulay, and W.J. Wright, *The Science and Engineering of Materials*. Cengage Learning. Vol. 6th. ed. 2011: Global Engineering. 62-101.
24. Han, Y.S. and S.H. Hong, *Microstructural changes during superplastic deformation of Fe-24Cr-7Ni-3Mo-0.14N duplex stainless steel*. *Materials Science and Engineering: A*, 1999. **266**(1-2): p. 276-284.
25. Akselsen, O.M. and E. Østby, *Evaluation of Welding Consumables for Application down to -60°C*, 2014, International Society of Offshore and Polar Engineers.
26. Akselsen, O.M., E. Østby, and S. Aldstedt, *Arctic Materials – Weld metal test programme*, S.-M.a. Chemistry, Editor 2012.
27. Akselsen, O.M., *E-mail correspondence; Oxygen content*, 2014.
28. Kang, Y., et al., *Influence of Ti on non-metallic inclusion formation and acicular ferrite nucleation in high-strength low-alloy steel weld metals*. *Metals and Materials International*, 2014. **20**(1): p. 119-127.

Appendix

A – Project description

THE NORWEGIAN UNIVERSITY
OF SCIENCE AND TECHNOLOGY
DEPARTMENT OF ENGINEERING DESIGN
AND MATERIALS

**MASTER THESIS SPRING 2015
FOR
STUD. TECHN. ISABELLA JUUL HJELTEREIE**

**CHARACTERIZATION OF NON-METALLIC INCLUSIONS IN FERRITIC WELD METALS
FOR ARCTIC APPLICATIONS**

Oppgavetekst norsk

Mikrostrukturundersøkelser av sveismetall i konstruksjoner for kaldt klima

In exploration of oil and gas in the arctic region, the low ambient temperature may be the major challenge for structural materials. This is due to the ductile to brittle transition taking place at a certain temperature below 0°C. Design temperatures down to -60°C may be required in the worst case. Previous investigations have shown that the properties of weldments of available structural steels, including both the heat affected zone (HAZ) and the weld metal, are insufficient or on the borderline for arctic application down to -60°C, and may thus not give the required robust solutions. Therefore, the present work was initiated to evaluate weld metal toughness based on the use of commercial wires to clarify the need for further developments of welding consumables.

The topics to be investigated will be:

- Examination of nonmetallic inclusions with respect to
 - Types and composition
 - Orientation relationships
- Study the relation between type of inclusion and solid state nucleation
- Characterization of fracture surface appearance of different weld metals (if Charpy samples are available)
- Quantify volume fractions of the weld metal microstructure constituents

The two first tasks should be examined with transmission electron microscope (TEM), while scanning electron microscope (SEM) should be used for fracture surface appearance characterization. Finally, volume fractions can be determined by optical microscopy.

Three weeks after start of the thesis work, an A3 sheet illustrating the work is to be handed in. A template for this presentation is available on the IPM's web site under the menu "Masteroppgave" (<http://www.ntnu.no/ipm/masteroppgave>). This sheet should be updated one week before the Master's thesis is submitted.

Performing a risk assessment of the planned work is obligatory. Known main activities must be risk assessed before they start, and the form must be handed in within 3 weeks of receiving the problem text. The form must be signed by your supervisor. All projects are to

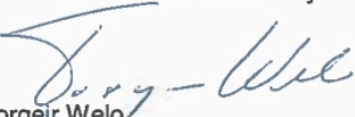
be assessed, even theoretical and virtual. Risk assessment is a running activity, and must be carried out before starting any activity that might lead to injury to humans or damage to materials/equipment or the external environment. Copies of signed risk assessments should also be included as an appendix of the finished project report.

The thesis should include the signed problem text, and be written as a research report with summary both in English and Norwegian, conclusion, literature references, table of contents, etc. During preparation of the text, the candidate should make efforts to create a well arranged and well written report. To ease the evaluation of the thesis, it is important to cross-reference text, tables and figures. For evaluation of the work a thorough discussion of results is appreciated.

The thesis shall be submitted electronically via DAIM, NTNU's system for Digital Archiving and Submission of Master's thesis.

Contact persons are:

NTNU: Prof.II Odd M. Akselsen
Prof.II John Whalmsley



Torgeir Welo
Head of Division



Odd M. Akselsen
Professor/Supervisor



NTNU
Norges teknisk-
naturvitenskapelige universitet
Institutt for produktutvikling
og materialer

B – Risk assessment

NTNU	Risikovurdering				Utarbeidet av	Nummer	Dato	
					HMS-avd.	HMSRV2601	22.03.2011	
HMS					Godkjent av		Erstatter	
					Rektor		01.12.2006	

Dato: 15.01.15

Enhet: Institutt for materialteknologi (IMT) / Institutt for produktutvikling og materialer (IPM)

Linjeleder: Jostein Mårdalen / Torgeir Welo

Deltakere ved kartleggingen (m/ funksjon):

Odd Magne Akselsen, hovedveileder

Isabella Juul Hjeltereie, student

Risikovurderingen gjelder hovedaktivitet: Masteroppgave for Isabella Juul Hjeltereie.

Characterization of non-metallic inclusions of ferritic weld metals for arctic applications


Signaturer: Ansvarlig veileder:



Student:



ID nr	Aktivitet fra kartleggings-skjemaet	Mulig uønsket hendelse/ belastning	Vurdering av sannsynlighet (1-5)	Vurdering av konsekvens:				Risiko-Verdi (menn-eske)	Kommentarer/status Forslag til tiltak
				Menneske (A-E)	Ytre miljø (A-E)	Øk/ materiell (A-E)	Om-dømme (A-E)		
1.	Prøvepreparering: Sliping og polering	Oppskraping av fingre	4	A	A	A	A	4A	Bruk manuell prøve-preparering. Vær varsom og fokusert. Bruke nødvendig verneutstyr.
2.	Prøvepreparering: Innstøping	Løsemiddelskade	1	E	A	A	E	1C	Foreta innstøping i avtrekkskap. Bruke nødvendig verneutstyr. Les datablad.
3.	Prøvepreparering: Etsing	Etseskade	3	C	A	A	B	3B	Foreta etsing i avtrekkskap. Bruke nødvendig verneutstyr. Les datablad før etsing.
4.	Mikroskopering (Ivsmikroskop).	Skade på utstyr	1	A	A	C	A	1B	Få grundig opplæring. Stille spørsmål ved usikkerheter.
5.	Mikroskopering (SEM)	Skade på utstyr	2	A	A	C	A	2B	Få grundig opplæring. Stille spørsmål ved usikkerheter.
6.	Mikroskopering (TEM)	Skade på utstyr	1	A	A	C	A	1A	Utstyret brukes ikke av studenter, kun av ansatte ved NTNU.

NTNU	Risikovurdering				Utarbeidet av	Nummer	Dato
					HMS-avd.	HMSRV2601	22.03.2011
HMS					Godkjent av Rektor		Erstatter 01.12.2006



Sannsynlighet vurderes etter følgende kriterier:

Svært liten 1	Liten 2	Middels 3	Stor 4	Svært stor 5
1 gang pr 50 år eller sjeldnere	1 gang pr 10 år eller sjeldnere	1 gang pr år eller sjeldnere	1 gang pr måned eller sjeldnere	Skjer ukentlig

Konsekvens vurderes etter følgende kriterier:

Gradering	Menneske	Ytre miljø Vann, jord og luft	Øk/materiell	Omdømme
E Svært Alvorlig	Død	Svært langvarig og ikke reversibel skade	Drifts- eller aktivitetsstans > 1 år.	Troverdighet og respekt betydelig og varig svekket
D Alvorlig	Alvorlig personskaade. Mulig uførhet.	Langvarig skade. Lang restitusjonstid	Drifts- eller aktivitetsstans i opp til 1 år	Troverdighet og respekt betydelig svekket
C Moderat	Alvorlig personskaade.	Mindre skade og lang restitusjonstid	Drifts- eller aktivitetsstans < 1 mnd	Troverdighet og respekt svekket
B Liten	Skade som krever medisinsk behandling	Mindre skade og kort restitusjonstid	Drifts- eller aktivitetsstans < 1 uke	Negativ påvirkning på troverdighet og respekt
A Svært liten	Skade som krever førstehjelp	Ubetydelig skade og kort restitusjonstid	Drifts- eller aktivitetsstans < 1 dag	Liten påvirkning på troverdighet og respekt

Risikoverdi = Sannsynlighet x Konsekvens

Beregn risikoverdi for Menneske. Enheten vurderer selv om de i tillegg vil beregne risikoverdi for Ytre miljø, Økonomi/materiell og Omdømme. I så fall beregnes disse hver for seg.

Til kolonnen "Kommentarer/status, forslag til forebyggende og korrigerende tiltak":

Tiltak kan påvirke både sannsynlighet og konsekvens. Prioriter tiltak som kan forhindre at hendelsen inntreffer, dvs. sannsynlighetsreduserende tiltak foran skjerpet beredskap, dvs. konsekvensreduserende tiltak.

NTNU	Kartlegging av risikofylt aktivitet				Utarbeidet av	Nummer	Dato	
					HMS-avd.	HMSRV2601	22.03.2011	
					Godkjent av		Erstatter	
					Rektor		01.12.2006	

MATRISSE FOR RISIKOVURDERINGER ved NTNU

KONSEKVENSENS		Svært alvorlig	E1	E2	E3	E4	E5
		Alvorlig	D1	D2	D3	D4	D5
		Moderat	C1	C2	C3	C4	C5
		Liten	B1	B2	B3	B4	B5
		Svært liten	A1	A2	A3	A4	A5
			Svært liten	Liten	Middels	Stor	Svært stor
			SANNSYNLIGHET				

Prinsipp over akseptkriterium. Forklaring av fargene som er brukt i risikomatrisen.

Farge	Beskrivelse
Rød	Uakseptabel risiko. Tiltak skal gjennomføres for å redusere risikoen.
Gul	Vurderingsområde. Tiltak skal vurderes.
Grønn	Akseptabel risiko. Tiltak kan vurderes ut fra andre hensyn.

C – MacTempasX input data

Ti₃O₅

04-008-8183

May 27, 2015 4:01 PM (XRD-lab)

Status Primary QM: Indexed Pressure/Temperature: Ambient Chemical Formula: Ti₃O₅
 Empirical Formula: O₅Ti₃ Weight %: 0.35.77 Ti64.23 Atomic %: 0.62.50 Ti37.50 ANX: A3X5
 Compound Name: Titanium Oxide Common Name: $\bar{\alpha}$ -Ti₃O₅

Radiation: CuK α 1 : 1.5406 Å d-Spacing: Calculated Intensity: Calculated I/c: 1.21 I/c - ND: 0.31

SYS: Monoclinic SPGR: I2/c (15)

Author's Cell [AuthCell a: 9.9701(5) Å AuthCell b: 5.0747(3) Å AuthCell c: 7.1810(4) Å
 AuthCell : 109.865(4)° AuthCell Vol: 341.71 Å³ AuthCell Z: 4.00 AuthCell MolVol: 85.43]
 Author's Cell Axial Ratio [c/a: 0.720 a/b: 1.965 c/b: 1.415]
 Density [Dcalc: 4.348 g/cm³ Dstruc: 4.35 g/cm³] SS/FOM: F(30) = 282.5(0.0025, 43)
 Temp: 297.000 K (Author provided temperature) Color: Black

Space Group: I2/a (15) Molecular Weight: 223.70

Crystal Data [XtlCell a: 9.970 Å XtlCell b: 5.075 Å XtlCell c: 7.181 Å XtlCell : 90.00° XtlCell : 109.86°
 XtlCell : 90.00° XtlCell Vol: 341.71 Å³ XtlCell Z: 4.00]
 Crystal Data Axial Ratio [c/a: 0.720 a/b: 1.965 c/b: 1.415]
 Reduced Cell [RedCell a: 5.075 Å RedCell b: 5.658 Å RedCell c: 7.181 Å RedCell : 109.58°
 RedCell : 90.00° RedCell : 116.64° RedCell Vol: 170.85 Å³]

ADP Type: B Crystal (Symmetry Allowed): Centrosymmetric

SG Symmetry Operators:

Seq	Operator	Seq	Operator	Seq	Operator	Seq	Operator
1	x,y,z	2	-x,-y,-z	3	x,-y,z+1/2	4	-x,y,-z+1/2

Atomic Coordinates:

Atom	Num	Wyckoff	Symmetry	x	y	z	SOF	Biso	AET
Ti	1	8f	1	0.37099	0.48805	0.0898	1.0	0.368	6-a
Ti	2	4b	-1	0.0	0.5	0.0	1.0	0.36	6-a
O	3	8f	1	0.68944	0.83681	0.53592	1.0	0.493	3#a
O	4	8f	1	0.58096	0.34457	0.63893	1.0	0.426	4-a
O	5	4e	2	0.0	0.30804	0.25	1.0	0.444	4-a

Subfile(s): Inorganic, Metals & Alloys Former PDF's #: 01-076-1066 Prototype Structure: V3 O5

Prototype Structure [Alpha Order]: O5 V3 LPF Prototype Structure: V3 O5,mS32,15

LPF Prototype Structure [Alpha Order]: O5 V3,mS32,15 Pearson: mC32.00

Cross-Ref PDF #'s: 00-027-0905 (Deleted), 00-040-0806 (Primary), 04-007-3972 (Alternate), 04-008-1597 (Alternate)

Entry Date: 09/01/2005 Last Modification Date: 09/01/2011 Last Modifications: Reflections

References:

Type	DOI	Reference
------	-----	-----------

Primary Reference		Calculated from LPF using POWD-12++.
-------------------	--	--------------------------------------

Structure		*The Structure of $\bar{\alpha}$ -Ti ₃ O ₅ at 297 K*. Hong S.H., anstrom sbrink S. Acta Crystallogr., Sec. B: Struct. Crystallogr. Cryst. Chem. 38, 2570 (1982).
-----------	--	--

ANX: A3X5. Color: black. LPF Collection Code: 2050123. Sample Preparation: STARTING
 MATERIALS: Ti₃O₅, Ti₂O₃. Compound Preparation: chemical transport method, transport agent TeCl₄.
 Database Comments: CRUCIBLE: sealed silica tube. Sample crystallized below 1200 K. Temperature of Data Collection: 297 K.
 Minor Warning: LPF Editor Comment: computed linear absorption coefficient differs significantly from
 published value. Unit Cell Data Source: Powder Diffraction.

d-Spacings (199) - 04-008-8183 (Fixed Slit Intensity) - Cu K1 1.54056 Å

2(°)	d(Å)	I	h	k	l	*	2(°)	d(Å)	I	h	k	l	*	2(°)	d(Å)	I	h	k	l	*
18.9125	4.688420	573	2	0	0		40.2321	2.239690	331m	1	2	1		52.6493	1.736990	m	-1	2	3	
19.8771	4.463020	172	1	1	0		40.2321	2.239690	m	-4	1	1		53.1487	1.721840	55	4	2	0	
21.8895	4.057040	6	0	1	1		40.3860	2.231510	89	2	2	0		53.3050	1.717160	13	-4	2	2	
26.3712	3.376850	777	0	0	2		42.0810	2.145460	197	-2	1	3		54.2857	1.688430	3	0	0	4	
26.7615	3.328480	161	-2	0	2		43.9642	2.057830	1	0	1	3		54.8930	1.671180	516m	-1	1	4	
30.4774	2.930590	762	-1	1	2		44.6333	2.028520	265	0	2	2		54.8930	1.671180	m	-3	2	3	
31.9566	2.798240	1	2	1	1		44.8812	2.017890	38	-2	2	2		55.1413	1.664240	115m	1	3	0	
33.6483	2.661320	999	3	1	0		48.6218	1.871030	10	4	1	1		55.1413	1.664240	m	-4	0	4	
35.3451	2.537350	376	0	2	0		48.9550	1.859070	5	-4	1	3		55.3188	1.659320	46	-3	1	4	
35.8171	2.504990	104	1	1	2		49.3090	1.846550	14	3	1	2		55.7446	1.647650	193	-6	0	2	
36.4093	2.465590	583	-3	1	2		50.2235	1.815050	1	-5	1	2		57.9437	1.590240	1m	1	2	3	
37.1199	2.382880	91	2	0	2		50.8293	1.794830	11	-2	0	4		57.9437	1.590240	m	-2	3	1	
37.9167	2.370960	18	-1	2	1		50.9503	1.790850	16	3	2	1		58.7719	1.569790	3	-6	1	1	
38.3662	2.344210	55	4	0	0		51.9381	1.759090	387	5	1	0		59.0603	1.562810	27	6	0	0	
38.5676	2.332430	11	-4	0	2		52.6493	1.736990	516m	2	2	2		60.4493	1.530180	76	-1	3	2	

© 2015 International Centre for Diffraction Data. All rights reserved.

Page 1 / 2

MnS

00-006-0518

May 27, 2015 3:24 PM (XRD-lab)

Status Primary QM: Star Pressure/Temperature: Ambient Chemical Formula: Mn +2 S

Empirical Formula: Mn S Weight %: Mn63.15 S36.85 Atomic %: Mn50.00 S50.00

Compound Name: Manganese Sulfide Mineral Name: Alabandite, syn

Radiation: CuK α 1 : 1.5405 Å Filter: Ni Beta Intensity: Diffractometer

SYS: Cubic SPGR: Fm-3m (225)

Author's Cell [AuthCell a: 5.224 Å AuthCell b: 142.56 Å³ AuthCell Z: 4.00 AuthCell MolVol: 35.64]Density [Dcalc: 4.053 g/cm³ Dmeas: 4.03 g/cm³] SS/FOM: F(12) = 54.2(0.0138, 16)

Temp: 299.000 K (Author provided temperature) Color: Black metallic

Space Group: Fm-3m (225) Molecular Weight: 87.00

Crystal Data [XtlCell a: 5.224 Å XtlCell b: 5.224 Å XtlCell c: 5.224 Å XtlCell : 90.00° XtlCell : 90.00°

XtlCell : 90.00° XtlCell Vol: 142.56 Å³ XtlCell Z: 4.00]

Crystal Data Axial Ratio [a/b: 1.000 c/b: 1.000]

Reduced Cell [RedCell a: 3.694 Å RedCell b: 3.694 Å RedCell c: 3.694 Å RedCell : 60.00°

RedCell : 60.00° RedCell : 60.00° RedCell Vol: 35.64 Å³]

: =2.70

Atomic parameters are cross-referenced from PDF entry 04-008-2759

Crystal (Symmetry Allowed): Centrosymmetric

SG Symmetry Operators:

Seq	Operator	Seq	Operator	Seq	Operator	Seq	Operator	Seq	Operator	Seq	Operator	Seq	Operator
1	x,y,z	8	-x,-z,-y	15	z,-x,-y	22	-y,x,z	29	-y,z,-x	36	z,-y,x	43	-x,-z,y
2	-x,-y,-z	9	y,x,z	16	-z,x,y	23	z,-y,-x	30	y,-z,x	37	-x,-y,z	44	x,z,-y
3	z,x,y	10	-y,-x,-z	17	y,-z,-x	24	-z,y,x	31	-x,-z,-y	38	x,y,-z	45	-y,-x,z
4	-z,-x,-y	11	z,y,x	18	-y,z,x	25	-x,y,-z	32	x,-z,y	39	-z,-x,y	46	y,x,-z
5	y,z,x	12	-z,-y,-x	19	x,-z,-y	26	x,-y,z	33	-y,x,-z	40	z,x,-y	47	-z,-y,x
6	-y,-z,-x	13	x,-y,-z	20	-x,z,y	27	-z,x,-y	34	y,-x,z	41	-y,-z,x	48	z,y,-x
7	x,z,y	14	-x,y,z	21	y,-x,-z	28	z,-x,y	35	-z,y,-x	42	y,z,-x		

Atomic Coordinates:

Atom	Num	Wyckoff	Symmetry	x	y	z	SOF	IDP	AET
Mn	1	4a	m-3m	0.0	0.0	0.0	1.0		6-a
S	2	4b	m-3m	0.5	0.5	0.5	1.0		6-a

Subfile(s): Common Phase, Educational Pattern, Inorganic, Metals & Alloys, Mineral Related (Mineral , Synthetic), NBS Pattern

Prototype Structure: Na Cl Prototype Structure [Alpha Order]: Cl Na

Mineral Classification: Halite (Group), chalcogenide (Subgroup) Pearson: cF8.00

Cross-Ref PDF #s: 04-003-1517 (Primary), 04-003-1776 (Alternate), 04-003-1892 (Alternate), 04-003-2554 (Alternate), 04-003-4153 (Alternate), 04-003-4314 (Alternate), 04-003-5458 (Alternate), 04-003-5942 (Alternate), 04-003-6939 (Alternate), 04-003-7138 (Alternate), 04-003-7147 (Alternate), 04-004-2223 (Alternate), 04-004-4211 (Alternate), 04-004-5281 (Alternate), 04-004-5295 (Alternate), 04-004-6657 (Alternate), 04-005-7887 (Alternate), 04-006-4930 (Alternate), 04-006-4932 (Alternate), 04-006-5506 (Alternate), 04-007-3621 (Alternate), 04-008-2759 (Alternate), 04-008-4037 (Alternate)

Entry Date: 09/01/1956

References:

Type	DOI	Reference
Primary Reference		Swanson et al. Natl. Bur. Stand. (U. S.), Circ. 539 IV, 11 (1955).
Crystal Structure		Crystal Structure Source: LPF.
Optical Data		Dana's System of Mineralogy, 7th Ed. I.

Database Comments: Additional Patterns: See PDF 01-072-1534. Analysis: Spectroscopic analysis: <0.1% Al; <0.01% Cr, Fe, Mg, Si, Sn; <0.001% B, Ca, Cu, Ni; <0.0001% Ag. Color: Black metallic. Opaque Optical Data: Opaque mineral optical data on specimen from Kapnik, Rumania: RR2Re=22.8, Disp.=16, VHN100=240-251, Color values=.301, .305, 22.8, Ref.: IMA Commission on Ore Microscopy Q.D.F. Polymorphism/Phase Transition: Two polymorphs exist. Sample Preparation: Prepared by heating Mn and S in closed tube at 675 C for 2 hours. Structures: Cubic \bar{a} -ZnS structure and \bar{a} hexagonal ZnO structure. Temperature of Data Collection: Pattern taken at 299 K. Unit Cell Data Source: Powder Diffraction.

d-Spacings (12) - 00-006-0518 (Fixed Slit Intensity) - Cu K α 1.54056 Å

2(°)	d(Å)	I	h	k	l	*	2(°)	d(Å)	I	h	k	l	*	2(°)	d(Å)	I	h	k	l	*
29.6044	3.015000	14	1	1	1		58.5585	1.575000	6	3	1	1		82.5042	1.168200	20	4	2	0	
34.3031	2.612000	100	2	0	0		61.3886	1.509000	20	2	2	2		92.5149	1.066200	16	4	2	2	
49.2962	1.847000	50	2	2	0		72.2858	1.306000	8	4	0	0		113.0419	0.923500	2	4	4	0	

© 2015 International Centre for Diffraction Data. All rights reserved.

Page 1 / 2

